UNIVERSITY OF CALIFORNIA
SANTA CRUZ

THE CHEMICAL STRUCTURE OF VENUS'S ATMOSPHERE AND INTERIOR EVOLUTION OF KUIPER BELT OBJECTS

A dissertation submitted in partial satisfaction of the
requirements for the degree of

DOCTOR OF PHILOSOPHY

in

EARTH SCIENCE

by

Carver Jay Bierson

June 2020

The Dissertation of Carver Jay Bierson
is approved:

Professor Francis Nimmo, Chair

Professor Xi Zhang

Professor Nicole Feldl

Dr. Kevin Zahnle

Quentin Williams
Acting Vice Provost and Dean of Graduate Studies

Table of Contents

List of Figures

List of Tables

Abstract

The chemical structure of Venus's atmosphere and interior evolution of Kuiper belt objects

by

Carver Jay Bierson

This thesis is composed of two distinct themes. The first concerns the chemical structure of Venus's atmosphere. Venus's atmosphere can be roughly separated into lower and middle regions separated by a thick cloud deck. When modeling the chemistry of Venus' atmosphere past researchers have focused on these regions separately. In doing so they have made conflicting assumptions about the cloud region that connects them. In Chapter 2 I present the first detailed chemical model of Venus' atmosphere that includes both the lower and middle atmosphere. This model is used to characterize the chemical recycling pathways of observed trace species. In this study I find that there also exists a yet unidentified sink of sulfur-dioxide in the Venusian clouds.

The second theme of this thesis concerns understanding the interior structure and history of Kuiper Belt objects. In July 2015, NASA's New Horizons spacecraft made its close flyby of Pluto. This opened a new era for understanding not only of Pluto, but also the nature of Kuiper Belt objects generally. To this end I developed a model of how the bulk density of Kuiper Belt objects would evolve through time due to changes in porosity and the melting and refreezing of a subsurface ocean. In Chapter 3 I apply this model to Pluto and its largest moon Charon. I found that the density contrast

between Pluto and Charon is large enough that it can only be reasonably explained by a difference in bulk composition (eg. rock to ice ratio).

In Chapter 4 I apply this model to bulk density measurements of Kuiper Belt objects (KBOs) generally. It has previously been observed that small KBOs have a much lower bulk density than their larger counterparts. I have found that this can naturally be explained by smaller KBOs being more porous. This difference in porosity is due to the longer cooling timescale of large KBOs causing them to warm more from the heat of radioactive decay. This in turn causes the ice to viscously relax away porosity. Small KBOs in contrast can efficiently conduct out this heat while staying cold and rigid. Because this depends on the abundance and heat production of radioactive elements, I have used this density information to place a constraint on when these objects formed.

In Chapter 5 I revisit Pluto examining what the observed tectonics imply about the history of Pluto's subsurface ocean. Namely I consider whether these observations are more consistent with Pluto having that ocean shortly after formation or developing it over a longer timescale through radioactive decay of long lived radioisotopes. If Pluto did form its ocean slowly, this would have caused global compression for which we find no tectonic evidence. If, however, Pluto started with an ocean we predict two stages of extension which is far more consistent with the observed geology.

To Dufouria

Acknowledgments

I am writing this thesis in strange times. Currently the state of California (and many other places) are under "Shelter in Place" orders for the foreseeable future; a unit of time that has grown considerably shorter. This is a time when we are more physically isolated and yet people have been working to come together more than ever. As such, it is fitting in such a time to reflect on all those who have helped me through the last six years of this journey.

I have to start with the person who invited me to UCSC, Francis. When I came to UCSC I didn't know what I wanted to study or even what good questions were. Francis allowed me to pursue my own ideas even when they went nowhere. Most impressively, Francis always made himself available to help while never feeling overbearing.

When I came to UCSC I knew almost nothing of planetary atmospheres except that they are beautiful and strange. I reached out to Xi before he even started as a Professor and he agreed to advise me in my quest to study Venus's atmosphere. Xi has an immense enthusiasm for understanding atmospheres. I remembering coming away from many meetings excited for the many different things we might discover. He has also always been willing to give his time to help where needed and keep me on the right track.

For my first year at UCSC I was quickly trying to both learn how to do grad school and also how I was going to do grad school. Doug and Naor were the old guard that showed me the ropes and let me make my own mistakes along the way. I learned so

much from both of them in our discussions about everyday physics, social philosophy, and how to break down research questions.

Since I started at UCSC a slew of new planetary graduate students have joined. It has been a great privilege for me to be able to work with all these great people and ask their advice on questions of research or life. It has great to be watch the group grow to now eleven people and to have that group be known for their involvement within the department. Thanks to Nick, Jack, Rachel, Szilard, Megan, Coby, Wencheng, Brynna, Linfeng, Huazhi, and Secana.

For most of my grad school run I lived on Dufour street in a house we called Dufouria. That core group of Kyle, Karen, and Wilson made that house a special place. At Dufouria someone would always listen to your story, guests were always welcome, and the house always smelled of wonderful baked goods.

I would not have been able to do any of my work without all of the wonderful support staff of the Earth and Planetary science department. One of the first things I was told when I started was, "if you have any problem, ask Jennifer". Little did I realize how that true that was. No matter what the situation was Jennifer always was able to help me find a solution. In the day to day life of the department Amy has always been there to help me find resources or teach me how to use the scanner (again). And without our IT support none of my research would be possible. Over the years this has included many people including Rion Parsons, Ocho Torres, Brecky Morris, and Ed Boring.

If there is one thing nearly everyone in the department knows about me, it is

that I take my lunch at noon outside at the picnic table. Over the years I have been fortunate that so many wonderful people have joined me for those lunches. Thanks to all who have done so. A special thanks to Sarah Neuhaus has been one of my most consistent lunch friends and I will always be grateful to her for that.

This section would obviously not be complete without those who put up with me before this adventure and through it all. Thanks to my parents for always supporting me even when you didn't know what I was doing. Thanks to my sister for always keeping me in check. Thanks to all my extended family including my grandparents Jack and Linda, my aunt Sara, and cousin Kate. Thanks to Zach for not only being a good partner in the backcountry but also letting me advise you on your first research project.

Lastly, thanks to Alicia for being me best friend for 15+ years. I cannot say in writing how grateful I am for all the support you have given me. I only hope that I can return the favor in the years to come.

Previously published material

The text of this thesis includes modified reprints of the following previously published material:

Chapter 2: Bierson, C. J., & Zhang, X. (2020). "Chemical cycling in the Venusian atmosphere: A full photochemical model from the surface to 110 km". Journal of Geophysical Research: Planets, 125.

Chapter 3: Bierson, C. J., F. Nimmo, and W. B. McKinnon (2018) "Implications of the

observed PlutoCharon density contrast." Icarus 309, 207-219.

Chapter 4: Bierson, C. J., & Nimmo, F. (2019). "Using the density of Kuiper Belt Objects to constrain their composition and formation history". Icarus, 326, 10-17.

Chapter 5: Bierson, C. J., Nimmo, F., and S. A. Stern (2020). "Evidence for a hot start and early ocean formation on Pluto". Nature Geoscience

Chapter 1

Introduction

The first part of this thesis concerns the atmosphere of Venus. In almost every respect, Venus is the most Earth-like world we know of. Venus has a very similar radius and density to the Earth's, but its atmosphere is quite different. The atmosphere of Venus is about ninety times the mass of Earths and is composed primarily of carbon dioxide. Between 50-75 km altitude Venus has a thick cloud deck (Knollenberg and Hunten, 1980). These clouds are composed of a mix of condensed water and sulfuric acid. These clouds also form the boundary between the lower and middle atmosphere regions.

Previous research on the atmospheric chemistry of Venus's atmosphere has focused on either the lower or middle atmosphere separately. High temperatures in the lower atmosphere cause this region to be dominated by thermal chemistry (Krasnopolsky, 2007). This drives most of the sulfur in this region into sulfur-dioxide, the most abundant minor species in the lower atmosphere. This sulfur dioxide is mixed through

the clouds into the middle atmosphere. In the middle atmosphere photo-chemical reactions break down both sulfur dioxide and carbon dioxide (Krasnopolsky, 2012; Zhang et al., 2012).

In this thesis I present work aimed at understanding the chemical interactions between Venus' middle and lower atmosphere. I have used a chemical model to characterize how different chemical groups are cycled between these two regions. By combining this with observations we propose new chemical pathways and highlight the laboratory studies that would provide the most insight for future work.

The second part of this thesis focuses on the thermal history of Pluto and Kuiper belt objects generally. Our understanding of Pluto was revolutionized with the New Horizons flyby in July, 2015 (Stern et al., 2015). While Pluto is the largest Kuiper belt object, prior to this flyby the uncertainty on its radius was relatively large due to its atmosphere. After the flyby the radius was determined to within $\sim$1 km (Nimmo et al., 2016b) establishing that Pluto and its large moon Charon had distinct densities. This raised the question of what the cause of this density contrast might be? This question is the focus of Chapter 3.

One surprising characteristic of Kuiper belt objects (KBOs) is a that very large fraction of them are in binary systems (i.e. have moons). This allows for accurate determinations of their mass and therefor their density. By collating these observations previous authors have noticed that small KBOs have lower densities than their larger counterparts (Brown, 2012). The cause of this trend difference was not clear. In Chapter 4 I propose porosity as the explanation for this density difference.

One of the most exciting discoveries by New Horizons was the multiple lines of evidence for a subsurface ocean on Pluto (Nimmo et al., 2016a; Moore et al., 2016; Cruikshank et al., 2019). Thermal evolution models of Pluto have generally assumed that after accretion Pluto was cold, i.e. an solid ice shell overlying a silicate core. In Chapter 5 I consider the possibility that Pluto had its liquid ocean shortly after formation, i.e. a hot start. These two initial conditions lead to different predictions of Pluto's strain history. I compare those predictions to the observed geology note what future studies can be done with the existing data.

Chapter 2

Chemical cycling in the Venusian atmosphere: A full photo-chemical model from the surface to 110 km

This chapter is a slightly modified reprint of work previously published as Bierson, C. J., & Zhang, X. (2020). "Chemical cycling in the Venusian atmosphere: A full photochemical model from the surface to 110 km". Journal of Geophysical Research: Planets, 125, e2019JE006159. https://doi.org/10.1029/2019JE006159

Abstract

Venus is an exceptional natural experiment to test our understanding of atmospheric sulfur chemistry. Previous modeling efforts have focused on understanding either the middle or lower atmosphere. In this work we performed the first full-atmosphere

analysis of the chemical-transport processes on Venus from the surface to 110 km using a 1D diffusion model with photochemistry. We focused on the cycling of chemical species between the upper and lower atmospheres and interactions between distinct species groups including SO_x, CO_x+OCS, chlorides, NO_x, O_x, and S_x. We tested different eddy diffusivity profiles and investigated their influences on the vertical profiles of important species. We find that the assumed boundary conditions in previous models strongly impacted their simulation results. This has a particularly large effect for SO_2. We find the high SO_2 abundance in the lower atmosphere is readily transported into the the middle atmosphere, far exceeding observed values. This implies some yet unknown chemistry or process limiting SO_2 mixing. We summarize outstanding questions raised by this work and note chemical reactions that should be the highest priority for future laboratory studies and ab initio calculations.

2.1 Introduction

Venus is a natural laboratory for understanding atmospheric sulfur chemistry. Over the last decade there have been a wealth of observations of the minor species in Venus's atmosphere from both ground-based observations (Marcq et al., 2006; Krasnopolsky, 2010b; Arney et al., 2014; Sandor et al., 2012; Jessup et al., 2015; Sandor and Clancy, 2017, 2018) and Venus Express (Marcq et al., 2008; Belyaev et al., 2008, 2012). Chemical models have been developed for the lower atmosphere (Yung et al., 2009; Krasnopolsky, 2013) and middle atmosphere (Krasnopolsky, 2012; Zhang et al.,

2012; Jessup et al., 2015). These two regions are separated by the thick cloud layers that extend from roughly 40 km to 70 km altitude. In the lower atmosphere the high temperatures (400 K-700 K) drive chemical systems to thermochemical equilibrium. In the middle atmosphere, where the temperatures are more similar to Earth's stratosphere (200 K-300 K), photochemistry is the dominant process.

In this work we present the first detailed chemical model that couples the lower and middle atmosphere. This is an attempt to understand how the limited domain of previous models impacted their results and determine what open questions can be better understood using a coupled model. Our results are broken up by species groups. We summarize the major outstanding questions (both pre-existing and raised by this study) and what future work is needed. The goal of this work is not to present the "best" or most highly tuned Venus atmospheric chemistry model. Instead we aim to use this model as a tool for exploring the interactions between species and regions of the Venusian atmosphere. First we briefly review the key observational constraints and previous modeling efforts.

2.1.1 Overview of Chemical cycles

In this work we focus on the chemical cycles for three species groups: sulfur oxides, carbon oxides, and chlorides (shown in Figure 2.1). Other groups including oxygen, nitrous oxides, and polysulfur species will be discussed briefly. Here we provide an overview of the interactions between these groups. For more background see the recent reviews by Mills and Allen (2007) and Marcq et al. (2017). In Section 2.3 these

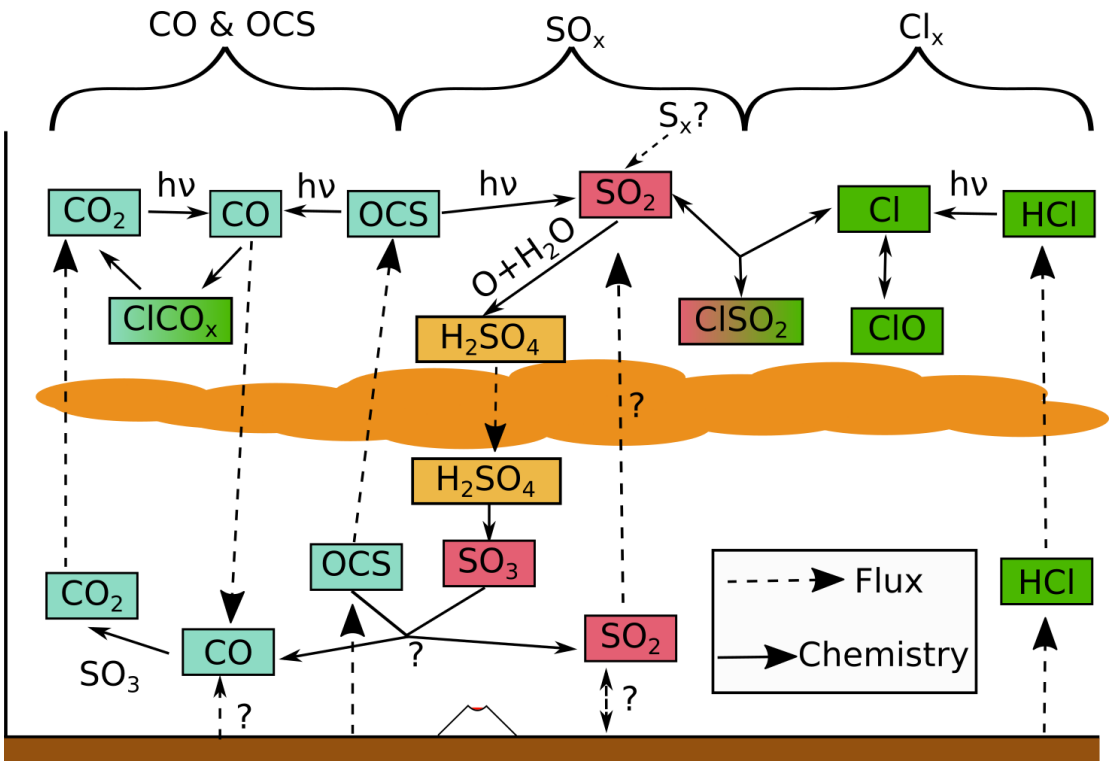

Figure 2.1: Cartoon showing the main species groups discussed in this work and their interactions.

processes will be evaluated and quantified.

By far the most thoroughly observed (and modeled) species in the lower atmosphere are carbon monoxide (CO) and carbonyl sulfide (OCS). At ∼30 km OCS is present at the ppm level. The OCS mixing ratio then decreases rapidly with altitude at about 35 km (Marcq et al., 2006; Arney et al., 2014). Conversely CO has a near surface mixing ratio of ∼20 ppm and a gradual increase with altitude. CO is also observed to increase in mixing ratio by ∼5 ppm within 30° of the poles (Marcq et al., 2006; Cotton et al., 2012). OCS does not have an unambiguous trend with latitude although Marcq et al. (2006) and Marcq et al. (2008) have suggested a possible decrease in mixing ratio

at high latitudes. Several chemical pathways have been proposed for conversion between CO and OCS (Krasnopolsky and Pollack, 1994; Yung et al., 2009) and are discussed in detail in Section 2.3.2.

Photolysis of carbon dioxide (CO_2) in the middle atmosphere produces CO and O which are slow to directly recombine back to CO_2. This leads to a build up of oxygen species including O_2. However, observed upper limits on the O_2 column density suggest that there is some catalytic mechanism providing more efficient recombination (Section 2.3.3 and Mills and Allen (2007)).

In the middle atmosphere the most thoroughly observed minor species is sulfur dioxide (SO_2). Vandaele et al. (2017) provides an excellent review of observations from ground-based and Venus Express measurements. Venus Express terminator measurements allow for well-resolved vertical profiles of SO_2 (Belyaev et al., 2012). These observations show that the mixing ratio of SO_2 decreases briefly above the clouds before inverting and increasing with altitude from ∼80 km up to ∼100 km. It was initially suggested that this could be due to the photolysis of sulfuric acid (H_2SO_4) at high altitudes (Zhang et al., 2010) but followup observations found that not enough H_2SO_4 was present (Sandor et al., 2012). The source of sulfur driving this inversion is still unclear and polysulfur aerosols remain a possibility (Zhang et al., 2012).

SO, SO_2, and SO_3 are quickly recycled inside the sulfur oxides group above the clouds. The relative abundance of these species is set by the balance between photolysis (creating more SO) and oxidation (producing SO_2 and SO_3). SO_3 will readily react with water vapor to form sulfuric acid (H_2SO_4). This sulfuric acid then condenses to

form the bulk of the cloud deck. At the base of the clouds (∼40 km), temperatures are high enough that the sulfuric acid droplets evaporate and the vapor is then thermally decomposed back into SO_3 and water. This lower atmosphere SO_3 is also converted to the more stable SO_2 and diffused upward to the middle atmosphere completing the sulfur cycle.

The most abundant chlorine species in the Venusian atmosphere is hydrochloric acid (HCl). HCl has been observed in the lower and middle atmosphere with a roughly constant mixing ratio of 100-400 ppm (Arney et al., 2014; Sandor and Clancy, 2017). Recently chlorine monoxide (ClO) was also observed to have a mixing ratio of ∼2 ppb at 85 km (Sandor and Clancy, 2018). Sandor and Clancy (2018) interpreted this concentration of ClO as requiring an additional significant reservoir of chlorine in the middle atmosphere apart from HCl.

2.1.2 Previous models

Previous chemical models of the Venusian atmosphere have focused on either the lower (Krasnopolsky, 2007, 2013) or middle atmosphere (Zhang et al., 2010, 2012; Krasnopolsky, 2012). The model of Krasnopolsky (2007) is not notably different from the updated version in Krasnopolsky (2013) and so we only discuss the latter. For the same reason we only review Zhang et al. (2012) and not Zhang et al. (2010). The only model to have a domain including both the lower and middle atmosphere is Yung et al. (2009). However, Yung et al. (2009) primarily show species profiles from a model with the domain restricted to the middle atmosphere. The only species profile they show

from their extended model is OCS (Figure 2.2).

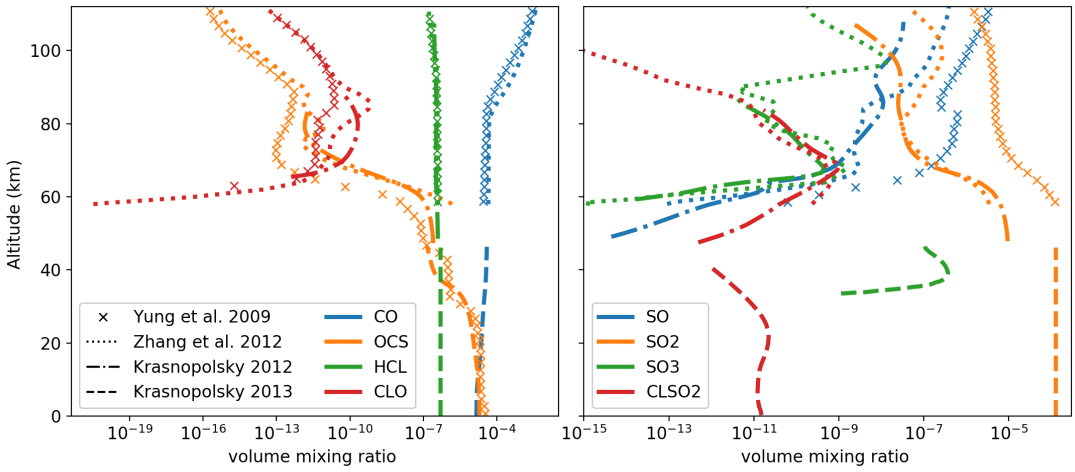

Figure 2.2: Comparison of previous chemical models of the Venusian atmosphere. The curves from Zhang et al. (2012) are their Model A. In Krasnopolsky (2013) SO_3 is only reported for values larger than 10^{-9}.

Figure 2.2 shows species profiles from the studies described above. Within a given domain (lower or middle) of the atmosphere, the different models are generally in agreement. The exception to this is the SO_2 profile of Yung et al. (2009) which exceeds the observed mixing ratio by nearly two orders of magnitude at 80 km. The middle atmosphere models of Zhang et al. (2012) and Krasnopolsky (2012) reproduce these observations by dramatically lowering their lower boundary condition (Table 2.1).

The greatest disagreement between previous models is at the boundary between the lower and middle atmosphere. This disagreement is modest for CO and OCS and is most significant for the sulfur oxides. In the lower atmosphere models, SO and $(SO)_2$ are often not even included or are included only in a limited capacity. We discuss how this effects the OCS chemistry in Section 2.3.2. Lower atmosphere models do not

predict any vertical gradient in SO_2 and as such report constant values around the observed 130 ppm (Marcq et al., 2006; Arney et al., 2014). To match the low mixing ratio observed in the middle atmosphere, models such as Zhang et al. (2012) and Krasnopolsky (2012) use a fixed abundance lower boundary condition of less than 10 ppm. It is these inconsistencies that motivate the need for models like the one presented here that can characterize the flux of SO_x species through the cloud layer (discussed in Section 2.3.1).

Table 2.1: Mixing ratios of SO_2 at the cloud level model boundary in different lower and middle atmosphere models. For the three middle atmosphere models this is simply the lower boundary condition. In the lower atmosphere models this value is calculated, but is the same as the surface boundary condition as there is no significant chemistry. Note that the model of Yung et al. (2009) which uses a higher SO_2 concentration also produced an SO_2 abundance two orders of magnitude larger than observations in the middle atmosphere.

Reference	Domain	SO_2 (ppm)
Krasnopolsky (2007)	0-47 km	130
Krasnopolsky (2013)	0-47 km	130
Krasnopolsky (2012)	47-112 km	9.7
Zhang et al. (2012)	58-112 km	3.5
Yung et al. (2009)	58-112 km	130

2.2 Model Description

For this study we use the JPL/Caltech kinetics 1D photochemisty-diffusion model (Yung and Demore, 1982; Mills, 1998; Zhang et al., 2012). Our model solves a 1D continuity equation with diffusion and chemical reactions. The atmosphere is assumed to be in hydrostatic equilibrium. We use 2 km grid cells covering 0-112 km. We calculate the diurnally averaged radiation field from 100 to 800 nm using a modified

radiative transfer scheme including gas absorption, Rayleigh scattering by molecules, and Mie scattering by aerosols with wavelength-dependent optical properties (Zhang et al., 2012). We also parameterized an additional UV opacity source in the radiative transfer calculation contributed by the unknown UV absorber (see Zhang et al. (2012) for details). Our calculations are set at 45° latitude with fixed solar insolation to approximate the global-mean situation.

We use the Venus International Refrence Atmosphere (VIRA) (Seiff et al., 1985) (Figure 2.3). Because observational constraints for the eddy diffusivity (k_{zz}) are sparse, a number of k_{zz} profiles have been used in the literature. For our nominal model configuration we use the profile from Zhang et al. (2012) linearly extrapolated in log space into the lower atmosphere. For a description of the other k_{zz} profiles used and their motivations see Section 2.2.2.

In this work we calculate the vertical profile of 53 species: O, O($^1\Delta$), O_2, O_2($^1\Delta$), O_3, H, H_2, OH, HO_2, H_2O_2, N, NO, NO_2, NO_3, N_2O, HNO, HNO_2, HNO_3, Cl, Cl_2, ClO, HCl, HOCl, ClCO, $COCl_2$, $ClCO_3$, CO, CO_2, S, S_2, S_3, S_4, S_5, S_6, S_7, S_8, SO, $(SO)_2$, SO_2, SO_3, S_2O, SH, H_2S, HSO_3, ClSH, ClS, ClS_2, Cl_2S, Cl_2S_2, OSCl, $ClSO_2$, SO_2Cl_2, OCS. Additionally we have three species with fixed profiles,N_2, H_2O, and H_2SO_4 (shown in Figure 2.4). N_2 is fixed at a mixing ratio of 3.4%. N_2 acts as a catalyst in some reactions and is a source of N via photolysis. H_2O and H_2SO_4 are also held constant as both species are condensible but condensation is not included in this model. In addition, as noted by Parkinson et al. (2015), in the middle atmosphere the H_2O and SO_2 abundances are strongly coupled. While the specific bifurcation

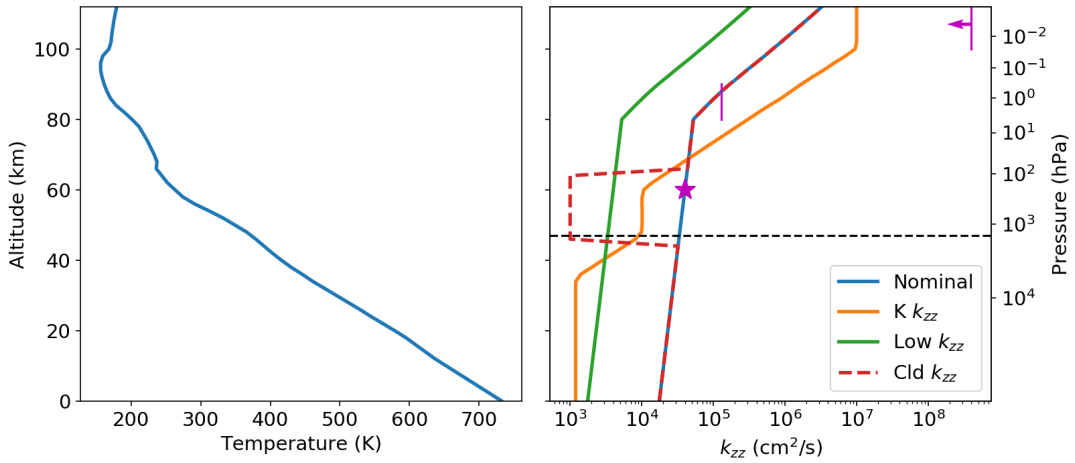

Figure 2.3: Left panel: Temperature profile from Seiff et al. (1985). Right panel: k_{zz} profiles used in this study. The Zhang et al. (2012) K_{zz} profile has been extrapolated into the lower atmosphere (Nominal). The other k_{zz} profiles are described in Section 2.2.2. The horizontal dashed line at 47 km indicates the boundary between the middle-atmosphere model in Krasnopolsky (2012) and the lower-atmosphere model in Krasnopolsky (2013). Observational estimates of k_{zz} are shown in magenta (upper limit (von Zahn et al., 1979), star (Woo and Ishimaru, 1981), and line (Lane and Opstbaum, 1983)).

behavior described by Parkinson et al. (2015) was due to numerical errors, the strong coupling is robust (Shao et al., In Review). By holding the water profile constant (at observed values) we remove this source of sulfur variability. The water profile used is a spline interpolation to the observational results from Bertaux et al. (2007) in the middle atmosphere and Marcq et al. (2006), Barstow et al. (2012), and Arney et al. (2014) in the lower atmosphere (see Figure 2.4).

The H_2SO_4 profile is fixed at the saturation vapor pressure assuming 90% weight percent H_2SO_4 above 57 km. This is consistent with observation of cloud acidity (Barstow et al., 2012; Arney et al., 2014). Our model is not very sensitive to this value

as H_2SO_4 is not a significant chemical source in the upper atmosphere. Below 47 km (at the base of the lower cloud) we use the profile calculated by Krasnopolsky (2013). Between 47 km and 57 km the H_2SO_4 profile is linearly interpolated in log space. The resulting profile shown in Figure 2.4 is consistent with the upper limits by Sandor et al. (2012) in the middle atmosphere and the Venus Express observations at the base of the clouds (Oschlisniok et al., 2012). The effect of this profile is discussed in detail in Section 2.3.1.

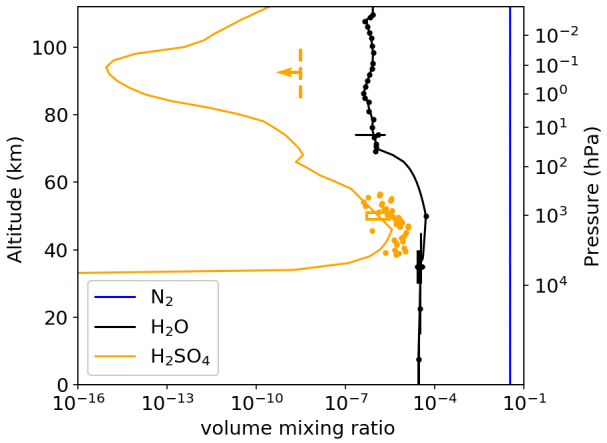

Figure 2.4: Profiles of all fixed species in the model and corresponding observations. H_2SO_4 upper limit is obtained from Sandor et al. (2012) and observed abundance from Oschlisniok et al. (2012) and Imamura et al. (2017). Water vapor observations are from Marcq et al. (2006), Bertaux et al. (2007), Krasnopolsky (2010b), Barstow et al. (2012), and Arney et al. (2014).

In order to couple the chemical systems in the middle and lower atmospheres, one needs to include both the photochemistry in the middle atmosphere and the high-temperature thermochemistry with both forward and reverse reactions in the lower atmosphere. In this study we have updated the chemistry of Zhang et al. (2012) to

include new experimental results as described in Burkholder et al. (2015) and the lower atmosphere chemistry of Krasnopolsky (2013). These updates to the chemistry have a negligible effect on our model compared directly with Zhang et al. (2012). In Section 2.4 we discuss which reactions with unconstrained reaction constants have the largest impact on our results.

2.2.1 Boundary conditions

For most species in our model we use a zero flux (closed box) boundary condition at both the upper and lower boundary. This is consistent with the standard setting for previous lower and middle atmosphere models (Krasnopolsky, 2007, 2012; Zhang et al., 2012). In a model with a zero flux boundary condition for all species, the resulting steady state solution is highly sensitive to the initial condition. This is due to the fact that the total abundance of each group is set by the initial condition. To avoid this, at least one species in each group was assigned a fixed mixing ratio at the lower boundary. We preferentially chose species that have observational constraints on their abundance. This allows the abundance of each chemical group to equilibrate to the observed values through surface fluxes. The upper boundary conditions used in this model follow the work of Mills (1998). Upward fluxes of CO_2, O_2, and $O_2(^1\Delta)$ are imposed at the upper boundary to account for photolysis taking place above the model boundary. We use the fluxes calculated by Mills (1998). In order to conserve the number of atoms in the domain, downward fluxes of CO and O of the same magnitude as the loss of CO_2 are also imposed at the upper boundary.

Table 2.2: Boundary conditions applied to the model. Φ is the flux (cm^2 s^{-1}), v is the escape velocity (cm s^{-1}) where v_m is the maximum escape diffusion velocity, and χ is a fixed mixing ratio. The boundary condition for all other species is zero flux. The sign convention is positive upwards.

Species	Lower	Upper
O	$\Phi = 0$	$\Phi = -5.030 \times 10^{11}$
O_2	$\Phi = 0$	$\Phi = 9.0 \times 10^8$
$O_2(^1\Delta)$	$\Phi = 0$	$v = v_m$
NO	$\chi = 5.5 \times 10^{-9}$	$\Phi = 0$
CO	$\chi = 1.5 \times 10^{-5}$	$\Phi = -5.03 \times 10^{11}$
CO_2	$\chi = 0.965$	$\Phi = 5.03 \times 10^{11}$
SO_2	$\chi = 1.0 \times 10^{-4}$	$\Phi = 0$
OCS	$\chi = 3.0 \times 10^{-5}$	$\Phi = 0$

2.2.2 Modifications to our nominal case

To discuss the sensitivity of our results to different changes in our nominal model it is useful to name particular cases we will refer back to. Here we describe those alternate cases in the sensitivity study. The alternate k_{zz} profiles are shown in Figure 2.3.

- **K** k_{zz}: Uses the combined k_{zz} profiles from Krasnopolsky (2012) and Krasnopolsky (2013).

- **Low** k_{zz}: Uses our nominal k_{zz} profile but reduced by one order of magnitude. We present this profile not because it is a plausible k_{zz} profile but because it is instructive for understanding the model sensitivity.

- **Clould (Cld)** k_{zz}: It was suggested by Marcq et al. (2017) that the cloud layer may inhibit transport. This profile tests a stable cloud region by using our nominal k_{zz} profile modified to a value of 10^3 cm^2/s between 45 km and 65 km.

- **S_8**: Changes the upper boundary condition of S_8 to $\Phi = -1 \times 10^7$. This polysulfur flux from the upper atmosphere was proposed by Zhang et al. (2012) to explain the SO_2 inversion in the middle atmosphere.

- **K OCS**: Uses the reaction rate constant for $OCS + SO_3 \longrightarrow CO_2 + (SO)_2$ from Krasnopolsky (2007).

2.3 Results

2.3.1 SO_x

Discussing SO_x in the Venusian atmosphere is nearly equivalent to discussing SO_2. SO_2 is the most abundant, most stable and best observed of the SO_x group everywhere except the highest altitudes. Using our nominal k_{zz} profile, the chemical transport timescale ranges from ∼10 years near the surface to months at 90 km (Figure 2.5). The chemical loss timescale for SO_2 exceeds ∼100 years until photolysis begins to dominate in the upper middle atmosphere. As such, SO_2 is well mixed from the lower boundary of the model until the base of the clouds.

In contrast to SO_2, SO and SO_3 have chemical loss timescales of hours or less throughout the model domain. In the lower atmosphere, where there are no significant sources of these species, this leads to mixing ratios below 1 ppt. Above the cloud deck their abundance is set by the relative contributions of oxidation and photochemical destruction. The source of oxygen for these reactions is primarily derived from the photolysis of CO_2 and SO_2.

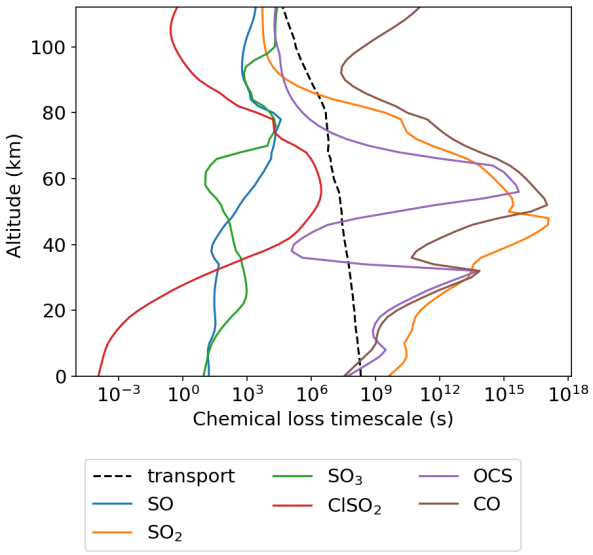

Figure 2.5: Chemical loss timescales for different SO_x species and the transport timescale profile. All profiles are for the nominal model configuration. The local minimum in the OCS lifetime corresponds to the region with excess SO_3 at the base of the clouds (Figure 2.7).

Here we quantitatively examine the sulfur flux exchange between the lower and middle atmospheres through the clouds, as illustrated in Fig. 2.1. The primary reservoirs of sulfur below 35 km are SO_2 (∼100 ppm) and OCS (∼30 ppm), both of which have fixed mixing ratios at the surface. There may be a few ppm S_x present, however, currently there is no direct observational evidence for this (see section 2.3.5). Right above 35 km, the observed rapid decrease of OCS suggests a rapid conversion from OCS to SO_x or S_x, which will be discussed in Section 2.3.2. As a result the primary source of sulfur into the middle atmosphere through the clouds is SO_2. The magnitude of this flux is set by the observed SO_2 mixing ratio and k_{zz} profile. In our nominal case, the upward flux of the SO_2 through the clouds (59 km) is $5{\times}10^{11}$ cm^{-1} s^{-1}. The value

ranges from 5×10^{11} cm^{-1} s^{-1} to 10×10^{11} cm^{-1} s^{-1} across all of our cases.

Above the cloud, SO_2 is converted to SO and SO_3 via photochemistry. The downward fluxes of SO and SO_3 to the lower atmosphere are negligible due to their short loss timescales. The main sink of SO_x is sulfuric acid formation ($SO_3 + 2H_2O \longrightarrow H_2SO_4 + H_2O$). The entire H_2SO_4 formation process is primarily limited by SO_3 formation which is itself primarily limited by the SO_2 flux. Thus among our model configurations the column integrated production rate of H_2SO_4 above 59 km shows little variation and tracks with the SO_2 flux. Values range from 5×10^{11} to 9×10^{11} cm^{-2}s^{-1}, which is in line with previous results by Zhang et al. (2012) (5.6×10^{11} cm^{-2}s^{-1}) and Krasnopolsky (2015) (5.7×10^{11} cm^{-2}s^{-1}). The H_2SO_4 produced in the middle atmosphere rapidly condenses to form the bulk of the Venus clouds. Cloud droplets settle into the lower atmosphere where they evaporate releasing H_2SO_4 vapor. This vapor further thermally decomposes into SO_3 and H_2O. This SO_3 is rapidly converted to SO_2 creating a source region of SO_2 at the cloud base. Then the long-lived SO_2 from the base of the clouds is diffused away from this source to complete the sulfur cycle.

In our nominal model configuration the SO_2 mixing ratio approaches that of a well-mixed profile with minimal vertical gradient, inconsistent with the observations from Venus Express (Belyaev et al., 2008, 2012). This problem was not observed in previous middle atmosphere models because they could limit the flux by fixing the mixing ratio of SO_2 in their lower boundary condition (located in the cloud deck). As shown in Table 2.1, the models that successfully reproduce the SO_2 minima (Zhang et al., 2012; Krasnopolsky, 2012) require a lower boundary condition of less than 10 ppm.

The only model with a lower boundary condition consistent with the lower atmosphere observations is Yung et al. (2009). Their model (like ours) does not match the middle atmosphere observations.

There are two way to overcome this issue, decreasing the SO_2 transport or increasing the chemical sink in the cloud layer. Two of our k_{zz} profiles attempt to limit the transported SO_2: *Cloud* k_{zz} and *Low* k_{zz}. *Cloud* k_{zz} is based on the suggestion from Marcq et al. (2017) that SO_2 transport is inhibited by a stable cloud layer. This profile has a value of 10^3 cm^2/s between 45 and 65 km (shown in Figure 2.3). Additionally we use the *Low* k_{zz} profile which has a k_{zz} lower than our nominal case by an order of magnitude throughout the domain. Both the *Cloud* k_{zz} and *Low* k_{zz} models come close to matching the observed SO_2. It is worth noting that in both of these cases the flux of SO_2 at 59 km is actually twice that of the nominal case due to the large mixing ratio gradient. This gradient leads to a much lower SO_2 mixing ratio at the cloud tops which in turn allows the radiation to penetrate deeper into the middle atmosphere. This further lowers the mixing ratio. In other words, it is the mixing ratio of SO_2 at the cloud top that is important, not the flux.

Figure 2.7 shows that the observed SO_2 profile can be matched allowing for any arbitrary amount of transport. This raises an important question: how plausible are these particular k_{zz} profiles? Both of these profiles are inconsistent with the radio scintillation estimate as 4×10^4 cm^2/s at 60 km (Woo and Ishimaru, 1981) and 2×10^3 cm^2/s at 45 km (Woo et al., 1982). From the mixing length theory, k_{zz} can be estimated as the product of vertical velocity and a length scale. Imamura and Hashimoto (2001)

used velocities from both models and the Vega balloons to estimate a cloud region k_{zz} of $10^4 - 10^6$ cm^2 s^{-1}. The value seems even larger between 50-60 km. Using the turbulent velocity on the order of 1 m/s measured by Vega balloon at 54 km (BLAMONT et al., 1986) and the mixing length scale of 1 km, the estimated k_{zz} is about 10^7 cm^2 s^{-1}. Based on the static stability profiles from the Pioneer Venus probes, which are consistent with the VeRa/VEx data (Limaye et al., 2018), McGouldrick and Toon (2007) estimated the k_{zz} between 10^4 and 10^7 cm^2 s^{-1} in the cloud region. These values have been validated by cloud micro-physical models which are sensitive to the k_{zz} to match the observed cloud droplet size distribution (McGouldrick and Toon, 2007; Gao et al., 2014). These values are higher than our *Cloud* k_{zz} and *Low* k_{zz} configurations by at least a factor of three. Even using the low end of these plausible values of k_{zz} (i.e., 10^4 cm^2 s^{-1}) cannot reproduce the observed SO2 data, as already shown in our *K* k_{zz} configuration. This implies that the low SO_2 mixing ratio above the clouds is due to some as of yet unknown chemical sink in the cloud region or interactions with the cloud droplets. This also highlights the need for 2D and 3D dynamical models to quantify the transport in greater detail, as the k_{zz} is a global-mean approximation of the 3D dynamical transport (Zhang and Showman, 2018a,b).

An important caveat in our results is the artificial source of sulfur as a result of the fixed H_2SO_4 vapor profile. As our model does not include cloud formation and so the gas H_2SO_4 abundance cannot be self consistently calculated. Instead the H_2SO_4 profile is held to the profile expected from condensation and evaporation, (Figure 2.4). This parameterization can be checked for self-consistency by comparing the net production

and loss rates. Figure 2.6 shows the production and loss reaction rates as well as the net production minus loss for H_2SO_4. Although the total column formation and destruction rates of H_2SO_4 are both roughly 4.4×10^{16} $cm^{-2}s^{-1}$, the column destruction rate is a bit higher than production by ∼0.2% in all our model configurations. This slight excess in H_2SO_4 destruction over production impacts the lower atmosphere sulfur budget. As noted above, the evaporation of sulfuric acid and conversion from SO_3 and SO_2 at the cloud base provides a SO_2 source, which needs to be diffused away, both upward and downward in our model. The downward diffusion flux goes into the surface to satisfy the lower boundary condition (fixed mixing ratio, Table 2.2). Because the production and loss of H_2SO_4 are not exactly equal, our model uses this boundary condition to achieve steady state. Across our model configurations this downward flux of SO_2 ranges from 6×10^{12} to 1×10^{14} molecules cm^{-2} s^{-1}. These are much larger than the 1×10^9 to 1×10^{11} molecules cm^{-2} s^{-1} suggested as plausible rates for surface reactions Fegley et al. (1997). These change very little even for large changes in the H_2SO_4 profile (see Text S1). To properly model the lower atmosphere flux of SO_2 will require a model that can fully conserve sulfur. In any model that does not conserve sulfur the lower boundary will numerically accommodate the excess.

In addition to the sulfur cycle discussed above, there might be an additional source of sulfur from the upper atmosphere. Such a source was proposed by (Zhang et al., 2010, 2012) in order to explain the increase of SO and SO_2 with altitude above 80 km. In this work we parameterize this as a poly-sulfur (S_8) flux from the model upper boundary as proposed by Zhang et al. (2012). It is only in the runs with this polysulfur

flux that we observe any inversion. However, because we have an over abundance of SO_x in the middle atmosphere generally this model should not be used to quantify the required flux.

We also use our model to examine a recently proposed candidate for the unknown UV absorber in the Venusian atmosphere. Frandsen et al. (2016) suggested that $(SO)_2$ could be the unknown UV absorber (Esposito, 1980). In creating their simple model to estimate the $(SO)_2$ abundance they assume either a 12 ppb or 20 ppb mixing ratio at their lower boundary (58 km). In contrast we find that at 58 km $(SO)_2$ is essentially non-existent (mixing ratio less than 10^{-25}). The concentration does increase higher in the atmosphere but never exceeds 1 ppb. In the model configuration that best matches the observed SO_2, low k_{zz}+S_8, the $(SO)_2$ abundance never exceeds even 1 ppt. The mixing ratio also peaks at ∼90 km altitude, far above the cloud tops where the UV absorber is observed. In summary, our results are consistent with the findings of Krasnopolsky (2018) and Marcq et al. (2020) suggesting that $(SO)_2$ is not abundant enough to be the main UV absorber.

2.3.2 CO and OCS

This section is an overview of the carbon cycling in Venus's atmosphere. While CO_2 is the most abundant carbon species throughout the atmosphere, the carbon flux is primarily controlled by CO and OCS in conjunction with CO_2.

There are two primary sources of CO, photolysis of CO_2 in the middle atmosphere and conversion from OCS in the lower atmosphere. Figure 2.9 shows the impor-

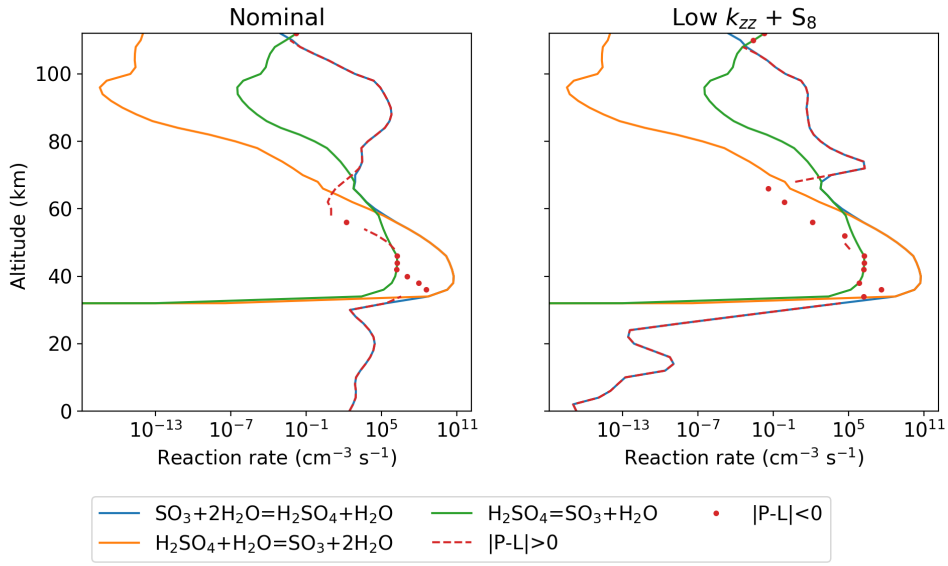

Figure 2.6: Profiles for the production and loss reaction rates of sulfuric acid for two model configurations. The red curve shows the net production minus loss where dashed lines indicate local H_2SO_4 production and dots indicate local loss. In both cases H_2SO_4 is primarily produced in the zone of SO_2 photolysis.

tant production and loss reactions of CO at each altitude in addition to the production and loss profiles. In our nominal case, above 59 km CO photolysis (CO_2=CO + O + M) has a column rate of 10×10^{11} cm^{-2} s^{-1} taking place primarily above 85 km. This plus the CO from the upper boundary (5×10^{11} cm^{-2} s^{-1}, Table 2.2) is transported downward with a nearly constant flux of 14×10^{11} cm^{-2} s^{-1}. The difference between this photochemical production and flux is due to slow reoxidation by OH (column rate 1×10^{11} cm^{-2} s^{-1}). These rates can vary by an order of magnitude between our different k_{zz} profiles. This sensitivity is largely due to the different radiation environment created by the varying SO_2 abundance (Figure 2.7). This leads to the different CO mixing ratio profiles shown in Figure 2.10. Regardless of the value, in all of these cases

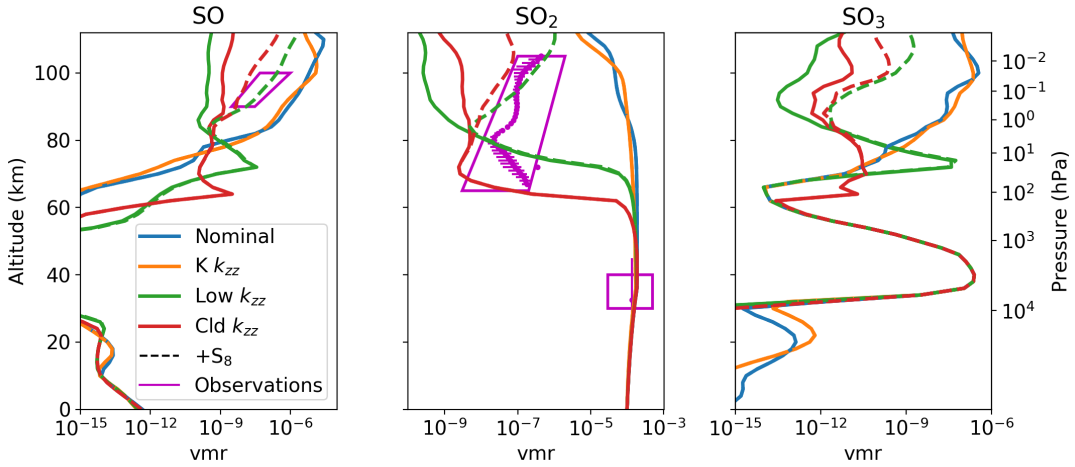

Figure 2.7: Observations and model results of SO_x. Observed SO and SO_2 are shown by in magenta. The middle atmosphere boxes denote the variability in SO and SO_2 observed by the SPICAV solar occultation instrument on Venus Express (Belyaev et al., 2012; Vandaele et al., 2017). The individual points show a typical observed profile from Belyaev et al. (2012) to show the shape of the observed SO_2 profile. The one middle atmosphere SO_2 point outside the box is from Krasnopolsky (2010b). Lower atmosphere box shows the variation in SO_2 measured by VIRTIS on Venus express (Vandaele et al., 2017). Individual lower atmosphere measurement from (Arney et al., 2014). Model configurations with varying k_{zz} are shown in the various colors. For each k_{zz} the run including a flux of S_8 from the upper boundary is shown with a dashed line. For some of these model configurations, the dashed line is on top of the solid line (hence is not visible) because the SO_2 flux from the lower atmosphere dominates. The exception are the *Low* k_{zz} and *Cloud* k_{zz} configurations. The is because the significantly lower SO_2 mixing ratio allows the high altitude oxidation of S_x species to make a significant impact on the profile.

this downward flux of CO in the middle atmosphere is matched by an upward flux of CO_2, closing the cycle.

In the lowest 30 km of the atmosphere, CO and OCS are cycled between each other. This cycling is mediated by S and S_2 (Figure 2.9). In all of our model configurations, OCS is diffused upwards from the lower boundary with a flux between 5×10^{12} and 5×10^{13} molecules/cm^2. In each case, this flux is matched by a comparable downwards

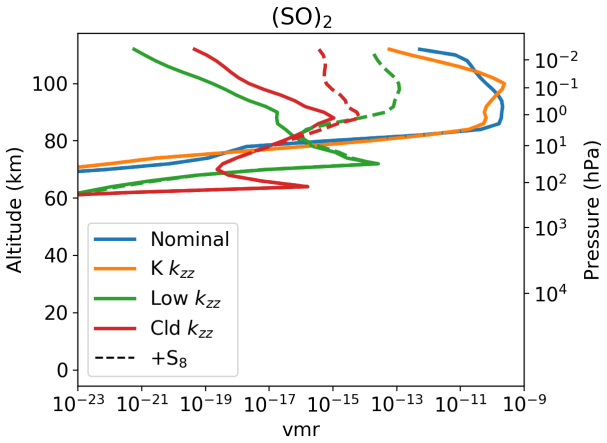

Figure 2.8: Profiles of $(SO)_2$ for the same cases as are shown in Figure 2.7.

flux of CO towards the surface. As with the middle atmosphere, the absolute value of these fluxes is dependent on the k_{zz} in the lower atmosphere which is not observationally constrained. This balance in fluxes implies some surface chemistry moderating CO and producing OCS (Zolotov, 2018, and the references within).

In all our model configurations, CO is converted back to CO_2 in the cloud region via

$$CO + SO_3 = CO_2 + SO_2 \tag{R1}$$

The rate constant used for this reaction was assumed by Krasnopolsky and Pollack (1994) using analogy to $CO + NO_2$=$CO_2 + NO$. The high abundance of SO_3 in the lower cloud region makes this reaction very fast and effectively prevents exchange of CO between the middle and lower atmosphere.

CO may also be rapidly produced in the cloud region by OCS-SO_3 chemistry. The observed decrease in OCS mixing ratio at 35 km is coincident with the bottom of the

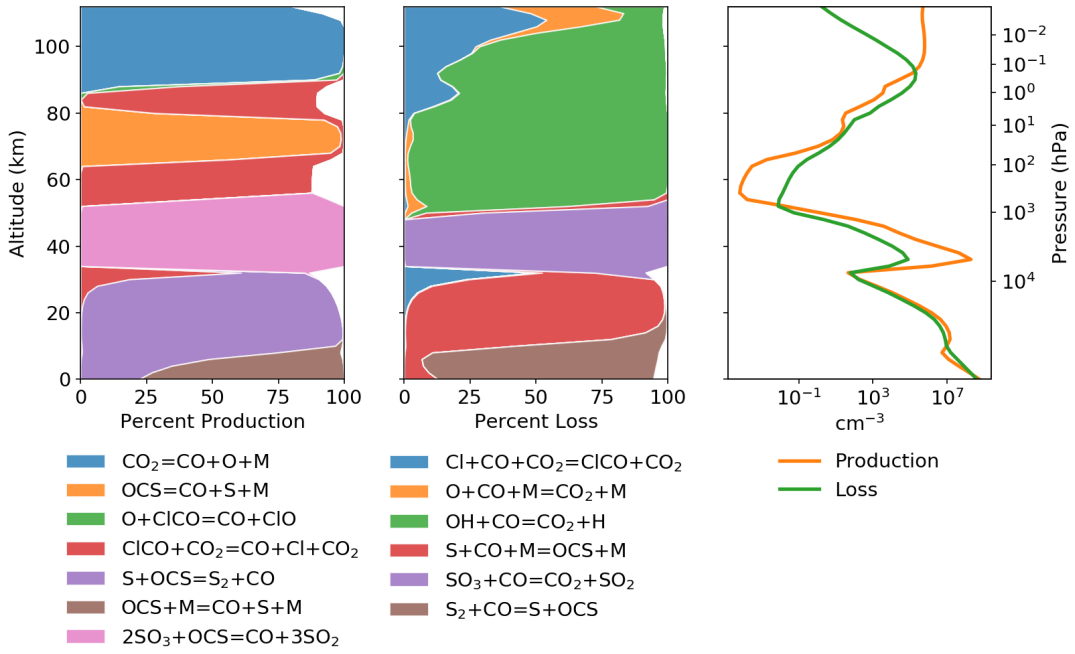

Figure 2.9: CO production and loss for our nominal case. Left two panels show the percentage of the production or loss that is due to a particular reaction. Unfilled (white) space is due to reactions not listed. All reactions that contribution at least 20% at any altitude are shown. Right panel shows the absolute production and loss curves for CO. In the *K OCS* model configurations (not shown), loss exceeds production at 40 km due to the absence of Reaction R5.

cloud deck. Because of this there is a local excess of SO_3 from the thermal decomposition of H_2SO_4. This leads to the natural hypothesis that there is some reaction between SO_3 and OCS driving this reduction. Krasnopolsky and Pollack (1994) calculated the free energy associated with possible products of SO_3 + OCS and found they are all endothermic. The least endothermic was

$$SO_3 + OCS = CO_2 + (SO)_2 \tag{R2}$$

Krasnopolsky and Pollack (1994) further suggested that the OCS destruction would be

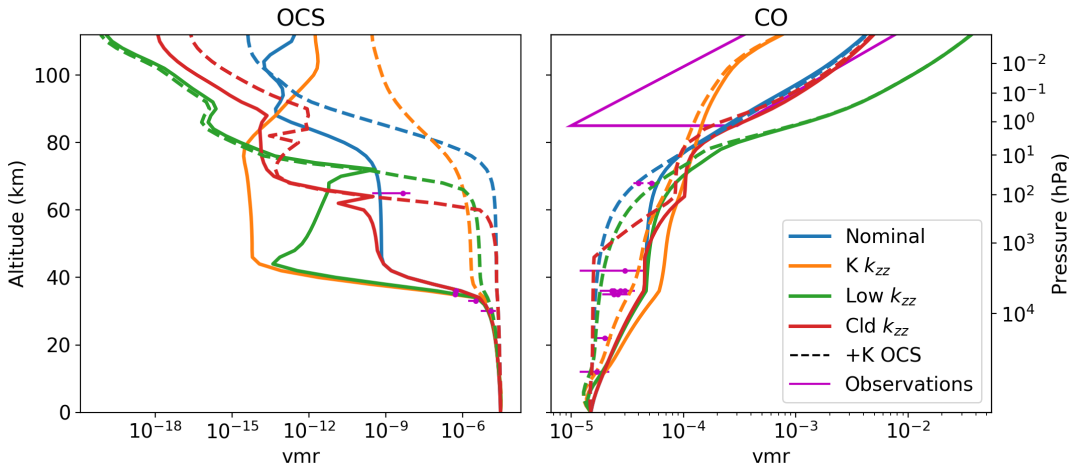

Figure 2.10: Profiles of OCS and CO for different model configurations. These profiles are not sensitive to the upper boundary S_8 flux. CO observations are shown by the magenta box (**?**).

enhanced by the secondary reaction

$$(SO)_2 + OCS = CO + SO_2 + S_2 \tag{R3}$$

This set of reactions has since been used in followup models of Venus's lower atmosphere (Krasnopolsky, 2007, 2013) but has yet to be measured in the lab. This pathway was tested in our *K OCS* model configuration.

In the lower atmosphere models of Krasnopolsky (2007) and Krasnopolsky (2013), R2 and R3 are the only reactions that feature $(SO)_2$. Because of this, $(SO)_2$ will build up in their models until reaction R3 has the same rate as reaction R2. In contrast, our model includes reactions that equilibrate $(SO)_2 \rightleftarrows 2\,SO$ using the rates estimated by Mills (1998). As a result, $(SO)_2$ does not build up and reaction R3 is effectively halted. This has two effects: it dramatically reduces the OCS destruction rate and interrupts the pathway converting OCS to CO. Because of this, none of the models

using *K OCS* fit the observed OCS observations (Figure 2.10). This could potentially be remedied by dramatically increasing the rate coefficient of Reaction R2. However, such a modification would still not allow for the efficient conversion of OCS to CO.

Yung et al. (2009) proposed that the primary OCS destruction pathway is

$$S + OCS = CO + S_2 \tag{R4}$$

This reaction rate has been measured in the lab (Lu et al., 2006), yet it is still difficult to test the impact of this reaction on OCS abundances due to the poor knowledge of S_x chemistry. As discussed in section 2.3.5 the S_x chemistry is some of the most uncertain in the entire model. In our model this reaction is insufficient to reproduce the OCS observations because the concentration of atomic sulfur is five orders of magnitude lower than what was proposed by Yung et al. (2009). There is also no apriori reason why atomic sulfur would be concentrated at the base of clouds, leading to the observed drop in OCS concentration at that particular altitude. Indeed in our model this reaction is fastest within 30 km of the surface, not at 35 km where the OCS mixing ratio declines (Figure 2.9). This does not rule out this mechanism, however, as a better understanding of S_x chemistry is needed to definitively test it.

In this work we propose a new pathway for OCS destruction. The reaction

$$2\,SO_3 + OCS = 3SO_2 + CO \tag{R5}$$

is exothermic in contrast to R2. It is a three body reaction and so would likely require some unknown intermediate steps. To estimate the rate constant we propose that it is similar to that of other 3 body reactions with $k = 3 \times 10^{-32}$ s^{-1} cm^{-3}. As shown in

Figure 2.10 this allows us to match the observed OCS profile. The observed value of OCS above the clouds can also be achieved given some tuning of this rate constant and the k_{zz} profile. While we favor reaction R5 we also note that, as with reaction R2, this pathway has not been verified either by lab studies or ab-initio calculations.

Due to reaction R5, our model does produce an increasing CO mixing ratio with altitude in the lower atmosphere but overshoots the observed values. As noted above, the vertical profile of CO is more sensitive to the k_{zz} profile than many other species and the chemistry in the cloud region is dominated by reactions with unmeasured rate constants. It is possible that future work could use this sensitivity of CO to constrain the k_{zz} of Venus's atmosphere, however better chemical rate constants are first required.

2.3.3 O_x

A long-standing problem with middle atmosphere photochemistry models of Venus is the overabundance of O_2 when compared to observations. In the middle and upper atmosphere, atomic oxygen is primairly produced by the photodissociation of CO_2 and SO_2. The direct recombination of CO and O to form CO_2 is much slower than photolysis, allowing atomic oxygen to accumulate. While there is no resolved vertical profile for any O_x species, there are upper limits on the column abundance above the cloud deck of O_2 that range from 0.8×10^{18} to 10×10^{18} cm^{-2} (Marcq et al., 2017). Our model configurations produce O_2 column abundance values between 5 and 200×10^{18} cm^{-2}. The lower end of these are values ($\sim 5 \times 10^{18}$ cm^{-2}) correspond to the model configurations that come closest to matching the SO_2 observations and are consistent

with previous middle atmosphere models.

O_3 has also been observed in the Venusian atmosphere with a mixing ratio of 0.11 ppm at 100 km (Montmessin et al., 2011). In contrast to O_2, O_3 mixing ratios in our model configurations are consistently below these observed levels. At 100 km most model configurations have ∼0.04 ppm O_3, consistent with Zhang et al. (2012). The outlier was the *K* k_{zz} configuration which had $\sim 10^{-5}$ ppm. This is because, with the *K* k_{zz} profile, the O_3 mixing ratio peaks at ∼0.01 ppm at 90 km and declines steeply at higher altitudes. This is consistent with the results presented in Krasnopolsky (2012).

For both O_2 and O_3 our *Low* k_{zz} configuration matches previous model results but diverges from the observations. Recent reanalysis of Venus Express observations has found cloud top O_3 mixing ratios of 10 to 20 ppb concentrated in the polar regions (Marcq et al., 2019). These values were also observed to vary with local time and year to year. This may suggest that understanding the oxygen observations will require 2D or 3D models that include transport in the middle and upper atmospheres. Alternatively the fact that O_2 is overabundant while O_3 is under-abundant may imply some important, but yet unknown, oxygen chemistry in the Venusian atmosphere.

2.3.4 Chlorides

The only chloride species with observed abundances are HCl (Arney et al., 2014; Krasnopolsky, 2010a; Sandor and Clancy, 2012; Mahieux et al., 2015; Sandor and Clancy, 2017) and ClO (Sandor and Clancy, 2018). In both the lower and middle atmosphere HCl is observed to have a mixing ratio of ∼400 ppb although cloud top

abundance have been observed as low as 100 ppb (Sandor and Clancy, 2012). This near constant mixing ratio is consistent with our model results (Figure 2.11). The only inflection seen in our model is above 90 km where photolysis begins to become important. This acts as a source of chlorine in the upper middle atmosphere producing a variety of other species.

Sandor and Clancy (2017) observed a decline in the HCl mixing ratio in the upper middle atmosphere with altitude. The gradient reported by Sandor and Clancy (2017) is steeper than our steady state solution. Sandor and Clancy (2017) also note that there appear to be secular variations of up to ∼300 ppb that occur on timescales of a month and do not appear correlated with local time. The difference between our model and these observations could be due to the temporal variations in HCl in Venus's atmosphere or a discrepancy between the true HCl photolysis rate and that calculated by the models.

The observations of Sandor and Clancy (2017) are in conflict with the Venus Express observations analyzed by Mahieux et al. (2015). Mahieux et al. (2015) found a cloud top value of 100 ppb increasing to 1 ppm at 110 km. They also found this increasing mixing ratio with altitude was not sensitive to latitude or local time. Such a profile would require some high altitude chlorine source which is not included in this work.

The observations of ClO by Sandor and Clancy (2018) have a mixing ratio of ∼2 ppb at 85 km. This is four orders of magnitude higher than our nominal model values. This value is very sensitive to the photolysis rate of HCl. To illustrate this it is useful to

compare our nominal model configuration to the low k_{zz}+S_8 configuration. This case has significantly less SO_2 than the nominal model, making it in better agreement with the observed middle atmosphere SO_2 abundance (see Section 2.3.1). The low k_{zz}+S_8 has significantly more ClO, implying that the excessive amount of SO_2 in our nominal case shields the middle atmosphere from UV radiation and thereby limits the HCl photolysis rate. However, even the higher abundance of ClO in the low k_{zz}+S_8 model configuration is a factor of 3 below the observed value. This difference could be due to uncertainties of the model HCl photolysis rate, some unknown Cl source as proposed by Sandor and Clancy (2018), or as-yet unobserved temporal variability in ClO similar to HCl.

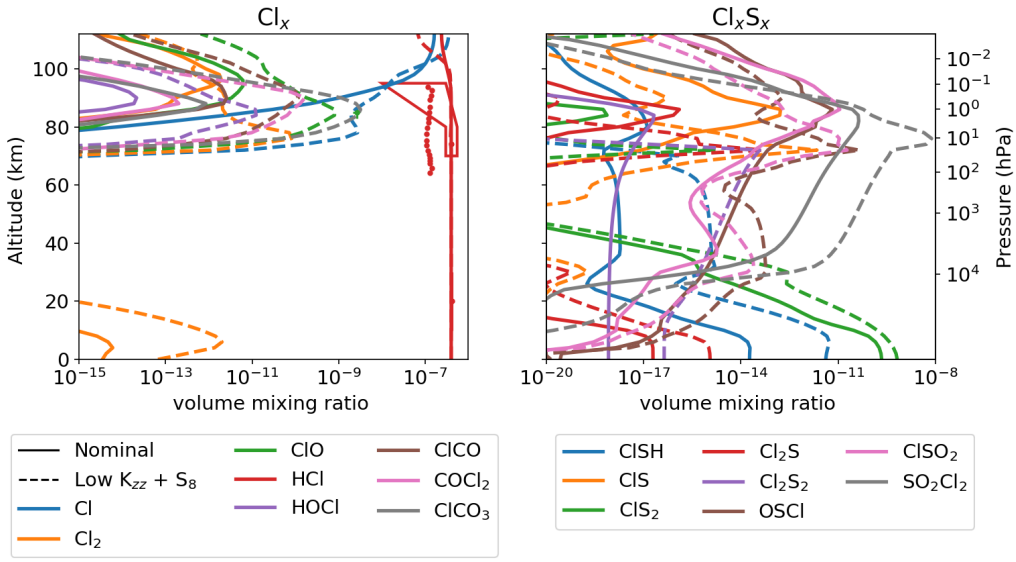

Figure 2.11: Model chlorine species results from our nominal and Low k_{zz}+S_8 configurations. Observations for HCl from Krasnopolsky (2010a), Sandor and Clancy (2012) (vertical profile) Arney et al. (2014), and Sandor and Clancy (2017) (boxed region). ClO observation from Sandor and Clancy (2018).

2.3.5 Other Species

Model profiles for NO_x species are presented in Figure 2.12. NO has been observed by Krasnopolsky (2006) and was interpreted to be sourced from lightning in the lower atmosphere. We find that any lower atmosphere NO mixing ratio is readily mixed into the middle atmosphere. This is consistent with Krasnopolsky (2006) but is agnostic to the source of NO in the lower atmosphere. No significant chemistry affects the NO_x species outside of photochemistry in our current model.

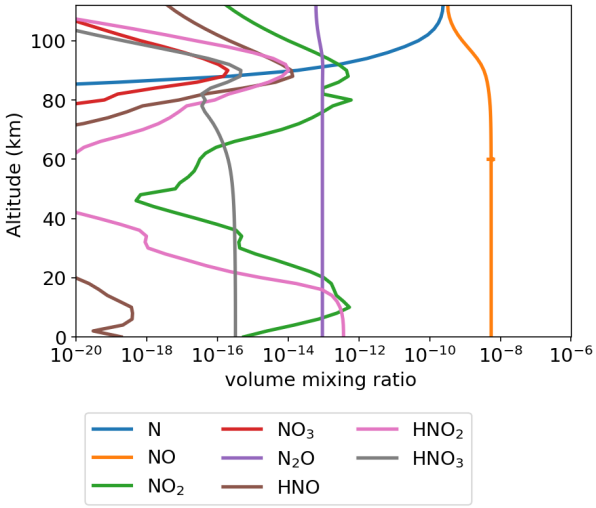

Figure 2.12: Nominal model profiles for the NO_x group. Observation of NO from Krasnopolsky (2006).

Figure 2.13 shows the model profiles for the S_x species. Data analysis of the Venera 11 spectra by Krasnopolsky (2013) has provided measurements for S_3 and S_4 abundance below the clouds. In that work an updated lower atmosphere model is also presented that can match these observations by including the photolysis pathway

$S_4 \longrightarrow S_3 + S$. The S_x chemistry is some of the least constrained in the entire model. The reactions used in this work come primarily from Moses et al. (2002) although those rate constants still lack experimental or ab-initio validation. While the pathway proposed by Krasnopolsky (2013) may be correct, more lab work is needed to properly understand this system.

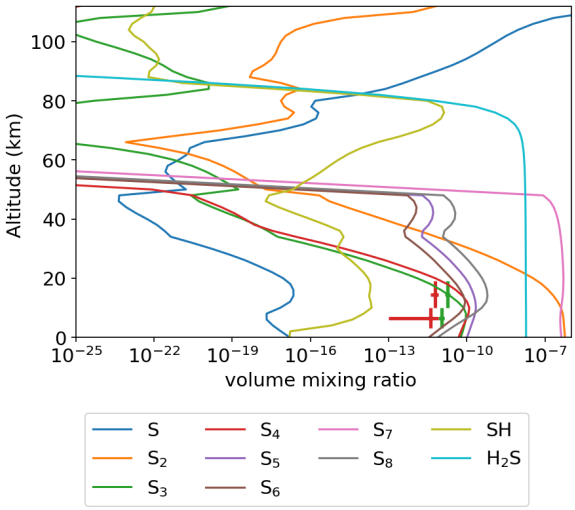

Figure 2.13: Nominal model profiles of S_x and reduced sulfur species. Observation for S_3 and S_4 from Krasnopolsky (2013).

2.4 Summary

In this work we perform the first detailed analysis of a Venus atmospheric chemistry model that extends from the surface through the middle atmosphere. We find that a large flux of SO_2 transported through the cloud layers, independent of the eddy diffusivity profile, prevents the model from matching the low SO_2 observed around

75 km. We suggest that there is either some unknown chemical sink in the cloud region or that interactions with the cloud droplets themselves prevent the transport of SO_2. We also propose a new chemical pathway by which SO_3 below the cloud deck could convert OCS to CO. In the preceding sections we have detailed how each chemical system behaves, however it is equally important to understand how these systems interact. These systems and interactions are summarized in Figure 2.1. In this section we also present a summary of outstanding questions raised by this model and the highest priority laboratory studies that could help address them.

The base of the clouds is one of the most chemically active regions in the Venusian atmosphere. The excess SO_3 released from the thermal decomposition of H_2SO_4 is highly reactive as it finds pathways to form the more stable SO_2. In the process it oxidises CO to CO_2. Simultaneously it may be actively producing CO from OCS (Section 2.3.2). However this important chemical pathways still lacks laboratory measured rate constants adding large uncertainty to this and similar models.

In the middle atmosphere, photochemically produced atomic chlorine is highly reactive. In this model the abundances of ClO, $ClCO_x$ and Cl_xSO_2 were not sufficient to be significant reservoirs of CO_x, SO_x or O_x. They can, however, act as important chemical catalysts (Mills and Allen, 2007).

There are two key factors that connect all the chemical groups we have dicussed: the radiation field and oxygen abundance. When any species becomes too abundant it can shield other species from photolyzing radiation. From a modeling perspective this means an overabundance of one phyotochemically active species can impact

chemically unrelated species (see the example of SO_2 and ClO in Section 2.3.4). Given the large temporal variability of SO_2 (Encrenaz, T. et al., 2012), future work should also explore the effects such shielding may have in the Venusian atmosphere.

The oxygen abundance of the middle atmosphere sets the relative abundance for many species. Yet, as noted in Section 2.3.3, models consistently over estimate the O_2 abundance. ClCO(O)O may be an important intermediate species in facilitating CO oxidation to CO_2 in the middle atmosphere (Mills and Allen, 2007). More work is needed to understand the plausibility of these reactions and how such pathways could impact these chemical networks.

As an integration of previous models and observations we think it is useful to summarize the key outstanding questions in Venus atmospheric chemistry. These questions are all demonstrated in earlier sections and have been discussed to varying degrees by previous authors. They are presented in no particular order.

- **SO_2 flux through clouds:** What limits the flux of SO_2 through the cloud deck and why is this process so temporally variable? (Section 2.3.1)
- **OCS destruction at 35 km:** What chemical pathway controls the sudden decline in OCS at ∼35 km altitude? (Section 2.3.2)
- **Surface chemistry:** What are the surface reactions that buffer CO and OCS and on what timescales can those be maintained? (Section 2.3.2)
- **O_2 abundance:** What process is catalyzing photochemically-created O_x back to CO_2? (Section 2.3.3)

Addressing these questions will require both a better understanding of physical processes (i.e. transport and condensation) as well as new laboratory measurements of reaction rates.

In this work we find that, due to chemical interactions, different species exhibit very different responses to k_{zz} (Figures 2.7 and 2.10). While our 1D work suggested that the observed drop in the SO2 mixing ratio cannot be resolved by transport, future 3D GCM studies including more realistic radiative heating and cooling, microphysical cloud processes, gas chemistry, and hydrodynamics could shed more light on the detailed chemical-transport mechanisms in the system and further investigate this problem and the possible solution. The globally averaged k_{zz} from these 3D models should also be complemented by more observational estimates of the k_{zz} either through revisiting the methods of previous studies (von Zahn et al., 1979; Woo and Ishimaru, 1981; Lane and Opstbaum, 1983) or new methods.

In our model, $\sim$40% of the reaction rate coefficients have no lab-measured value and many more rate coefficients are based solely on upper limits or rates at one temperature (Table S1). Given this, it is important to highlight the reactions that have the largest effect in our model and are also lacking any constraints on their reaction rate constants.

The reaction for which lab measurements would have the largest impact on our understanding of lower atmosphere chemistry is SO_3 + OCS $\longrightarrow$ products. As discussed in Section 2.3.2, understanding this reaction is key to understanding if and how the CO and OCS cycles are linked in Venus's atmosphere. A related process is

$CO + SO_3 = CO_2 + SO_2$ which is critical for re-oxidizing CO at the cloud base, but also has no measured rate coefficient.

Another gap in our laboratory measurements is understanding the chemistry and stability of the Cl_xO_x groups. Species such as ClCO(O)O and ClS have been proposed to be important in the recycling of O_x back to CO_2 and thus bringing model O_2 values in line with observations (Section 2.3.3 and Mills and Allen (2007)).

Finally the S_x chemistry plays a large role in several outstanding questions. S_x species have been proposed to be the the sulfur source for the SO_2 inversion layer (Section 2.7 and Zhang et al. (2012)). Our ability to interpret the observed lower atmosphere abundances of S_3, S_4, and OCS is also limited by our understanding of these rates (Section 2.3.2).

Chapter 3

Implications of the Observed Pluto-Charon Density Contrast

This chapter is a slightly modified reprint of work previously published as Bierson, C. J., F. Nimmo, and W. B. McKinnon (2018) "Implications of the observed PlutoCharon density contrast." Icarus 309, 207-219.

Abstract

Observations by the New Horizons spacecraft have determined that Pluto has a larger bulk density than Charon by 153 ± 44 kg m^{-3} (2σ uncertainty). We use a thermal model of Pluto and Charon to determine if this density contrast could be due to porosity variations alone, with Pluto and Charon having the same bulk composition. We find that Charon can preserve a larger porous ice layer than Pluto due to its lower gravity and lower heat flux but that the density contrast can only be explained if the

initial ice porosity is $\gtrsim 30\%$, extends to $\gtrsim 100$ km depth and Pluto retains a subsurface ocean today. We also find that other processes such as a modern ocean on Pluto, self-compression, water-rock interactions, and volatile (e.g., CO) loss cannot, even in combination, explain this difference in density. Although an initially high porosity cannot be completely ruled out, we conclude that it is more probable that Pluto and Charon have different bulk compositions. This difference could arise either from forming Charon via a giant impact, or via preferential loss of H_2O on Pluto due to heating during rapid accretion.

3.1 Introduction

The New Horizons spacecraft has provided a wealth of new information about the Pluto system (Stern et al., 2015) and has spurred a number of modeling efforts to understand these observations. Desch (2015) and Desch and Neveu (2016) have modeled the process of differentiation on early Pluto and Charon (or their precursors in the case of an impact formation). Malamud et al. (2016) modeled the role serpentinization may play in the extensional tectonics observed on Charon (Beyer et al., 2016). Hammond et al. (2016) used thermal modeling to show that if Pluto's subsurface ocean froze completely ice II may have formed, causing contraction. Given that no contractional features are observed on Pluto's surface they infer that Pluto must still have a subsurface ocean today. In this work we apply a thermal model similar to these to examine the implications of the bulk density difference between Pluto and Charon.

Bulk density is one of the most important measurements for determining the first order structure and composition of any world. Prior to 2015, bulk density measurements of Pluto and Charon were limited by the poorly known radius of Pluto (Tholen and Buie, 1997; Lellouch et al., 2009). This uncertainly was large enough that it could barely be determined whether Pluto and Charon had any difference in density at the 2σ level (Brozović et al., 2015). With the images acquired by New Horizons, the radius of Pluto has been measured with an error of less than two kilometers (Stern et al., 2015; Nimmo et al., 2016b). These results show that Pluto and Charon have distinct bulk densities (1854 ± 11 and 1701 ± 33 kg m^{-3} respectively). This difference in density raises the question of whether Pluto and Charon must be compositionally distinct, or if this observation could be consistent with bodies that have the same bulk composition.

This observed difference in density ($\Delta\rho_{PC} = 153 \pm 44$ kg m^{-3}) at first glance appears small given that it is $\sim 10\%$ of Pluto and Charon's bulk density. The changes needed to achieve this density contrast without a difference in bulk composition, however, are dramatic. To give some sense of the scale of change required, it would require melting Pluto's entire ice shell to match the observed density contrast (McKinnon et al., 2017).

Determining if Pluto and Charon have different rock/ice ratios is an important constraint on formation models of the Pluto-Charon system (Nesvorný et al., 2010; Canup, 2005, 2011). There are two primary models for how Pluto and Charon might have formed. One is that Pluto and Charon may have formed in-situ via gravitational collapse (Nesvorný et al., 2010). In this scenario there is no obvious mechanism which

might cause one body to preferentially accrete rock or ice; it therefore predicts that Pluto and Charon should have the same inital bulk composition. Alternatively, Charon could have been formed in a giant impact, analogous to the Earth-Moon forming impact. Published models support a low velocity impact between partially differentiated impactors (Canup, 2011). In this scenario there is a grazing impact where a remnant of the impactor is captured (Charon) and a disk of ice-dominated material is created. Some of this disk reaccretes onto Charon and some of the disk may go on to form the smaller outer moons (Canup, 2011), resulting in a Charon that may be ice-rich relative to Pluto.

In this work, we investigate whether the observed bulk density difference *requires* a difference in composition. We examine a number of sources of density contrast to determine if any of those could explain the magnitude of difference observed. We consider density contrasts due to differences in porosity, subsurface oceans, self-compression, water-rock interactions (i.e. serpentinization), and volatile loss. We focus on porosity as it is the mechanism capable of producing the largest density contrast. We find that to match the observed density contrast Charon must have an ice shell with $\sim 30\%$ porosity to ~ 100 km depth. We also present arguments why this large porous layer is unlikely to exist and instead favor a compositional difference between Pluto and Charon to explain the density contrast.

3.2 Thermal Evolution and Pore Closure Model

To test if the density contrast between Pluto and Charon can be explained by differences in the thickness of a porous layer we used a 1D conductive thermal model based on Nimmo and Spencer (2014). We set the same initial rock to ice ratio for Pluto and Charon and model their thermal evolution in order to determine if the density contrast can be explained without differences in composition. The key effects that generate density contrast are changes in the porous structure and the final state of a subsurface ocean.

To fully test porosity as an explanation for the observed density contrast we focus on the most favorable initial conditions. In our model Pluto and Charon are differentiated; this is consistent with the observation that both Pluto and Charon show no compressional features that would be expected from high-pressure ice phases forming at depth if they were not differentiated (Stern et al., 2015; Moore et al., 2016; McKinnon et al., 2017). The initial porosity extends from the surface to the base of the ice shell and has a constant value ψ_0. Having such a thick initial porous layer after differentiation, even if full differentiation follows a giant impact, may or may not be likely but provides an important end-member case. Although we do not explicitly include impact-generation of porosity at later epochs (Milbury et al., 2015), the depth to which such porosity extends will probably be limited to $\sim$ 10 km at most because of the low velocity and restricted sizes of likely impactors (discussed in Section 3.4.1). Porosity of the silicate core is unlikely to affect the overall bulk density for reasons discussed in

Section 3.3.2 below.

The start time for thermal evolution is assumed to be after the decay of short-lived isotopes like ^{26}Al (Kenyon, 2002). Our model takes into account the decay of the long-lived isotopes ^{238}U, ^{235}U and ^{40}K. The abundances of these elements in the core is assumed to be the chondritic value using the abundances of Robuchon and Nimmo (2011). We adopt a cold (150 K), isothermal initial state and assume that a specified porosity initially extends throughout the entire ice mantle. Differentiation probably requires temperatures higher than 150 K, but higher initial temperatures would permit ice flow and reduce the initial porosity. The initial temperature assumed is not very important for the long-term porosity evolution, because the long-term evolution is determined mainly by the energy associated with radioactive decay (Robuchon and Nimmo, 2011). Sensitivity tests found that lowering the initial temperature from 150 K to 50 K lowered the final density of Charon by $\sim$ 15 kg/m^3 because slightly more porosity was preserved.

We assume both Pluto and Charon have conductive ice mantles (the effect of ice convection is discussed in Section 3.2.1.2). The local melt temperature of each layer is pressure-dependent following Leliwa-Kopystyński et al. (2002). For all the runs presented here we assume there is no ammonia present (discussed in Section 3.2.1). We modify the original code of Nimmo and Spencer (2014) to include the variable thermal conductivity of water ice (Petrenko and Whitworth, 2002; Hobbs, 1974; Hammond et al., 2016), the effect of porosity on thermal conductivity, as well as conservation of mass (A). The model self-consistently adjusts the thermal conductivity (k) for each grid point

(i) as pore closure proceeds. We modify the conductivity according to the lower bound derived by Shoshany et al. (2002),

$$k_i(\phi) = k_{ice}(T)\left(1 - \frac{\phi}{\phi_p}\right)^{(a\phi+b)} \tag{3.1}$$

where ϕ is the layer porosity and T is the temperature in Kelvin. $k_{ice}(T)$ and the constants a, b, and ϕ_p are given in Table 3.1. The effect of porosity on thermal conductivity is generally less than that of the temperature but does become important for high porosity cases ($> 20\%$). The temperature dependence of specific heat (Cp) was not included as sensitivity tests found its effect on the long term evolution negligible (less than 0.1% change in the final density for a factor of four change in Cp).

To account for the radial variation in conductivity, layer thickness (Δz), and density (ρ) of each grid point (subscript i), we update the discretized heat conduction equation from Nimmo and Spencer (2014) to use to that of (Kieffer, 2013) modified to the spherical geometry. The following equation is derived in Appendix A.

$$\Delta T_i = \frac{-2\Delta t}{\rho_i Cp_i \Delta z_i r_i^2}\left[r_{i+1/2}^2 \frac{T_{i+1} - T_i}{\frac{\Delta z_{i+1}}{k_{i+1}} + \frac{\Delta z_i}{k_i}} - r_{i-1/2}^2 \frac{T_i - T_{i-1}}{\frac{\Delta z_{i-1}}{k_{i-1}} + \frac{\Delta z_i}{k_i}}\right]. \tag{3.2}$$

Here Δt is the model timestep and r_i is the radial location of the cell i.

The change in ϕ with time is modeled as depending on the pressure (P) and viscosity (η) (Fowler, 1985; Nimmo et al., 2003; Besserer et al., 2013) via

$$\frac{d\phi}{dt} = -\phi \frac{P(r)}{\eta(T)}. \tag{3.3}$$

Besserer et al. (2013) performed a direct comparison of this model with the more sophisticated model of (Eluszkiewicz, 2004) and qualitative comparisons with (Castillo-Rogez

et al., 2007) and (Eluszkiewicz, 1990). In each case they found a negligible difference. The pressure at each radial layer of index i is calculated as

$$P_i = P_{i+1} + \rho_i g_i \Delta z_i \tag{3.4}$$

where Δz_i and g_i are the layer thickness and the local gravitational acceleration respectively. We assume the surface pressure is $P = 0$. For each layer g_i is computed as

$$g_i = \frac{G}{r_i^2} \sum_{j=0}^{i} m_j \tag{3.5}$$

where G is the universal gravitational constant and m_j is the mass in layer j. The local viscosity is a strong function of the local temperature (T) and is computed via

$$\eta = \eta_0 \exp\left[\frac{Q}{R_g}\left(\frac{1}{T} - \frac{1}{T_0}\right)\right] \tag{3.6}$$

where η_0 is the reference viscosity, T_0 is the reference temperature, Q is the activation energy, and R_g is the gas constant.

As pore space closes and an ocean melts/freezes the density, and therefore the thickness, of each layer can change. Because we are interested in the bulk density evolution it is important to conserve mass as these density changes occur. The change in a given layers thickness can be most easily defined in terms of the ratio of the initial to final density of that layer,

$$\Psi \equiv \frac{\rho_0}{\rho_f}. \tag{3.7}$$

As derived in Appendix A, we can relate Ψ to the change in the radial position of the top of the layer (ΔR) in terms of the initial layer thickness (Δz_0) and the original location

of the layer top ($R_{t,0}$) assuming a fixed bottom boundary.

$$\Delta R_t = \left\{ \left[\left(1 - \frac{\Delta z_0}{R_{t,0}} \right)^3 (1 - \Psi) + \Psi \right]^{1/3} - 1 \right\} R_{t,0} \tag{3.8}$$

After that layer expands or contracts the radial position of all the layers above need to be adjusted accordingly. The spherical geometry causes the change in the radial position of the layer bottom (Δa) to be different from the change of the radial position of the layer top (Δb). For the layer immediately above the layer that has changed density, $\Delta R = \Delta a$. With this constraint, and conservation of volume, we can calculate the change in layer thickness ($\Delta(\Delta z)$) for each layer above the layer that changed density.

$$\Delta b = \left\{ \left[\left(1 + \frac{\Delta a - \Delta z_0}{R_{t,0}} \right)^3 - \left(1 - \frac{\Delta z}{R_{t,0}} \right)^3 \right]^{1/3} - 1 \right\} R_{t,0} \tag{3.9}$$

$$\Delta(\Delta z) = \Delta b - \Delta a \tag{3.10}$$

Because the radial position of each layer, R, is assumed to be at the layer center (not the center of mass), the change in the layer center is given as

$$\Delta R = \frac{\Delta a + \Delta b}{2} \tag{3.11}$$

With the above equations we are able to conserve mass with a relative error over an entire run of $\sim 10^{-5}$. For comparison, runs that keep the layer thickness fixed as the density changes have an error in the mass of $\sim 10^{-2}$.

All of the parameter values used, along with the ranges tested for sensitivity, are listed in Table 3.1. These parameter values are largely based on those of Robuchon and Nimmo (2011). Each model run uses 100 cells in the core and enough cells in the ice

mantle so that the layer thickness is less than 2 km. This spatial scale was determined from a set of resolution tests. The model Δt is recalculated at the start of each timestep using the Courant criterion as

$$\Delta t = 0.3 \min(\Delta z_i^2 \rho_i C p_i / k_i). \tag{3.12}$$

The model is initialized with a constant temperature of 150 K throughout the body and porosity throughout the entire ice shell. Throughout the temperature evolution the surface temperature is fixed at T_s. These initial conditions are set up to be the favorable for porosity surviving in the ice mantle to determine the maximum $\Delta\rho_{PC}$ that can be achieved via a porous ice shell.

3.2.1 Model Results

For each pair of model runs Pluto and Charon are started with their observed mass, a fixed ice to rock ratio, and an initial ice porosity. Because the ice mantle begins porous, the initial radius of Pluto and Charon in most cases exceed their observed values. At the end of each run we can evaluate whether the final radii (and therefore the bulk density) match the observations.

3.2.1.1 Thermal Histories

Before comparing the runs in aggregate it is instructive to look at individual cases. From Equations 3.3 and 3.6 we can see that both higher pressures (due to large g) and higher temperatures on Pluto should lead to less porosity being preserved through time than on Charon. Each run starts with a silicate interior ($\rho_c = 3500$ kg/m^3) and ice

Table 3.1: Parameters used.

	Symbol	Nominal Value	Units	Variation Range
Reference Viscosity	η_0	10^{14}	Pa s	$10^{13} - 10^{17}$
Viscosity Reference Temperature	T_0	270	K	
Activation Energy	Q	60	kJ/mol	
Ice Thermal Conductivity	k_{ice}	0.4685 + 488.12/T	W/(m K)	
Core Thermal Conductivity	k_c	3.0	W/(m K)	$1.0 - 4.0$
Initial Porosity	ϕ_0	0.2		0.0-0.3
Empirical porosity-conductivity coeff.	a	4.1		
Empirical porosity-conductivity coeff.	b	0.22		
Empirical porosity-conductivity coeff.	ϕ_p	0.7		
Surface Temperature	T_s	40.0	K	
Initial Temperature	T_0	150.0	K	150-250
Ice Specific Heat	Cp_{ice}	1930	J/(kg K)	
Core Specific Heat	Cp_c	1053	J/(kg K)	
Ice Density	ρ_{ice}	950	kg/m^3	950
Ocean Density	ρ_w	1000	kg/m^3	
Core Density	ρ_c	3500	kg/m^3	2500-3500
Latent Heat of Ice	L_H	3.33×10^5	J/kg	

mantle ($\rho_i = 950$ kg/m^3). This ice density is slightly higher than pure water ice (~ 920 kg/m^3) to take into account dust and clathrates in the ice shell. The concentration of such impurities is highly uncertain and therefore their potential effects on other parameters such as thermal conductivity are not included in this model. Each of pair of runs starts with a Pluto and Charon that have the same silicate mass fraction (f_{rock}). At the start of each run we introduce an initial porosity, ϕ_0, throughout the ice mantle. This allows us to evaluate the maximum $\Delta\rho_{PC}$ due to differences in the porous structure and the presence of an ocean.

A nominal model output is presented in Figure 3.1. On Pluto, the porosity within ~ 100 km of the core closes on the order of 10^8 years due to the high pressure. Over the first few billion years, the decay of long lived radioisotopes heats the core to > 1000 K. If the thermal conductivity of the core is high enough and the core is sufficiently dense, an ocean will form that can persist to the present day (See Appendix C). A present day ocean on Pluto is consistent with the model of Hammond et al. (2016) (discussed more below) and some observational evidence (Moore et al., 2016; Nimmo et al., 2016a). As this ocean forms and the ice mantle warms, more of the porosity is destroyed by viscous relaxation. The final thickness of the porous layer can vary from 50-170 km. The dominant control on this thickness is the initial porosity, ϕ_0, and the thermal conductivity of the core, k_c. If ϕ_0 is larger, the conductivity of the ice shell is reduced by a larger amount (Equation 3.1) causing more heat to become trapped in the ice shell. This raises temperatures, lowering the ice viscosity and destroying more of the porosity. Similarly if k_c is larger heat is more rapidly transferred from the core

into the ice and more porosity is destroyed.

On Charon, the final porous layer is generally ~ 15 km thicker than on Pluto due to Charon's lower gravity and heat flux. For most of the explored parameter space no ocean ever forms on Charon. In those runs when an ocean does form it never persists to the present day (See Appendix C). Not forming an ocean is seemingly at odds with the widespread extensional features on Charon's surface (Moore et al., 2016), but may be reconciled in number of ways. The first is Charon may have had additional heating from tidal dissipation early in its history (Cheng et al., 2014; Barr and Collins, 2015) which would reduce porosity in Charon's shell. Second, Charon may have an ammonia concentration sufficient to allow a cold ocean to form. Such an ocean would not have a significant effect on the preservation of porosity in the upper ice mantle since there would still be a very low heat flux. Third, the extensional features may not be due to the refreezing of an ancient ocean but due to the serpentinization of Charon's silicate core. This is the scenario proposed by Malamud et al. (2016) and discussed further in Section 3.3.4.

3.2.1.2 Density contrast Results

The results of this parameter space exploration are summarized in Figure 3.2. The largest control on the bulk density is the initial porosity. In particular, to generate the observed $\Delta\rho_{PC}$, an initial porosity of 30% or more is required for almost all parameter combinations. This high porosity needs to extend to significant depths ($\gtrsim 100$ km) but this is easily achieved due to the low temperatures and pressure in Charon's ice shell.

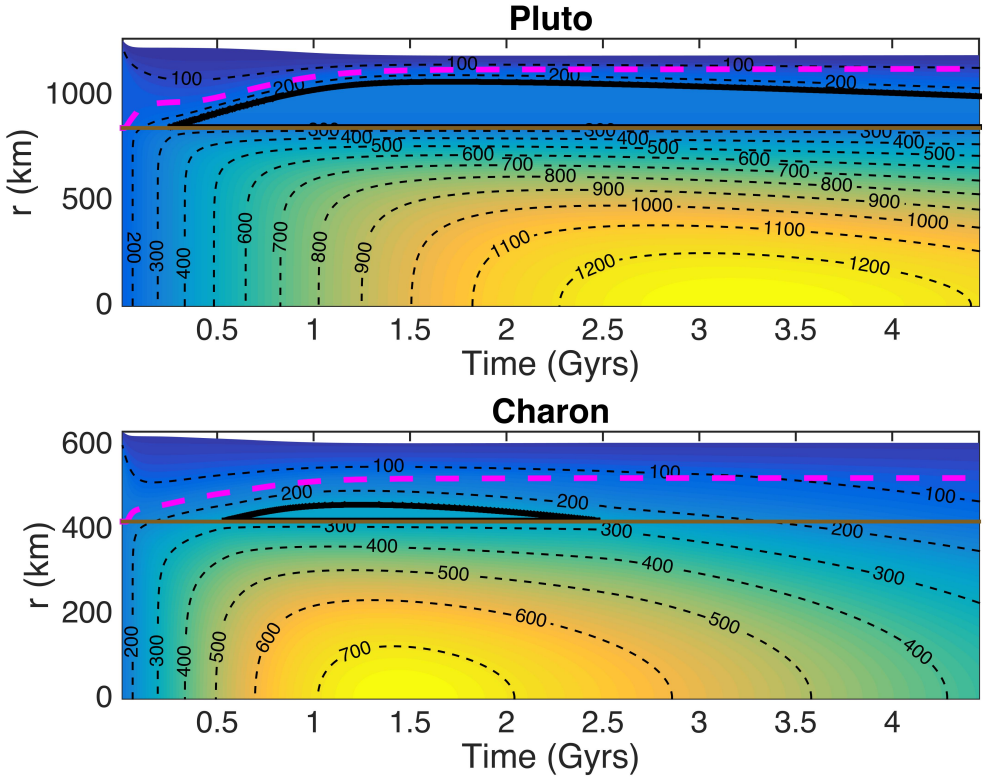

Figure 3.1: Thermal histories of Pluto and Charon. For this run $f_{rock} = 0.69$ $\rho_c = 3500$ kg/m^3, $k_{core} = 3.0$ W/ m K, $\phi_0 = 0.30$. Temperature is contoured at a 100 K interval. The horizontal brown line is the top of the silicate core, the dashed magenta line contours the bottom of the porous layer and the thick black line is the top of the ocean layer. In this run Pluto forms a substantial ocean that persists to the present day. Charon forms an ocean 40 km thick that then refreezes. Charon maintains a larger porous layer than Pluto due to lower temperatures and pressure in the ice mantle. At the end of this run Pluto and Charon have radii of 1191 km and 605.2 km. This run gives $\Delta\rho_{PC} = 132$ kg/m^3, within the 1σ error of the observed density contrast.

Charon could still develop an ocean <50 km thick which then refroze (consistent with the observed extensional tectonics; (Beyer et al., 2016)) without violating this depth requirement. We widely varied the ice viscosity, initial porosity, core conductivity, melting temperature, and core density to characterize the sensitivity of our results (Table 3.1).

Changes in η_0 and k_c have a notable effect on how much porosity is preserved, but have a small effect on $\Delta\rho_{PC}$ because the magnitude of this change is nearly equal on Pluto and Charon. Changing the core density does change f_{rock} but because the effect is the same on Pluto and Charon it does not generate a density contrast.

It is important to investigate how the presence of ammonia would affect our results. If the oceans of Pluto and Charon contain a significant fraction of ammonia they will be colder, larger in extent, and less dense. The colder ocean will limit the heat flux in the ice shell causing porosity to only be destroyed nearer the ocean itself and potentially only when the ice melts. This effect however, will be outweighed by the fact that a larger ocean will form. Of importance for this work, there is no reason to suspect radically different ammonia concentrations on Pluto and Charon and as such this will have a negligible impact on our results. If there is a significant fraction of ammonia in Pluto's modern ocean it would make that ocean less dense, the opposite effect that would be needed to explain $\Delta\rho_{PC}$. These effects together imply that our results (with no ammonia) may represent the best case scenario for generating a density contrast without requiring bulk compositional variation.

Another factor not in our model is convection in the core and/or ice shell. If the cores of Pluto and Charon are porous, hydro-thermal convection could occur for permeability above $\sim 10^{-15}$ m^2 (Turcotte and Schubert, 2014). This would increase the heat flux out of the core. This would have the same effect on the ice shell as varying the thermal conductivity of the core shown in Figure 3.2 (more discussion in Section 3.3.2). Ice shell convection is unlikely to occur on Charon due to its small size. In

contrast, Robuchon and Nimmo (2011) found that for Pluto with $\eta_0 < 5 \times 10^{15}$ Pa s convection occurs. Robuchon and Nimmo (2011) find that when present, the more efficient heat transport due to convection cools the ice shell and prevents an ocean from forming. Conductive and convective shells develop near-surface temperature structures which are almost identical (Robuchon and Nimmo, 2011), because irrespective of how heat is transferred at depth, in the near-surface conduction always dominates. Since it is only in this cold region that porosity can persist, the porosity structure will be almost unaffected by whether conduction or convection operates. In contrast, the lack of a thick ocean for a convective Pluto would lead to a less dense Pluto, making the density contrast harder to explain. Again this implies that our model runs are providing an estimate of the maximum density contrast case.

3.2.1.3 Comparisons to other Thermal models

The only other Charon model to estimate pore closure is described in Malamud and Prialnik (2015) and Malamud et al. (2016). The aim of Malamud and Prialnik (2015) was to explain the difference in density between Charon, Orcus, and Salacia as differences in the porosity of these three Kuiper belt objects. Malamud et al. (2016) used an updated version of the same model to understand the extensional features on Charon found by New Horizons (Stern et al., 2015; Moore et al., 2016). There are two important differences between these models and the one presented here. The first is that these models include serpentinization, and as of Malamud et al. (2016), dehydration reactions between the originally anhydrous silicates and water. This does affect the energy balance

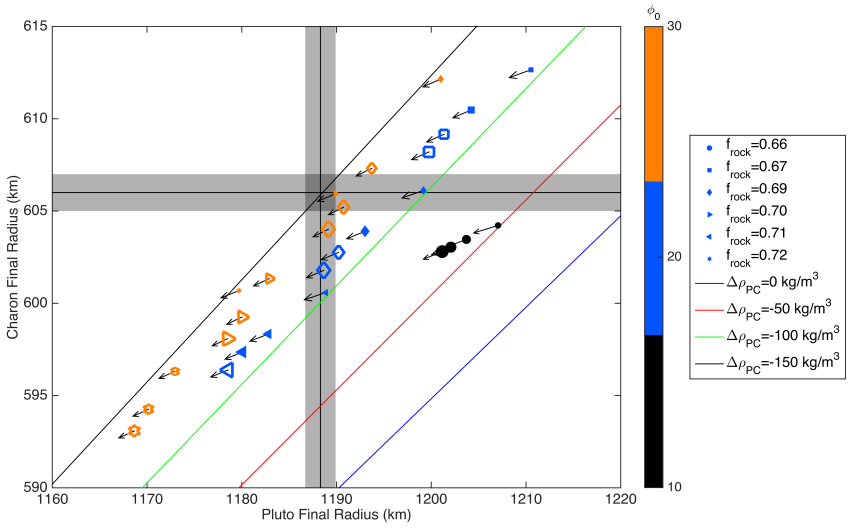

Figure 3.2: Final radius for all model runs with $\rho_c = 3500$ kg/m^3, $\rho_{ice} = 950$ kg/m^3, $\eta_0 = 10^{14}$ Pa s. In all cases the mass of Pluto and Charon is consistent with the observations. Solid lines are lines of constant density contrast. Symbols indicate different rock mass fractions. This size of the points scales with k_c which was varied from 1.0-4.0 W/(m K) in integer increments. Unfilled markers indicate Charon formed an ocean > 10 km thick (C). Arrows show the effect that would result from gravitational self-compression (Section 3.3.1). Note that only porosity has a strong effect $\Delta\rho_{PC}$.

of the system as serpentinization reactions are exothermic. This difference (and others) means that (Malamud et al., 2016) find core temperatures that are ~ 200 K higher than in our model. If this were to be included in our model the increase in heat flux would reduce the amount of porosity that survives on Pluto and Charon to the present day (reducing the density contrast). Given the large uncertainties involved with modeling these reactions (Section 3.3.4) we chose not to include them in our model.

The second important difference is in how porosity is treated. The model of Malamud and Prialnik (2015) and Malamud et al. (2016) use an empirical relationship between pressure, temperature, and porosity based on experimental data from Durham

et al. (2010) and Yasui and Arakawa (2009). We adopt the physical model presented in Section 3.2.1.1. The main difference in these methods is that in the parametrization method of Malamud and Prialnik (2015) and Malamud et al. (2016) ice of the same pressure and temperature will apparently always have the same porosity independent of its history (silicate porosity in their model does have a thermal memory and will not reform porosity). With the method used in this study, once porosity is destroyed it is never reformed. It is not clear what physical process may create new porosity at depth where this difference is likely to manifest. We adopt the simple model described by equation 3 so we can better interpret the effect parameters like k_c and η_0 have on the porosity evolution.

Another model that includes the effects of serpentinization is that of Desch and Neveu (2016). This model also tracks composition, including ammonia along the eutectic as oceans form. This focus of this model was for understanding the evolution of subsurface oceans on Pluto and Charon and their implications for cryovolcanism on these worlds. Given this aim they do not model porosity in the ice shell. Because of the larger number of additional factors tracked in Desch and Neveu (2016) and a limited set of published thermal histories we were not able to make a direct comparison between their model and the one presented here.

The thermal model used here is very similar to Hammond et al. (2016). Hammond et al. (2016) include the formation of ice II which can, in some circumstances, occur on Pluto if the ocean freezes completely. Because of the lack of observed compression features and noted extensional features on Pluto (Moore et al., 2016), they

conclude that Pluto must still have a subsurface ocean and therefore there is no ice II in the ice shell. Given this result we do not include the formation of ice II in our model.

Because of the similarity between our model and Hammond et al. (2016) we tried to benchmark our model against theirs. We found that our model results for the heat flux and ocean thickness through time are very similar to Hammond et al. (2016) for $k_c = 2$ W m^{-1} K^{-1}. However, Hammond et al. (2016) predict Pluto should have a thicker ocean for lower k_c, while we find the opposite effect (See Appendix C). This discrepancy results from a minor error in the code of Hammond et al. (2016); their corrected results now agree with ours (Hammond, pers. comm).

3.3 Other Mechanisms

3.3.1 Self-Compression

One potential mechanism for generating a denser Pluto is the bulk compression of Pluto's interior under the greater lithostatic pressure (P). For environments where the pressure is less than the bulk modulus (K) of the material, as is the case for Pluto and Charon, the change in the material density is given by

$$\frac{d\rho}{\rho} \approx \frac{dP}{K}. \tag{3.13}$$

Due to the low gravity of Pluto and Charon this is a relatively small change in the bulk density. For these calculations we calculate P as shown in Equation 3.4 and nominal values for the bulk modulus of ice ($K_{ice} = 10^{10}$ Pa) and silicates ($K_{rock} = 10^{11}$ Pa). The effect of applying Equation 3.13 as a post-processing step to our model runs is shown

as arrows in Figure 3.2. In general this generates a difference in bulk density between Pluto and Charon of $\Delta\rho \sim 15$ kg/m^3.

3.3.2 Core Porosity

In our model we only include porosity in the ice shell of Pluto and Charon. Porosity likely also exists in their cores but given the warm core temperatures this pore space would likely be filled with liquid water. The question for this study is what effect would changes in the core porosity have for the bulk porosity. When the porosity in the ice mantle closes the ice becomes denser, lowering the bulk volume of the body. Conversely, when the fluid-filled pores in the core close the water is redistributed from the inner parts of the core to the base of the ocean. If that water stays liquid there is no change in the bulk volume, and therefore the bulk density is unaffected. If the water squeezed out of the core then freezes the body radius would increase and thereby lower the bulk density. Because the compressibility of water is much lower than that of rock, as the water migrates upwards it will expand slightly in accordance with Equation 3.13.

Due to the low pressures and low temperatures (Equation 3.3) we find for a silicate viscosity following an Arrhenius dependence (Equation 3.6, $\eta_0 = 10^{20}$ Pa s, $Q = 300$ kJ/mol, $T_0 = 1400$ K) nearly all porosity present in Charon's core could survive the history of the solar system (in the absence of water-rock reactions, considered below). On Pluto there may be significant pore closure. As noted above however, if the water remains liquid (as would be the case if Pluto has a present day ocean (Hammond et al., 2016; Nimmo et al., 2016a; Moore et al., 2016)) Pluto's bulk density would would be

slightly lowered, the opposite effect needed to match the observations. If the water from Pluto's core froze it would also lower Pluto's bulk density. If Charon has a more porous core than Pluto it could also have a lower thermal conductivity unless hydrothermal circulation were operating (Malamud et al., 2016). This also does not help to match the observations because in many model runs nearly all the porosity in Charon's ice shell survives. Our ability to match the observations is limited by the amount of porosity that can be removed from Pluto's ice shell. This porosity reduction would be increased if the core conductivity of Pluto were increased, e.g., by hydrothermal circulation. In the absence of such an effect, porosity in the core of Pluto or Charon, or changes in that porosity, are unlikely to have any effect on their bulk density and may only lower the density of Pluto.

3.3.3 Thermal Expansion

Assuming a cold start, as Pluto and Charon warm they will expand. We can estimate how this will affect the bulk density of each object by combining the density change due to a change in volume (ΔV),

$$\frac{-\Delta\rho}{\rho} = \frac{\Delta V}{V} \tag{3.14}$$

with the volume change due to thermal expansion,

$$\Delta V \approx V \alpha_v \Delta T. \tag{3.15}$$

Here α_v is the volumetric thermal expansion coefficient. Using $\alpha_{v,ice} \approx 10^{-4}$, $\alpha_{v,rock} \approx 3 \times 10^{-5}$ and the temperature changes observed in our modeling ($\Delta T_{ice} \approx 100$ K,

$\Delta T_{rock} \leq 1000$ K) we estimate $\Delta\rho \leq -10$ kg/m^3. Because Pluto will experience higher internal temperatures than Charon, this effect will be larger on Pluto (Pluto will become less dense). This means thermal expansion would produce a small density contrast with the opposite sign to the observed $\Delta\rho_{PC}$.

3.3.4 Serpentinization

If Pluto and Charon have, or have had, active hydrological systems we would expect water-rock interactions to modify their mineralogy and therefore their density structure. The extent to which this would occur on Pluto and Charon depends on a wide range of poorly constrained parameters including the mineralogy and hydrology of their cores. Modeling by Malamud et al. (2016) suggest that this process could be wide-spread at least on Charon.

When anhydrous rock and water react to form serpentine the net result is an increase in density. We can determine how much serpentinization would need to occur to explain the observed density contrast to assess its plausibility. Applying equation 3.14, we can relate ΔV to the change in volume due to producing one mole of serpentinite, ΔV_S by also including the number of moles of serpentinite, N_S.

$$\Delta V = N_S \Delta V_S \tag{3.16}$$

The volume change per mole is calculated by

$$\Delta V_S = \sum_{products} n_i \frac{M_i}{\rho_i} - \sum_{reactants} n_j \frac{M_j}{\rho_j} \tag{3.17}$$

where n_x is the number of moles of the species involved in the reaction, M_x is the molar mass of the species, and ρ_x is the density of the species. Values of ΔV_S calculated for different serpentine reactions are given in Table 3.2. Because all these reactions increase the bulk density, Pluto would have to be more serpentinized than Charon to explain the observed density contrast. Associated magnetite-forming reactions (Vance et al., 2016) also increase the bulk density. We can relate the volume of Pluto that would need to be occupied by serpentinite, V_S to produce $\Delta\rho_{PC}$, using the density of serpentinite (ρ_S) and the molar mass of serpentinite (M_S).

$$N_S = \frac{V_S \rho_S}{M_S} \tag{3.18}$$

$$\frac{-\Delta\rho}{\rho} = \frac{N_S \Delta V_S}{V} \tag{3.19}$$

$$\Rightarrow \frac{V_S}{V} = \frac{-\Delta\rho}{\rho} \frac{M_S}{\Delta V_S \rho_S} \tag{3.20}$$

Depending on the assumed reaction taking place (Table 3.2), Equation 3.19 predicts $\sim 80\%$ of Pluto's total volume would have to be serpentinized to match the observed density contrast. This estimate is a lower limit as it assumes no serpentinization in Charon.

The volume fraction of Pluto and Charon that undergo serpentinization is dependent on the availability of water in the silicate core and the thermal stability of serpentine minerals. Ideally we could choose a temperature cutoff above which serpentinite is unstable and track that isotherm in the model output. The model of Desch and Neveu (2016) has dehydration occur over a range of temperatures between 700-850 K. Malamud and Prialnik (2016) use temperature-dependent reactions rates from ex-

periments by Sawai et al. (2013) and estimate such a cutoff at 675 K. The experimental data is mixed with prograde experiments (constantly increasing temperature with time) finding dehydration temperatures of 875 K to 1075 K (Sawai et al., 2013) while isothermal studies find dehydration temperatures of 725 K to 875 K (Wegner and Ernst, 1983; Candela et al., 2007; Inoue et al., 2009; Dlugogorski and Balucan, 2014). Because of this large uncertainty we opt to not choose any particular temperature for the stability and instead do a more qualitative comparison between Pluto and Charon. Because Charon has lower core temperatures, a much larger volume fraction of Charon's core will be favorable for serpentinite compared to Pluto. This would have the net effect of making Charon more dense than Pluto, the opposite of the observations. It is hard to contrive a situation wherein Pluto would be more serpentinized than Charon.

Given that Charon is likely to be more serpentinized and serpentinization increases the bulk density, we expect serpentinization to have the opposite net effect to that needed to explain the observed density contrast. It is worth noting that there may be secondary chemical reactions may have moderating effects. In summary, while more detailed modeling could be carried out, the simple analysis used here implies that serpentinization is unlikely to explain the density contrast.

3.3.5 Volatile Loss

Spectroscopic data of Pluto's surface suggests it has more high vapor pressure volatile elements including, N_2, CH_4, and CO, than Charon (Buie et al., 1987; Marcialis et al., 1987; Protopapa et al., 2008; Cruikshank et al., 2015). These findings have been

Table 3.2: Volume change per mole serpentinite produced calculated using Equation 3.17. Reaction 1 is that used by Malamud et al. (2016). All reactions result in a overall decrease in volume which would lead to a larger bulk density. Mineral densities used are all at Earth surface temperature and pressure (Table B.1). Star indicates value is uncertain due to the small differences in mineral density and the precision of the density measurements (Ahrens and Gaffney, 1971).

	Reaction	ΔV_S (m^3/mol)
1)	$Mg_2SiO_4 + MgSiO_3 + 2\,H_2O \longrightarrow Mg_3Si_2O_5(OH)_4$	$< 10^{-6}$ *
2)	$3\,Mg_2SiO_4 + SiO_2 + 4\,H_2O \longrightarrow 2Mg_3Si_2O_5(OH)_4$	-8.5×10^{-6}
3)	$2\,Mg_2SiO_4 + 3\,H_2O \longrightarrow Mg_3Si_2O_5(OH)_4 + Mg(OH)_2$	-1.1×10^{-5}

confirmed by New Horizions which found that Charon's surface is almost exclusively water ice with some exposed NH_3 around fresh craters (Grundy et al., 2016). This difference is likely due to Charon's lower gravity allowing these volatiles to be lost to space via escape processes (Schaller and Brown, 2007; Brown, 2012). There are no observations that allow us to determine if Charon has lost its entire inventory of these volatile species or if some are retained in the subsurface.

For this work it is of interest to determine how the loss of these volatile ices would affect Charon's bulk density. To make an initial estimate we assume cometary abundances of these species relative to water (Eberhardt et al., 1988; Crovisier, 1994; Mumma and Charnley, 2011). We focus on CO as it is an order of magnitude more abundant than N_2 and CH_4 and accordingly has the largest impact on the bulk density change. Assuming a CO ice density of 1000 kg/m^3 (Jiang et al., 1975) and present at 10% abundance relative to water ice, the loss of all CO would lead to a increase in the bulk density of Charon by $\sim$ 200 kg/m^3. While we do not know what fraction of Charon's volatile ices have been lost, this effect has the opposite sign of what would be needed to explain the Pluto-Charon density contrast.

3.4 Discussion

The difference in density between Pluto and Charon appears at a first glance to be too small to be of much significance. However, what our analysis shows is that assuming the same bulk composition, this density contrast can only be explained if Charon has a high initial porosity ($\gtrsim 30\%$), that still extends to great depths in Charon's ice shell ($\gtrsim$ 100 km) *and* Charon has not lost a significant fraction of its volatile ices (Section 3.3.5) *and* is not significantly more serpentinized than Pluto (Section 3.3.4).

3.4.1 Initial porosity

Forming and retaining a thick ($\gtrsim$ 100 km) porous layer within Charon is required to explain the observed density contrast. Impacts are known to be able to both create and destroy porosity. Which effect dominates depends on the details of the impact including the preimpact porosity (Arakawa et al., 2002; Milbury et al., 2015). The aggregate long term effect is impacts generate porosity up to some equilibrium value. On the Moon, impact-generated porosity of 15% persists to depths of $\sim$ 15 km (Wieczorek et al., 2013; Besserer et al., 2014); the lower-velocity impacts in the Pluto-Charon system may result in a thinner impact-generated porous layer. Thus, the thick porous layer required to match the density contrast must be the result of primordial (accretionary) processes. This could include one or more giant impacts. Given the geologic evidence that Charon is differentiated (Stern et al., 2015; Moore et al., 2016; McKinnon et al., 2017), this porous layer must also survive (or be formed after) the

differentiation and/or impact formation process.

Unfortunately, there is as yet little understanding of how porosity accumulates during the accretion process. Comets have a porosity of $60\% - 90\%$ (Consolmagno et al., 2008), and Hyperion, with a mean radius of 135 km, has a porosity of $>40\%$ (Thomas et al., 2007). Larger bodies are expected to retain less porosity due to self-compaction. Baer et al. (2011) show that estimated asteroid porosities decrease with increasing size, with estimated porosities of up to 60% at 150 km radius but not exceeding 20% for bodies with radii in excess of 200 km. This holds for both S and C group main belt asteroids, the only two groups for which enough data was available. Ice has a compressional strength an order of magnitude less than that of rock, and ice flows more readily at the same temperature, so icy bodies of a comparable size would be expected to have less porosity[1] Yasui and Arakawa (2009) use experimental measurements to suggest a maximum porosity of 20% for ice at 218 K and 30 MPa (the pressure at 100 km depth on Charon). Taken together, these results suggest that requiring 30% porosity to extend to >100 km on depth is unlikely.

3.4.2 Implications for Other KBOs

If Pluto and Charon have different bulk compositions, that helps constrain how they - and potentially other Kuiper Belt objects - formed. These issues are discussed at length in (McKinnon et al., 2017), but we will briefly mention some key issues here. Although the different compositions of Pluto and Charon could potentially be reconciled

[1]Some asteroids may have undergone compaction due to early ^{26}Al heating. This process is less likely to be relevant in the outer solar system due to much longer formation timescales (Kenyon, 2002).

with direct gravitational collapse (see above), the existence of the small icy satellites of Charon does not support this hypothesis. The Pluto-Charon system more likely formed from a giant impact between partially-differentiated precursors (Canup, 2011); similar giant impacts are also likely responsible for the extreme variation in density observed across other, comparably-sized KBOs (McKinnon et al., 2017, and Chapter 4). Unfortunately, the differentiation state of these bodies is poorly known, but it seems likely that different accretion scenarios will lead to quite different predicted internal structures.

3.5 Conclusion

The difference in Pluto and Charon's density can only be explained by porosity alone in a very extreme case (>30% initial porosity). Arguments presented above suggest that such high initial porosity values are unlikely for such large objects. From this we conclude that Pluto and Charon must have different rock to ice ratios with Pluto having a larger silicate fraction. This observation is consistent with an impact formation model of the Pluto-Charon system or a scenario whereby Pluto formed quickly enough to lose a significant fraction of its original water ice content via accretional heating. Future works should investigate the feasibility of forming Pluto fast enough for this mechanism to occur and the amount of volatiles that may escape during this formation period.

Chapter 4

Using the density of Kuiper Belt Objects to constrain their composition and formation history

This chapter is a slightly modified reprint of work previously published as Bierson, C. J., & Nimmo, F. (2019). "Using the density of Kuiper Belt Objects to constrain their composition and formation history". Icarus, 326, 10-17.

Abstract

Telescopic observations of Kuiper Belt objects have enabled bulk density determinations for 18 objects. These densities vary systematically with size, perhaps suggesting systematic variations in bulk composition. We find this trend can be explained instead by variations in porosity arising from the higher pressures and warmer

temperatures in larger objects. We are able to match the density of 15 of 18 KBOs within their 2σ errors with a constant rock mass fraction of 70%, suggesting a compositionally homogeneous, rock-rich reservoir. Because early ^{26}Al would have removed too much porosity in small ($\sim$ 100 km) KBOs we find the minimum formation time to be 4 Myr after solar system formation. This suggests that coagulation, and not gravitational collapse, was the dominant mechanism for KBO formation, or the gas disk lingered in the outer solar system. We also use this model to make predictions for the density of Makemake, 2007 OR_{10}, and MU_{69}

4.1 Introduction

As of this writing there are 18 Kuiper Belt systems in which the orbit of the secondary has been determined well enough to meaningfully estimate the system mass (Table D.1). In these cases, with the addition of radii measurements from either occultation or direct imaging, the primary's density can be determined. In small KBOs the uncertainty in radius can be large, leading to a large uncertainty in density. Despite this there is a clear systematic trend of larger objects also having a higher density (Brown, 2012).

There are at least three mechanisms that could generate the oberved KBO density distribution. The first is that large KBOs could contain higher density ice phases. However, the low internal pressures in even the largest KBOs (Grundy et al., 2007; Brown, 2012), along with an absence of any evidence for such high-pressure phases in

Pluto (McKinnon et al., 2017), rules out this possibility. The second is there could be a compositional difference between small and large KBOs. This would require smaller KBOs to be significantly more ice rich than their larger counterparts (Brown, 2012). The most commonly discussed mechanism to generate such a difference is large disruptive impacts. Modeling has been done to estimate the effect impacts could have on the bulk density of particular systems (Leinhardt et al., 2010; Canup, 2011; Barr and Schwamb, 2016) but not on the overall density distribution. Estimates using existing scaling laws suggest that impacts are an implausible explanation due to the large fraction of material that would need to be removed from the system (Brown, 2012). A compositional gradient could also arise if larger bodies could lose volatiles preferentially due to accretional heating (McKinnon and Mueller, 1988; Bierson et al., 2018) but we show below that this mechanism is not plausible. The third possibility is that small KBOs contain substantial porosity (Brown, 2012) not present in larger bodies, and is the focus of this work.

Experimental work has shown a series of processes that remove macro-porosity in different temperature-pressure regimes. Below 1 MPa significant macro porosity can be maintained in cold water ice (Durham et al., 2005; Yasui and Arakawa, 2009). Between 1 and 10's of MPa brittle failure begins to cause the porosity to fall rapidly. In this regime pore closure is independent of temperature. The degree of pore closure due to brittle failure is dependent on the rock mass fraction. At pressures greater than 10's of MPa ductile deformation dominates. In this high pressure regime compaction depends on both temperature and rock mass fraction. Durham et al. (2005) found that

pure water ice at temperatures of 77 K could support porosity of 10%-20% beyond 100 MPa. In contrast Yasui and Arakawa (2009) found pure water ice samples at 260 K would contain only ∼1% porosity at 30 MPa.

In this work we test if porosity is able to explain the observed density distribution of KBOs. This is done with a model of KBO thermal evolution coupled with the porosity evolution. We examine the sensitivity of these results to the KBO rock mass fraction and formation time. We find that the observed density distribution can be well fit with a nearly uniform rock mass fraction. We also find that small KBOs ($\sim$ 100 km) must have formed after the decay of ^{26}Al to maintain their high porosity. We discuss the implications of these results for KBO formation.

4.2 Model

We use a 1D model to probe the effect of the two different pore-closure processes on the bulk density. All model runs begin with an undifferentiated KBO that has an initial bulk porosity ϕ_0 and rock mass fraction $f_m = M_s/(M_s + M_i)$. Here M_s is the mass of the silicates and M_i is the mass of the ice. For each model run the effect of brittle failure is calculated followed by the thermal-ductile pore closure modeling.

Brittle failure is assumed to take place on geologically rapid timescales and is modeled following the empirical results of Yasui and Arakawa (2009). This is done by iteratively calculating the internal pressure and updating the ice and silicate porosity

via

$$\phi_i(P) = \max(\phi_0 \exp(b_1 P), \phi_c) \tag{4.1}$$

$$\phi_s(P) = \min(\phi_0 P^{b_2}, \phi_0) \tag{4.2}$$

where P is the local lithostatic pressure in MPa. The value ϕ_c is the assumed porosity that can be supported by matrix in cold conditions (Durham et al., 2005). Values for the empirical constants used are given in Table 4.1. These components are then mixed by their volume fractions to get the bulk porosity of each layer. Recalculation of the pressure profile and updating of the porosity profile is iterated until the porosity profile converges. This sets the initial porosity profile for the long-term thermal modeling.

Modeling the subsequent evolution of the porous structure of KBOs is handled by the thermal evolution model of Bierson et al. (2018). This model assumes that porosity is primordial and removed over time. The final porosity structure is then dependent on the thermal history. Following Besserer et al. (2013) we model the change in porosity as a function of pressure (P) and viscosity (η) via

$$\frac{d\phi}{dt} = \phi \frac{P}{\eta(T)}. \tag{4.3}$$

Here the ice viscosity is taken to be Newtonian and is assumed to vary as

$$\eta(T) = \eta_0 \exp\left(\frac{Q}{R_g T} - \frac{Q}{R_g T_0}\right) \tag{4.4}$$

where Q is the activation energy, R_g is the gas constant and η_0 is the reference viscosity at T_0 (Table 4.1). It was shown by Besserer et al. (2013) that equation (4.3) provides a

reasonable approximation to more complicated pore-closure models (Eluszkiewicz, 1990; Leliwa-Kopystyński and Kossacki, 2000).

This model was updated from Bierson et al. (2018) to include short-lived radioisotopes. The method by which porosity affects thermal conductivity has also been updated. The effect of porosity on thermal conductivity is one of the largest uncertainties in modeling high porosity objects. The true conductivity of a porous mixture depends on the geometry of the matrix (how interconnected the pores are) and the effective thermal conductivity of the pore space itself. While there are no direct constraints on the thermal conductivity of KBOs, there exists a wealth of theoretical work to bound the value. A detailed review of different physical models is given in Carson et al. (2005).

In this work the thermal conductivity is computed for each timestep as follows. We begin by assuming the rock-ice matrix itself is well mixed. As such we use the parallel model to combine an assumed constant silicate conductivity and temperature dependent ice conductivity (see values in Table 4.1).

$$k_0(f_{rock}, T) = k_s \left(f_m \frac{\rho_s}{\rho} \right) + k_{ice} \left(1 - f_m \frac{\rho_s}{\rho} \right) \tag{4.5}$$

We then assume heat transfer through the porosity itself is highly inefficient and apply the parallel model via

$$k(\phi) = k_0(f_{rock}, T)(1 - \phi) \tag{4.6}$$

The parallel model is the upper bound for the thermal conductivity in a solid medium. Any lower values chosen for the thermal conductivity would lead to higher densities

(more porosity removed) for smaller objects. Radiation may slightly enhance the heat transfer in a porous material. Shoshany et al. (2002) calculated the effective thermal conductivity including radiation and the parallel model is in the middle of the range of values they predict. Changing our thermal conductivity model to the maximum conductivity model of Shoshany et al. (2002) results in at most an 8% decrease in predicted density at intermediate (400 km) radii, and less at larger or smaller radii. Neglecting the effect of porosity on thermal conductivity entirely results in at most a 10% change in the final density. This change is too small to alter any of our conclusions.

4.2.1 Parameters and sensitivity

Table 4.1 gives the nominal values for all the parameters used in this modeling. These values are generally taken from Bierson et al. (2018). The new parameters are those for the brittle failure modeling taken from Durham et al. (2005) and Yasui and Arakawa (2009). The other important controlling parameter is the initial porosity. Here a nominal value of 60% is used as this gives an object with $f_m = 70\%$ a density of ~ 750 kg/m^3. This high porosity is consistent with measurements made for asteroids, which Baer et al. (2011) find exhibit a range of porosity from 10%-70% for radii up to ~ 150 km. While porosity is difficult to infer for comets as we do not know the grain density, the bulk density of comets like 67P/Churyumov-Gerasimenko (532 ± 7 kg m^3, Jorda et al. (2016)) imply a porosity of $> 40\%$.

Our model has very little sensitivity to most of the parameters in Table 4.1. A factor of two change in C_p leads to a 4% change in the bulk density (~ 50 kg m^3).

Changing η_0 to 10^{17} Pa s also changes the final density by up to 4%. Changing the initial porosity changes the density of small KBOs (as expected) but does not notably change the radius at which density begins to increase. While each of these parameters may change the rate of change or the timing of when porosity closes, the final bulk density is a robust outcome of our model runs.

Table 4.1: Parameters used. Values for b_1, b_2 based on Yasui and Arakawa (2009). ϕ_c value based on Durham et al. (2005). Other parameter values are from Bierson et al. (2018).

	Symbol	Nominal Value	Units
Ice Reference Viscosity	η_0	10^{14}	Pa s
Viscosity Reference Temperature	T_0	270	K
Activation Energy	Q	60	kJ/mol
Ice Thermal Conductivity	k_{ice}	0.4685 + 488.12/T	W/(m K)
Silicate Thermal Conductivity	k_s	3.0	W/(m K)
Surface Temperature	T_s	40.0	K
Initial Temperature	T_0	100.0	K
Specific Heat	Cp	1000	J/(kg K)
Ice Density	ρ_{ice}	920	kg/m^3
Silicate Density	ρ_s	3500	kg/m^3
Initial Porosity	ϕ_0	0.60	
Strength supported porosity	ϕ_c	0.20	
Empirical compaction parameter (ice)	b_1	-0.1	MPa^{-1}
Empirical compaction parameter (silicate)	b_2	-0.11	

4.2.2 Processes not modeled

The modeling in this work does not include melt production, differentiation, convection, impacts, and tidal heating. Here we discuss each of these process in turn and

their potential impact on our results. Melting to form a subsurface ocean will increase the bulk density while the ocean is present, but the effect is small and will disappear once the ocean freezes (McKinnon et al., 2017; Bierson et al., 2018). Differentiation redistributes the mass within the body; however, because no mass is lost the bulk density is unchanged. As differentiation occurs a small amount of extra gravitational energy will be released which is not included here (Desch et al., 2009; Malamud and Prialnik, 2015). The redistribution of ice and silicates will also change the magnitude of compression but given the low internal pressures of KBOs we expect this to have only a minor effect (Bierson et al., 2018). Since differentiation redistributes the heat source (silicates) towards the center of the body, higher internal temperatures will result, making our porosity estimates conservatively high. Convection will remove heat more rapidly than in our conductive models, but if ice is warm enough to convect, all porosity will already have been removed.

In a high porosity surface, impacts will also reduce the bulk porosity. This effect is limited to the upper tens of kilometers (Milbury et al., 2015), small compared to the size of objects considered here. It is possible that during the formation of larger KBOs, impacts may have removed porosity in a significant fraction of the outer ice shell. Large disruptive impacts into differentiated KBOs could change f_m and are further discussed in section 4.3.

All the KBOs discussed here are either in binary systems or experienced capture (Goldreich et al., 1989; Agnor and Hamilton, 2006). Because of this tidal heating may have been an extra energy source. The amount of energy and its importance to the

overall thermal evolution is dependent on the initial orbital configuration and internal structure of the KBOs (Saxena et al., 2018).

The important point for this work is that all these processes have the same net effect of removing more porosity than predicted by our model. Similarly, we assume an upper limit for the thermal conductivity at a given porosity. A lower thermal conductivity would allow more heat to build up in the interior, removing additional porosity. As a result our model runs represent a *lower bound* on the bulk density (the most porosity that can be retained).

In this work we also assume that the 'ice' component is dominated in composition by H_2O. Depending on their formation conditions, some KBOs may have incorporated ices during formation such as N_2, NH_3, CO, CO_2, and CH_4. Most of these ices have densities close to that of water ice (950, 850, 1000, 1000-1600, 500 kg/m^3 respectively) and so cannot have a significant effect on the bulk density at reasonable concentrations (Satorre et al., 2008, 2013; Umurhan et al., 2017). For example, to change the bulk density by ~ 300 kg/m^3 through the addition methane (the ice with the lowest density) would require adding $\sim 8\%$ of the total body mass. There is also no obvious reason why these compositional differences would depend on size, the main focus of this work.

4.3 Results

A comparison of our model results with the observed KBO values are shown in Figure 4.1a. Our model predicts that the transition from small porous objects to dense

KBOs occurs quickly between a radius of 200km-500km. This transition radius is set by the balance between heat production (which depends on f_m and radioactive half-life) and conductive heat loss (which depends on the body size). An analogous argument has been made for understanding the minimum size of differentiation in asteroids (Grimm and McSween Jr, 1993).

Around this transition diameter internal temperatures begin to reach or exceed the melting point of water (red stars). For the reasons presented in Section 4.2.2 these points are more likely to underestimate the bulk density. The maximum bulk density for a given f_m (neglecting compression) is shown by the dashed lines. This is the density an object of a given f_m would have with no porosity. We estimate the f_m for each KBO in Figure 4.1b with error bars that include the observational uncertainty and in addition treat our model and zero porosity values as limiting cases (see Figure caption for details). This is a conservative estimate that likely overestimates our error particularly for small KBOS and on the lower limits.

For a rock mass fraction of 70% our model matches the density observations for eleven of eighteen KBOs within 1σ and fifteen of seventeen within 2σ (Figure 4.1b). The three objects not well fit by this model are Triton, Eris, and 2002 UX_{25}. Eris and Triton both require $f_m > 70\%$. Triton's high rock fraction might be a consequence of the extreme heating it experienced during capture (Goldreich et al., 1989). There is also a hint that scattered disk objects may have a higher f_m compared with classical KBOs. This could be due to more energetic collisions caused by their more dynamically excited orbits; such collisions will preferentially remove the ice-rich mantles of differentiated

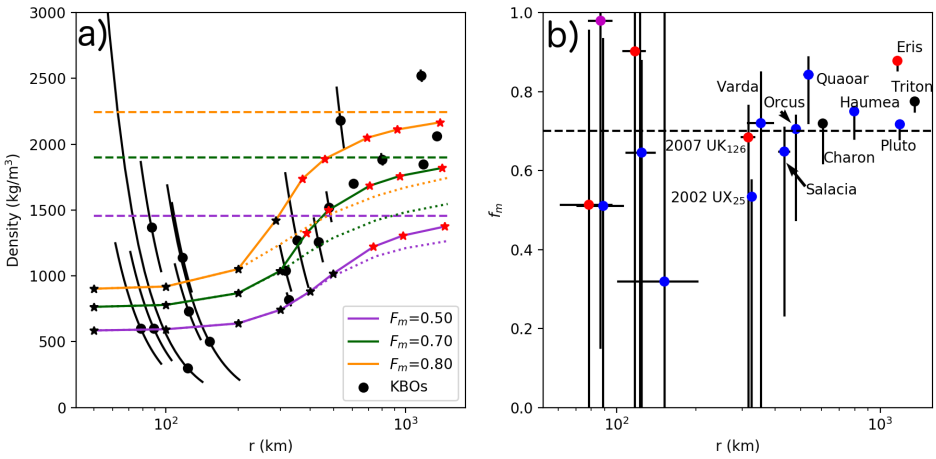

Figure 4.1: a) Density of observed KBOs with 1σ errors in black. Error bars only account for uncertainty in radius. See Table D.1 for citations. Each color refers to a fixed rock mass fraction indicated in the legend. Flat dashed lines show the density of a non-porous object. Dotted line shows the expected density only accounting for brittle failure. Solid lines show model results that include the effects of thermally controlled viscous relaxation. Individual model runs are show with stars. Red stars indicate models where internal temperatures met or exceeded 250 K at some point. All thermal models were started at 10 Myr to avoid the effects of ^{26}Al decay (See Figure 4.2). b) Estimated rock mass fraction of each KBO by interpolating model runs. Horizontal line is $f_m = 0.7$. Colors indicate object class where blue are classical and resonant KBOs, red is scattered disk object, magenta is centaur, and black are satellites. The upper f_m limit is the interpolated model value using the 1σ density upper bound. The lower f_m limit is the f_m calculated assuming no porosity and the 1σ density lower bound.

objects, potentially explaining the higher rock fraction of Eris (Lissauer and Stewart, 1993; Barr and Schwamb, 2016). 2002 UX$_{25}$ is below our expected density. We are not aware of any processes that might significantly lower the bulk density without lowering f_m. Our model predicts that $f_m \sim 50\%$ for 2002 UX$_{25}$. It is worth noting that at present no light curve or occultation measurements have been used to constrain the shape of 2002 UX$_{25}$. If it is significantly non-spherical in shape this could lead to an overestimation of its volume, and thereby an underestimation of the density. Whatever

the case, this object remains enigmatic but is also only a single data point.

We can also place a constraint on the formation time of KBOs as follows. The earlier in solar system history KBOs form the more short lived radiogenic isotopes will be incorporated. It is these isotopes that are responsible for differentiation of small asteroids (Grimm and McSween Jr, 1993); in the case of KBOs, if these objects form too early, sufficient ^{26}Al will be present that all porosity is removed. We assume chondritic abundances of ^{26}Al, ^{60}Fe, ^{53}Mn in the silicate component of modeled KBOs (Table D.2). Figure 4.2 shows the final density of modeled KBOs as a function of their formation time. If a small KBO with $f_m = 0.7$ forms before 5 Myr after CAI the internal porosity will be removed by the heat from the decay of short lived isotopes (primarily ^{26}Al). At $f_m = 0.5$ this limit is pushed to 4 Myr after CAI. As previously noted other feedbacks would further remove porosity once the object starts to warm. Based on these results we conclude that 4 Myr is a lower bound on the KBO formation time. This is consistent with the modeling of Merk and Prialnik (2006) who found that objects larger than a few kilometers radius reach internal temperatures sufficient for liquid water if formed with ^{26}Al still live. A similar argument has been made in favor of a low ^{26}Al in the small Saturnian satellites(Leliwa-Kopystyński and Kossacki, 2000). This is also consistent with McKinnon et al. (2017) who argue that Pluto couldn't be fully differentiated before the Charon-forming impact, and therefore that Pluto did not form while ^{26}Al was live.

An analogous argument can be made that small, low density KBOs cannot have experienced large amounts of tidal heating. As more precise estimates of the

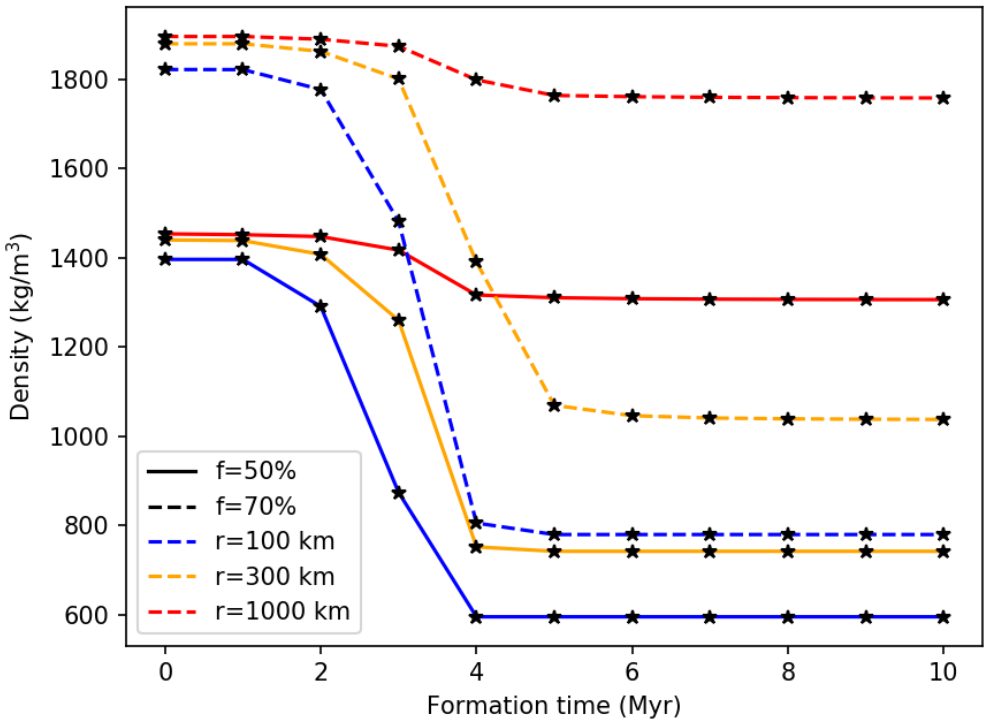

Figure 4.2: Modeled final density of three KBOs of different sizes formed a different times after CAI. Models are shown with f_m=0.70 or 0.50 and with an initial temperature of 40 K. If any small (∼100 km-scale) KBOs formed earlier than 4 Myr after CAI the heat from short lived radioisotopes would remove a significant fraction of their internal porosity.

orbits and individual masses of KBO binary systems become available this should allow constraints to be placed on the tidal parameters such as k_2/Q (Saxena et al., 2018).

4.4 Dicussion

The results above show that small KBOs cannot have formed prior to 4 Ma, as otherwise they would have experienced too much porosity reduction. Placing this

timing constraint on the formation of KBOs allows us to test the formation models that have been proposed. There are currently two main models for KBO formation. The coagulation model proposes that KBOs formed from kilometer-sized precursors that interacted dynamically to form larger bodies (Kenyon, 2002; Kenyon et al., 2008; Schlichting and Sari, 2011). Because of the long orbital periods this process takes tens of millions of years to form the large KBOs. Alternatively the Nesvorný et al. (2010) model proposes that decimeter sized 'pebbles' could be aggregated by the streaming instability to undergo gravitational collapse. This gravitational collapse model naturally forms binary systems which are common in the Kuiper belt and dynamical evidence suggests may have been more common early in the solar system (Petit and Mousis, 2004; Fraser et al., 2017). KBO binaries could form through gravitational interactions (Goldreich et al., 2002) although it remains open if this mechanism is efficient enough to form the inferred number of binary systems.

Because the Nesvorný et al. (2010) model invokes the streaming instability, it requires the presence of a gas disk. Astronomical observations of disks around young systems suggest disk lifetimes of three to ten million years (Haisch et al., 2001; Williams and Cieza, 2011). Constraints from the inner solar system suggest that the gas was present until $4-5$ Myr after solar system formation (Johnson et al., 2016; Wang et al., 2017; Kruijer et al., 2017). Our results constrain KBO formation to be after $4-5$ Myr, around the same time the gas disk is dispersing in the inner solar system.

One interpretation of this result could be that the gas disk must have persisted longer in the outer solar system. How plausible this is depends on what mechanism(s)

are responsible for removing the gas disk in the outer solar system (Matsuyama et al., 2003). This explanation would also require that KBO formation only occur after 4 Myr; if collapse were operating before 4-5 Myr, small dense KBOs should have formed, but are not observed. The alternative interpretation is that our constraint favors KBO formation via the coagulation model. In this case there is no need for special timing because the $\sim$ 100 km KBOs naturally form long after the shortlived isotopes are extinct.

This work also has implications for the dynamical environment of the Kuiper Belt. The near constant f_m is in stark contrast with the inner solar system where core mass fractions vary from 2% (the Moon, Weber et al. 2011) to 70% (Mercury, Rivoldini et al. 2009). This suggests that there was much less erosion of material by impacts relative to the inner solar system. This may be due to the fact that giant impacts between KBOs, such as the one that may have formed the Pluto-Charon system, do not necessarily lead to large changes in the bulk composition (Canup, 2011). A relative absence of giant impacts is also consistent with the preponderance of binary systems being formed by long-range dynamical interactions (Goldreich et al., 2002).

Our results suggest that KBOs form a homogenous population, in terms of their bulk composition. While variations in surface color certainly exist, and appear to be related to dynamical characteristics (Brown, 2012; Dalle Ore et al., 2013; Tegler et al., 2016), we see little evidence of systematic variations in bulk composition, except for a hint that scattered disk objects are more rock-rich (Fig 4.1b).

Going forward we expect future observations to be able to test the model presented here. Moons have recently been discovered for Makemake (Parker et al.,

2016) and 2007 OR_{10} (Kiss et al., 2017) making density measurements likely in the near future. Our results predict that both of these objects should have bulk densities similar to, or slightly less than, that of Pluto ($\approx$ 1800 kg m^{-3}). In contrast, if a mass measurement is possible during the New Horizons flyby of 2014 MU_{69} (r$\sim$ 30 km) we expect it to have a low density of $\sim$ 750 kg/m^3.

4.5 Conclusion

We find the density distribution of KBOs is best explained not by variations in composition, but in bulk porosity. KBOs transition from highly porous to having only a surface porous layer when the internal heat production by radioactive decay outpaces the rate of energy transport by thermal conduction. Because the large amount of energy in ^{26}Al would have melted even small KBOs ($r \sim 100$ km) we conclude they must have formed $\sim$ 5 Myr after CAI. As observations of KBO density are refined and more acquired more narrow constraints will be placed on the range of compositions within the Kuiper Belt.

Chapter 5

Evidence for a hot start and early ocean formation on Pluto

This chapter is a slightly modified reprint of Bierson, C. J., Nimmo, F., and Stern S. A. (2020) "Evidence for a hot start and early ocean formation on Pluto" Nature Geoscience

Abstract

Pluto is thought to possess a present-day ocean beneath a thick ice shell. It has generally been assumed that Pluto accreted from cold material, and then later developed its ocean due to warming from radioactive decay; in this case, the ice shell would have experienced early compression and more recent extension. Here we use geological observations to suggest that Pluto formed "hot", with an early subsurface ocean, rather than "cold". A hot-start Pluto produces an early, rapid phase of extension,

followed by a more prolonged extensional phase which totals ≈0.5% linear strain over the last 3.5 Gyr. The amount of second-phase extension is consistent with that inferred from extensional faults on Pluto; we suggest that the enigmatic "ridge-trough system" recently identified on Pluto is indicative of early extensional tectonics. A hot initial start can be achieved with the gravitational energy released if the final stage of Pluto's accretion is rapid (<30 kyr). A fast final stage of growth is in agreement with models of KBO formation via gravitational collapse followed by pebble accretion, and implies that early oceans were common features of large KBOs.

The New Horizons mission returned the first detailed images of Pluto and Charon (Stern et al., 2015), allowing the first geological interpretations to be made (Moore et al., 2016; White et al., 2017; Stern et al., 2018). An important observation was the predominance of extensional features on both bodies. Because water expands as it freezes, such extension is a natural outcome of a refreezing subsurface ocean, for which there is some circumstantial evidence (e.g. putative cryovolcanism (Moore et al., 2016); reorientation of Sputnik Planitia (Nimmo et al., 2016a)). However, in models in which Pluto starts "cold", the melting of an initially solid ice layer due to radiogenic elements results in early compression, with extension only dominating late in Pluto's history (Robuchon and Nimmo, 2011; Hammond et al., 2016). The most ancient portions of Pluto's surface imaged at high resolution do not show any unambiguous evidence of compression.

5.1 Thermal evolution model

Here we consider the effect of the initial conditions on the long-term thermal and strain evolution of Pluto. We use a relatively simple model in which Pluto is fully differentiated and the ice shell and core are assumed to be conductive throughout; full details of this model are provided in the methods and in Bierson et al. (2018). Some recent works have considered a "hot-start" Pluto (Bhatia and Sahijpal, 2017; Canup et al., 2020; Kimura and Kamata, 2020) but none have considered the tectonic consequences of their results.

The thermal model used in this work is that of Bierson et al. (2018). This model solves the 1D thermal diffusion equation for a sphere assuming a differentiated Pluto. Radioactive elements are assumed to be concentrated in the silicate core in chondritic abundances. As an ocean melts or freezes mass is conserved causing the given layer to shrink or expand with the change in density. All layers above react immediately, equivalent to assuming no stress is stored in the ice shell.

Arguments for a present-day conductive shell have been presented in Nimmo et al. (2016a); at least for the hot start model, our results show that the shell has never been thicker than the present-day value and so if the present-day shell is conductive, it will also have been conductive at all earlier times (Robuchon and Nimmo, 2011). In this study we also neglect complications such as the initial differentiation of Pluto (Desch et al., 2009; Malamud and Prialnik, 2015) and hydrothermal alteration of, or advective heat transfer from, the silicate interior (Neveu et al., 2017), as these are likely to have

only second-order effects on the long-term strain evolution of the shell. We also do not consider the potential role of clathrates at the base of the ice shell (Kamata et al., 2019), since this results in slower shell thickening and smaller strain accumulation. Early tidal heating (Barr and Collins, 2015) might play a role, but the spatial patterns of known tectonic features do not resemble those expected from tides (Keane and Matsuyama, 2016) and so tides are not included in this work.

Many authors have discussed the role ammonia may play in the evolution of Pluto's subsurface ocean (Desch et al., 2009; Hammond et al., 2018) and New Horizons observations have found surface ammonia is correlated with punitive cryovolcanic flows (Dalle Ore et al., 2019). With regards to this work the main impact of ammonia is that depresses the melting point of water. A colder ocean will refreeze more slowly and generate less strain because there is less conductive heat loss, however the general behavior of the ocean will remain the same. Given the large uncertainties in Pluto's ammonia concentration we do not consider this issue in further detail.

Figures 5.1a and 5.1b show two representative evolution models for Pluto, with 5.1a showing a "cold start" and 5.1b a "hot start". In Fig 5.1a the silicate interior of Pluto warms due to radioactive decay, and outward conduction of heat melts the ice. Fig 5.1c shows the cold start model's strain history, with melting leading to a reduction in volume and initial compression. As the radioactive heating wanes, the ice shell begins to refreeze, resulting in extension. However, at the present day the *net* strain is still compressional, because the ocean has not completely refrozen. These results are common to other models with similar initial conditions (Robuchon and Nimmo, 2011;

Hammond et al., 2016).

By contrast, in the hot start model (Fig 5.1b), the ice shell initially thickens rapidly because heat conduction exceeds radioactive heat production. The increase of shell thickness pauses as the radiogenic heat conducted out of the silicates balances the heat lost across the shell; further shell freezing happens more slowly as the radiogenic heat production decreases. The resulting strain evolution (Fig 5.1d) shows corresponding initial rapid extensional strain growth, followed by a pause, then a second episode of increasing extensional strain from 1 Gyr onward. Because the conductive timescale of the silicate core is short relative to the age of the solar system (Nimmo and Spencer, 2014), the final shell thicknesses are not very different between the two model scenarios.

The main difference between the "cold start" (Fig 5.1c) and "hot start" (Fig 5.1d) models is that the early strain is compressional for the former, and extensional for the latter. It is possible that later burial, erosion or tectonic overprinting could remove evidence of early compressional features, or that they could be reactivated as extensional faults. This could allow the cold start to explain the observed recent extension. Nonetheless, the prediction of early compression in the cold-start model is not borne out by the existing observations, to which we now turn.

5.2 Observations and comparison with models

Pluto displays abundant evidence of relatively recent extension, but little of compression (McGovern et al., 2019). In particular, a set of prominent graben west of

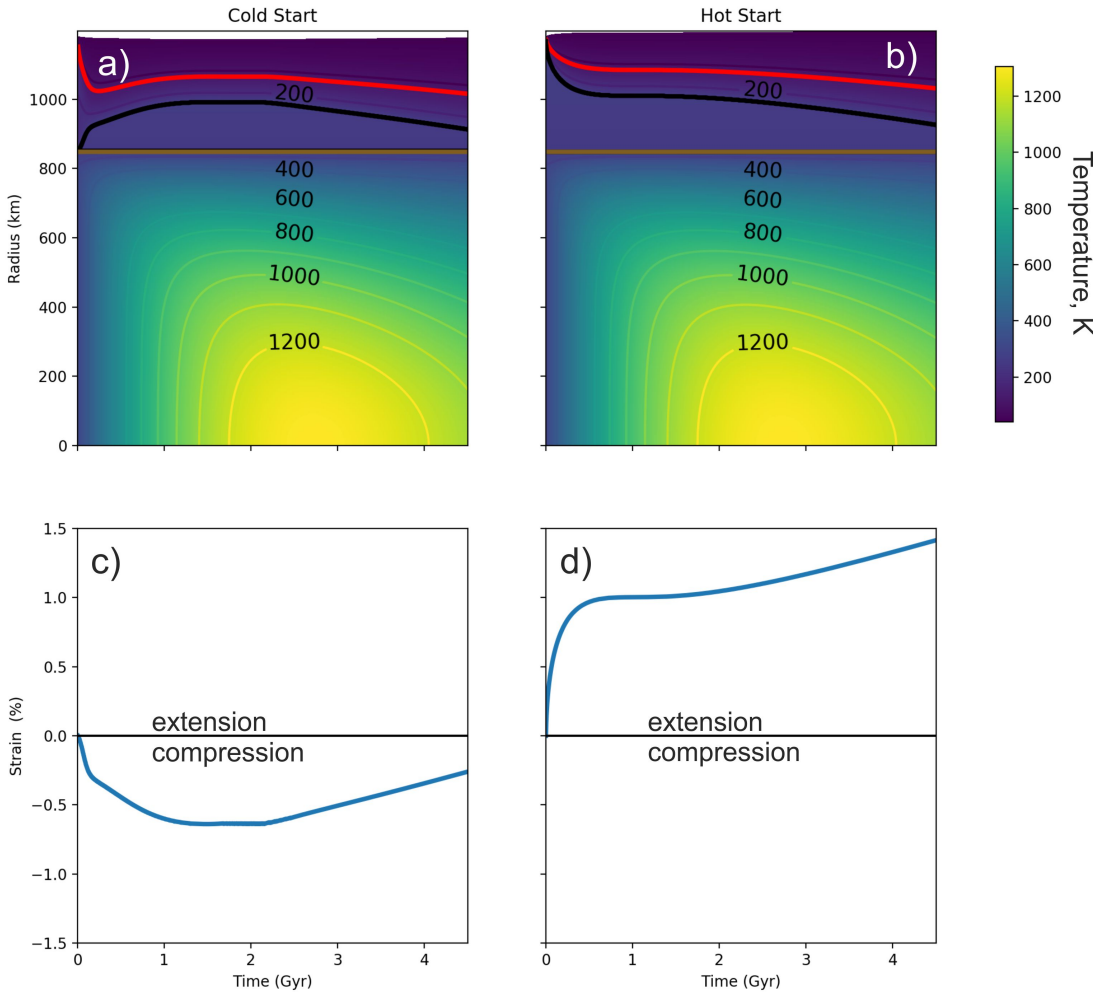

Figure 5.1: a) "Cold start" Pluto model, with initial temperature 300 K in silicates and 200 K in ice. Calculations are carried out as described in Bierson et al. (2018); parameters are the same except for the ice density (920 kg m^{-3}) and core density (3000 kg m^{-3}). Solid brown line indicates top of rocky core and black line top of ocean. Red line indicates the nominal base of the elastic layer, at 120 K (see text). b) "Hot start" Pluto model, with 300 K in silicates plus an ocean and an initial ice shell 6.5 km thick. c) Evolution of net linear strain due to thermal expansion/contraction and freezing/melting of ice, for the "cold start" model. Here compression is negative. d) As for c) but for "hot start".

Sputnik Planitia (Figure 5.2) show little topographic degradation and overprint other features, such as craters (Moore et al., 2016). The graben are also associated with

surface deposits of NH_3, which are likely young because NH_3 degrades over geological time (Cruikshank et al., 2019). Taken together, recent extension is indicated.

In contrast to Charon, where a rough estimate of ∼1% extensional strain was derived (Beyer et al., 2016), no total strain estimates have yet been made for Pluto. We obtain a lower bound by considering the four known, relatively young graben called fossae. Each is about 2 km deep (Conrad et al., 2019), and for typical normal fault dip angles of $45 - 60°$ (Jackson and White, 1989), each experiences about 2.5-4 km of horizontal extension. Across the four fossae the total horizontal extension is thus 10-16 km. For the imaged hemisphere, this represents a linear extensional strain of about 0.3-0.4%. We deliberately focused on the largest fossae seen, but since this estimate does not include the many smaller fractures observed, nor features on poorly-imaged parts of Pluto, it is a conservative minimum.

The most plausible way this recent extension can be reconciled with a cold start is if early compressional features were erased. The putative Charon-forming impact (Canup, 2011) probably completed Pluto's differentiation (McKinnon et al., 2017) and is expected to have erased any pre-existing surface features. Despite uncertainties in the absolute ancient impact flux, the oldest areas of both Pluto and Charon have estimated ages >4 Ga (Singer et al., 2019). On Pluto, evidence of extension in ancient terrains is ambiguous. However, a degraded NNE-SSW trending "ridge-trough system" (RTS) (Schenk et al., 2018) represents a likely ancient tectonic feature (Figure 5.2).

The fact that the RTS does not appear to be significantly deflected by the Sputnik Planitia basin suggests that it predates this impact feature. The extremely

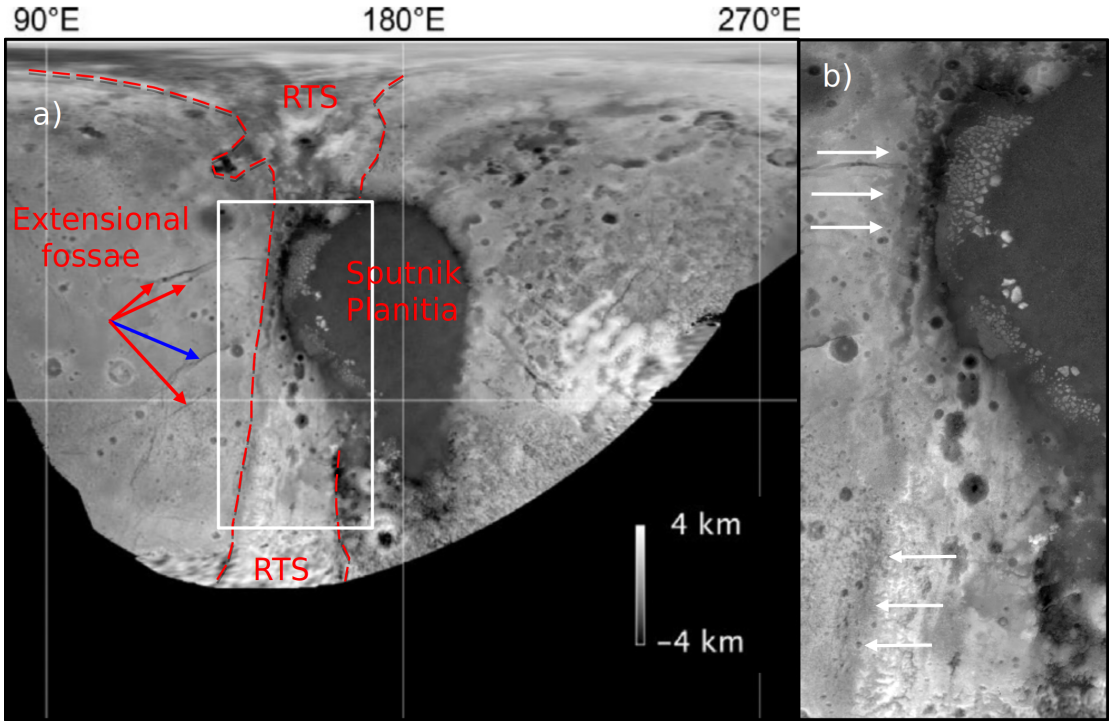

Figure 5.2: Stereo topography from (Schenk et al., 2018) in simple cylindrical projection. The "ridge-trough system" (RTS) is a degraded complex of tectonic features including graben. a) The young extensional fossae west of Sputnik Planitia are described in more detail by (Conrad et al., 2019); the blue arrow points to Virgil Fossa, where cryovolcanism has been suggested (Cruikshank et al., 2019). b) A zoom in of the region boxed in panel a. White arrows point to the 1-2 km deep trough discussed in the text.

degraded nature of the RTS also suggests an ancient origin. Although its morphology is complicated, several areas of the RTS suggest extension. Along its length the western edge of the RTS is a 1-2 km deep depression that is ∼100 km wide (white arrows in Figure 5.2b) (Schenk et al., 2018). If we interpret this feature as an extensional grabben and use the same logic as above these depths of 1-2 km would represent 1.3-4 km extension, or 0.03-0.1% linear strain across the imaged hemisphere. Because of the amount of topographic degradation, this interpretation and strain estimate are both highly uncertain.

Despite the uncertainties, Fig 5.1d (hot-start) is much more consistent with the observations (widespread extensional features and lack of compressional features) than Fig 5.1c (cold-start). The existence of ancient apparent graben in the RTS is not consistent with the ancient compression predicted in Fig 5.1c. Conversely, the post-1 Gyr extension of about 0.5% predicted in Fig 5.1d accords very well with the estimated recent extensional strain of 0.3-0.4%. The magnitude of the predicted early extension (about 1%) is larger than the lower bound derived from the RTS, but as noted above the uncertainties are large, and the degree of model extension depends on the initial conditions assumed. The available observations therefore favor a "hot-start" Pluto, and suggest that significant ancient extension is present that has not yet been identified.

5.3 Heat sources for Pluto

The main sources of energy available to cause an initially hot Pluto are gravitational energy released during accretion, and heat released by ^{26}Al decay. Numerical models of the Charon-forming impact (Canup, 2011) reveal only modest heating of Pluto, but these cover a restricted area of parameter space. The gravitational energy ΔE deposited during accretion of a uniform body is given by

$$\Delta E = M\left(\frac{3}{10}v_{esc}^2 + \frac{1}{2}v_\infty^2\right) \tag{5.1}$$

where M is the final mass, v_{esc} is the final escape velocity ($= \sqrt{2GM/R}$), R is the final radius, G is the gravitational constant and v_∞ is the velocity of the impactors at

infinity. If all this energy is retained as heat, the mean temperature change ΔT is

$$\Delta T = \frac{3}{10}\frac{v_{esc}^2}{C_p}\left(1+\frac{5}{3}f^2\right) = 330 \text{ K } (1+\frac{5}{3}f^2) \tag{5.2}$$

where C_p is the mean specific heat capacity and the factor f compares v_∞ to v_{esc}: $v_\infty = f v_{esc}$. The numerical quantities are obtained by assuming v_{esc}=1.2 km/s and C_p = 1300 J/kg K (Robuchon and Nimmo, 2011). In the late stages of accretion, excitation of planetesimal eccentricities by embryos results in $v_\infty \approx v_{esc}$ ($f \approx 1$) (Agnor et al., 1999, e.g.), while in situations where gas or dynamical friction damps eccentricities, $f \approx 0$. Equation (5.2) shows that if all the energy is retained as heat, Pluto forming an initial liquid water ocean is inescapable.

In practice, however, much of the energy delivered during accretion may be re-radiated instead of being buried (Squyres et al., 1988). The balance between re-radiation and burial depends on the accretion duration of the body, and the impactor size distribution (Barr et al., 2010; Monteux et al., 2014); for instance, on a 30 kyr accretion timescale heat delivered by impactors $\ll$1 km will be promptly re-radiated . If the accreting material is too small, some fraction of the energy may be deposited in an accretion-generated atmosphere. For larger impacts some energy will be lost via radiation from ejecta and impact melt (Stevenson, 1989). Unfortunately such processes are complex and difficult to quantify. Given this uncertainty we proceed by considering limiting cases.

In order to estimate of the maximum accretion duration (τ) consistent with near-surface melting, we can balance black-body radiation from a given surface temper-

ature T_s against the total accretion energy deposited. Making use of equation (1) we obtain

$$\tau = \frac{R\rho v_{esc}^2}{10\sigma T_s^4}\left(1+\frac{5}{3}f^2\right) = 30kyr\left(1+\frac{5}{3}f^2\right) \tag{5.3}$$

where ρ is the bulk density, σ is Stefan's constant, v_{esc} refers to the escape velocity for the final mass and the numerical value was obtained by setting T_s=270 K. While this is only an order-of-magnitude level calculation at best, we can conclude that if Pluto formed with a timescale <30 kyr, then a hot start is assured. On the other hand, accretion taking a few Myr to complete could only result in a hot start if the impactors are large and the heat is deeply buried. Based on these results, we conclude that rapid accretion will almost certainly yield a hot-start Pluto, while the consequences of slower accretion involving large impactors is less certain.

As accretion proceeds, the velocity of impactors will increase (because they are striking a progressively larger body). As a result, accretionally-heated bodies develop a reverse temperature profile, in which the outer layers are hotter than those inside (Squyres et al., 1988; Bhatia and Sahijpal, 2017). This means that a Pluto possessing an ocean in the near-surface (as shown in Fig 1b) is not in contradiction with the requirement that the interior be incompletely differentiated when Charon formed (Canup, 2011). Similar analyses of accretion by (Canup et al., 2020) and (Bhatia and Sahijpal, 2017) also permit an initial near-surface ocean.

In contrast, heating solely by ^{26}Al decay results in an isothermal interior, because the decay timescale is very short compared to the conduction timescale. The degree of heating depends on the accretion time compared to the 0.7 Myr half-life of ^{26}Al.

In Bierson and Nimmo (2019) we argued that the low observed density of small Kuiper Belt Objects (KBOs) requires that they have high porosity. Such porosity would not survive under the influence of ^{26}Al heating. As a result, we conclude that the formation of KBOs took place later than 4 Myr after solar system formation, and thus that ^{26}Al was not an important heat source. Work by Canup et al. (2020) and (Castillo-Rogez et al., 2019) reached an identical conclusion.

5.4 Implications

Traditional coagulation models for KBO formation (Kenyon and Bromley, 2012, e.g.) have difficulty in producing large enough objects (Morbidelli and Nesvorny, 2020). They also typically take hundreds of Myr to produce ∼1000 km-scale bodies, and would therefore likely produce a cold initial Pluto. More recent work, reviewed in Morbidelli and Nesvorny (2020), suggests instead a multi-stage formation process, which also reproduces the observed KBO size-frequency distribution. The initial growth is via the so-called "streaming instability" (Youdin and Goodman, 2005), which generates dense clumps that undergo gravitational collapse to produce 100 km-scale bodies (Nesvorný et al., 2010). An intermediate, slower stage of growth via coagulation may then occur until the bodies become large enough to act as cores for subsequent pebble accretion (Johansen et al., 2015; Ormel, 2017). This final stage of growth, from ∼300 km to Pluto size, is extremely rapid, taking <100 kyr for semi-major axes < 45 AU (Johansen et al., 2015; Johansen and Lambrechts, 2017).

This latter, multi-stage growth model agrees with a hot-start scenario for Pluto. Focusing on the pebble accretion phase, the predicted growth time of <100 kyr is broadly consistent with the rapid growth requirements (Equation 3). Such rapid accretion could in principle have been either early (while ^{26}Al was live) or delayed. Early, rapid formation would assure a hot start, but this scenario contradicts the retention of porosity in small KBOs (see Chapter 3). Delayed, yet rapid accretion is consistent with all these constraints and the general trend observed in meteorite data for the inner solar system (Kruijer et al., 2017).

An important difference between the hot-start and cold-start models is that the former, but not the latter, shows a monotonic increase in ice shell thickness (Fig 5.1). Since both the length-scales of tectonic features (Jackson and White, 1989) and the degree of elastic support of impact craters and other loads (Dombard and McKinnon, 2006) are expected to scale with shell thickness, these two scenarios have different consequences, which may be compared with observations.

One constraint comes from Sputnik Planitia, an ancient impact basin (Singer et al., 2019) now filled with N_2 ice. Although the thickness of the N_2 ice is currently uncertain (Moore et al., 2016), a reasonable guess of a 10 km thick layer requires an elastic thickness of about 40 km (Nimmo et al., 2016a). The base of the elastic layer is defined by a temperature of roughly 120 ± 20 K (Conrad et al., 2019). In the hot start model, such an elastic thickness would be achieved within about 100 Myr of Pluto's formation (Fig 5.1b). This timescale seems reasonable, given the rapidly-declining impactor flux associated with the end of accretion. In the cold-start model, conversely, such a low

elastic thickness is never achieved.

The large-scale nature of the RTS implies a relatively large elastic thickness, which is probably consistent with either model. Although at least one large (D=145 km) relaxed crater, informally named Edgeworth, appears to be present on Pluto (McKinnon et al., 2018) its age is unknown. The observed relaxation, if true, suggests heat fluxes of roughly 50 mW m^{-2} (McKinnon et al., 2018). Such heat fluxes never arise with the "cold start" model and would only occur in the "hot start" model for the first few tens of Myr. Future work to estimate the ice shell elastic thickness during various points in Plutos history could distinguish between the hot-start and cold-start models.

Because the expected heating due to accretion goes as R^2 (equation 5.2), the hot start we envisage is likely relevant only for bodies of roughly half Pluto's radius or more. Charon, at half Pluto's radius, is therefore instructive. The absence of any compressional features on Charon (Beyer et al., 2016) suggests that Charon also underwent a hot start, though in this case the ocean is not expected to have survived to the present day (Desch and Neveu, 2016; Bierson et al., 2018).

Our results imply that initial liquid water oceans were a generic feature of larger dwarf planets in the Kuiper Belt. These oceans will probably have undergone extensive reactions with the warm silicates beneath (Neveu et al., 2017; Malamud and Prialnik, 2015). High initial temperatures might contribute to loss of more volatile species such as N_2 or CO. While Pluto-size bodies are large enough to significantly limit such losses (Schaller and Brown, 2007), smaller bodies have lower escape velocities - but will also have experienced lower peak temperatures. The trade-off between these two

effects deserve further study.

How might the hypothesis of a hot-start Pluto be tested further? An obvious approach would be to estimate the strain history of Pluto, in a similar manner to that attempted for Charon (Beyer et al., 2016), and compare it with the predictions of Fig 5.1. The total strain associated with recent tectonic features can be assessed relatively easily. The nature of the RTS will take more work to characterize, but based on our model we predict that it is primarily an extensional feature, accommodating up to about 1% strain. Our model also makes an implicit prediction for the unimaged hemisphere, and the southern polar terrains globally: they should include additional extensional features, with a total linear strain not exceeding 1.5%.

One important distinction between the cold- and hot-start models is that the former, but not the latter, is likely to retain an undifferentiated, rock-rich carapace in the near-surface (Desch et al., 2009). Such a carapace represents an unstable density structure that might be removed by Rayleigh-Taylor instabilities (Rubin et al., 2014). Thus, clear evidence of a rock-rich carapace, such as that inferred at Ceres (Hiesinger et al., 2016), would rule out a hot-start Pluto. Similarly, widespread evidence of compressional features such as wrinkle ridges would be very hard to reconcile with a hot-start Pluto. Conversely, ancient cryovolcanism and/or extensional tectonics would be hard to explain with the cold-start model, while being entirely consistent with a hot-start. The main pre-requisite for any of these tests is a stratigraphic column for Pluto; now that the basic cratering characteristics have been established (Singer et al., 2019), such an enterprise can be attempted.

An encouraging aspect of a hot-start Pluto is that it is consistent with a multi-stage model of KBO growth (Johansen et al., 2015) which also explains other KBO characteristics (see above). Our hypothesis suggests that large dwarf planets in the Kuiper Belt generally formed "hot", resulting in near-surface oceans and possible loss of volatile species. The long-term interaction between water and warm silicates likely had a large effect on the ocean chemistry (Neveu et al., 2017), and perhaps the habitability of these distant icy worlds.

Chapter 6

Summary

Through this thesis I have presented a variety of works each trying to grow our understanding of the solar system by applying numerical models. The most unique of these, both in terms of topic and character, is Chapter 2 on Venus. This work is not the standard formula of build a model, compare it to data, and present some physical insight. Instead I see it more as an intermediate between a research paper of that form and a review paper. In this work I synthesized several models from different groups and tested them in ways that hadn't been done before. When tested most of these models failed to match the data raising a new question; why? This chapter ends not by presenting new insights into Venus, but instead demonstrating new holes in our understanding. Because no test like this had been done, the community didn't know there was a problem to be solved.

Since Chapter 2 didn't follow the standard formula it was by far the hardest to write. This work as also received a very warm reception at meetings and in the short

time since it has been published. Many groups that don't directly run atmospheric chemistry models but want to use their outputs have jumped on this work. I think this has been assisted by the fact that I openly provided the profiles for every species and reaction rate in every model configuration. I am excited to see how this data is applied.

The next three chapters (3-5) all contribute different pieces to understanding the formation, composition, and evolution of Pluto and its neighbors in the Kuiper belt. Each of these, in slightly different ways, uses recent geophysical observations to constrain the formation of these bodies.

In Chapter 4 I find that that KBOs formed more than 5 Myr after CAIs. This timescale is extremely interesting since it coincides with the expected lifetime of the proto-solar disk itself. This raises the question, was KBO formation triggered in some way by the removal of the proto-solar disk? This may or may not be related to the other question raised, why are KBOs so rocky? Taking the composition of the Sun (which presumably matches the proto-solar nebula) one would expect KBOs to be two-thirds ice, one-third rock. Instead I find the opposite. Both of these are questions that I hope I will have the oppertunity to return to as I continue in my career.

Bibliography

C. B. Agnor and D. P. Hamilton. Neptune's capture of its moon triton in a binary-planet gravitational encounter. *Nature*, 441:192–, May 2006. URL http://dx.doi.org/10.1038/nature04792.

C. B. Agnor, R. M. Canup, and H. F. Levison. On the character and consequences of large impacts in the late stage of terrestrial planet formation. *Icarus*, 142(1):219 – 237, 1999. ISSN 0019-1035. doi: https://doi.org/10.1006/icar.1999.6201. URL http://www.sciencedirect.com/science/article/pii/S0019103599962012.

T. J. Ahrens and E. S. Gaffney. Dynamic compression of enstatite. *Journal of Geophysical Research*, 76(23):5504–5513, 1971. ISSN 2156-2202. doi: 10.1029/JB076i023p05504. URL http://dx.doi.org/10.1029/JB076i023p05504.

M. Arakawa, J. Leliwa-Kopystynski, and N. Maeno. Impact experiments on porous icy-silicate cylindrical blocks and the implication for disruption and accumulation of small icy bodies. *Icarus*, 158(2):516 – 531, 2002. ISSN 0019-1035. doi: http://dx.doi.org/10.1006/icar.2002.6893. URL http://www.sciencedirect.com/science/article/pii/S0019103502968934.

G. Arney, V. Meadows, D. Crisp, S. J. Schmidt, J. Bailey, and T. Robinson. Spatially resolved measurements of h2o, hcl, co, ocs, so2, cloud opacity, and acid concentration in the venus near-infrared spectral windows. *Journal of Geophysical Research: Planets*, 119(8):1860–1891, 2014. ISSN 2169-9100. doi: 10.1002/2014JE004662. URL http://dx.doi.org/10.1002/2014JE004662. 2014JE004662, No SOM.

J. Baer, S. R. Chesley, and R. D. Matson. Astrometric masses of 26 asteroids and observations on asteroid porosity. *The Astronomical Journal*, 141(5):143, 2011. URL http://stacks.iop.org/1538-3881/141/i=5/a=143.

A. C. Barr and G. C. Collins. Tectonic activity on pluto after the charon-forming impact. *Icarus*, 246:146 – 155, 2015. ISSN 0019-1035. doi: http://dx.doi.org/10.1016/j.icarus.2014.03.042. URL http://www.sciencedirect.com/science/article/pii/S0019103514001687. Special Issue: The Pluto System.

A. C. Barr and M. E. Schwamb. Interpreting the densities of the kuiper belt's dwarf planets. *Monthly Notices of the Royal Astronomical Society*, 460(2):1542–1548, 2016. doi: 10.1093/mnras/stw1052. URL http://dx.doi.org/10.1093/mnras/stw1052.

A. C. Barr, R. I. Citron, and R. M. Canup. Origin of a partially differentiated Titan. *Icarus*, 209(2):858–862, Oct 2010. doi: 10.1016/j.icarus.2010.05.028.

J. Barstow, C. Tsang, C. Wilson, P. Irwin, F. Taylor, K. McGouldrick, P. Drossart, G. Piccioni, and S. Tellmann. Models of the global cloud structure on venus derived from venus express observations. *Icarus*, 217(2):542 – 560, 2012. ISSN 0019-1035. doi:

http://dx.doi.org/10.1016/j.icarus.2011.05.018. URL http://www.sciencedirect.com/science/article/pii/S0019103511001916. Advances in Venus Science.

D. Belyaev, O. Korablev, A. Fedorova, J.-L. Bertaux, A.-C. Vandaele, F. Montmessin, A. Mahieux, V. Wilquet, and R. Drummond. First observations of so2 above venus' clouds by means of solar occultation in the infrared. *Journal of Geophysical Research: Planets*, 113(E5):n/a–n/a, 2008. ISSN 2156-2202. doi: 10.1029/2008JE003143. URL http://dx.doi.org/10.1029/2008JE003143. E00B25.

D. A. Belyaev, F. Montmessin, J.-L. Bertaux, A. Mahieux, A. A. Fedorova, O. I. Korablev, E. Marcq, Y. L. Yung, and X. Zhang. Vertical profiling of so2 and so above venus' clouds by spicav/soir solar occultations. *Icarus*, 217(2):740 – 751, 2012. ISSN 0019-1035. doi: http://dx.doi.org/10.1016/j.icarus.2011.09.025. URL http://www.sciencedirect.com/science/article/pii/S0019103511003770. Advances in Venus Science.

J.-L. Bertaux, A.-C. Vandaele, O. Korablev, E. Villard, A. Fedorova, D. Fussen, E. Quémerais, D. Belyaev, A. Mahieux, F. Montmessin, et al. A warm layer in venus' cryosphere and high-altitude measurements of hf, hcl, h2o and hdo. *Nature*, 450(7170):646–649, 2007.

J. Besserer, F. Nimmo, J. H. Roberts, and R. T. Pappalardo. Convection-driven compaction as a possible origin of enceladus's long wavelength topography. *Journal of Geophysical Research: Planets*, 118(5):908–915, 2013. ISSN 2169-9100. doi:

10.1002/jgre.20079. URL http://dx.doi.org/10.1002/jgre.20079. Note that there is an error in equation 2b.

J. Besserer, F. Nimmo, M. A. Wieczorek, R. C. Weber, W. S. Kiefer, P. J. McGovern, J. C. Andrews-Hanna, D. E. Smith, and M. T. Zuber. GRAIL gravity constraints on the vertical and lateral density structure of the lunar crust. *Geophysical Research Letters*, 41(16):5771–5777, 2014. ISSN 1944-8007. doi: 10.1002/2014GL060240.

R. A. Beyer, F. Nimmo, W. B. McKinnon, J. M. Moore, R. P. Binzel, J. W. Conrad, A. Cheng, K. Ennico, T. R. Lauer, C. Olkin, S. Robbins, P. Schenk, K. Singer, J. R. Spencer, S. A. Stern, H. Weaver, L. Young, and A. M. Zangari. Charon tectonics. *Icarus*, pages –, 2016. ISSN 0019-1035. doi: http://dx.doi.org/10.1016/j.icarus.2016.12.018. URL http://www.sciencedirect.com/science/article/pii/S001910351630834X.

G. K. Bhatia and S. Sahijpal. Thermal evolution of trans-Neptunian objects, icy satellites, and minor icy planets in the early solar system. *Meteoritics and Planetary Science*, 52(12):2470–2490, Dec 2017. doi: 10.1111/maps.12952.

C. Bierson and F. Nimmo. Using the density of kuiper belt objects to constrain their composition and formation history. *Icarus*, 326:10 – 17, 2019. ISSN 0019-1035. doi: https://doi.org/10.1016/j.icarus.2019.01.027. URL http://www.sciencedirect.com/science/article/pii/S0019103518306456.

C. Bierson, F. Nimmo, and W. McKinnon. Implications of the observed pluto-

charon density contrast. *Icarus*, 309:207 – 219, 2018. ISSN 0019-1035. doi: https://doi.org/10.1016/j.icarus.2018.03.007. URL https://www.sciencedirect.com/science/article/pii/S0019103517303081.

J. E. BLAMONT, R. E. YOUNG, A. SEIFF, B. RAGENT, R. SAGDEEV, V. M. LINKIN, V. V. KERZHANOVICH, A. P. INGERSOLL, D. CRISP, L. S. ELSON, R. A. PRESTON, G. S. GOLITSYN, and V. N. IVANOV. Implications of the vega balloon results for venus atmospheric dynamics. *Science*, 231(4744):1422–1425, 1986. ISSN 0036-8075. doi: 10.1126/science.231.4744.1422. URL https://science.sciencemag.org/content/231/4744/1422.

M. E. Brown. The compositions of kuiper belt objects. *Annual Review of Earth and Planetary Sciences*, 40(1):467–494, 2012. doi: 10.1146/annurev-earth-042711-105352. URL http://dx.doi.org/10.1146/annurev-earth-042711-105352.

M. E. Brown. The density of mid-sized kuiper belt object 2002 ux25 and the formation of the dwarf planets. *The Astrophysical Journal Letters*, 778(2):L34, 2013. URL http://stacks.iop.org/2041-8205/778/i=2/a=L34.

M. E. Brown and B. J. Butler. The density of mid-sized kuiper belt objects from alma thermal observations. *The Astronomical Journal*, 154(1):19, 2017. URL http://stacks.iop.org/1538-3881/154/i=1/a=19.

M. Brozović, M. R. Showalter, R. A. Jacobson, and M. W. Buie. The orbits and masses of satellites of pluto. *Icarus*, 246:317 – 329, 2015. ISSN 0019-1035. doi:

http://dx.doi.org/10.1016/j.icarus.2014.03.015. URL http://www.sciencedirect.com/science/article/pii/S0019103514001419. Special Issue: The Pluto System.

M. W. Buie, D. P. Cruikshank, L. A. Lebofsky, and E. F. Tedesco. Water frost on charon. *Nature*, 329(6139):522–523, Oct. 1987. URL http://dx.doi.org/10.1038/329522a0.

J. Burkholder, S. Sander, J. Abbatt, J. Barker, R. Huie, C. Kolb, M. Kurylo, V. Orkin, D. Wilmouth, and P. Wine. Chemical kinetics and photochemical data for use in atmospheric studies: evaluation number 18. Technical report, Pasadena, CA: Jet Propulsion Laboratory, National Aeronautics and Space Administration, 2015.

P. Candela, C. Crummett, D. Earnest, M. Frank, and A. Wylie. Low-pressure decomposition of chrysotile as a function of time and temperature. *American Mineralogist*, 92(10):1704–1713, 2007. ISSN 0003-004X. doi: 10.2138/am.2007.2559. URL http://ammin.geoscienceworld.org/content/92/10/1704.

R. M. Canup. A giant impact origin of pluto-charon. *Science*, 307(5709):546–550, 2005. doi: 10.1126/science.1106818. URL http://www.sciencemag.org/content/307/5709/546.abstract.

R. M. Canup. On a giant impact origin of charon, nix, and hydra. *The Astronomical Journal*, 141(2):35, 2011. URL http://stacks.iop.org/1538-3881/141/i=2/a=35.

R. M. Canup, K. M. Kratter, and M. Neveu. *On the Origin of the Pluto System*. 2020.

J. K. Carson, S. J. Lovatt, D. J. Tanner, and A. C. Cleland. Thermal conductivity bounds for isotropic, porous materials. *International Journal of Heat and Mass Transfer*, 48(11):2150 – 2158, 2005. ISSN 0017-9310. doi: https://doi.org/10.1016/j.ijheatmasstransfer.2004.12.032. URL http://www.sciencedirect.com/science/article/pii/S0017931005000670.

J. Castillo-Rogez, D. Matson, C. Sotin, T. Johnson, J. Lunine, and P. Thomas. Iapetus' geophysics: Rotation rate, shape, and equatorial ridge. *Icarus*, 190(1):179 – 202, 2007. ISSN 0019-1035. doi: http://dx.doi.org/10.1016/j.icarus.2007.02.018. URL http://www.sciencedirect.com/science/article/pii/S0019103507001108.

J. Castillo-Rogez, T. V. Johnson, M. H. Lee, N. J. Turner, D. L. Matson, and J. Lunine. 26al decay: Heat production and a revised age for iapetus. *Icarus*, 204(2):658 – 662, 2009. ISSN 0019-1035. doi: http://dx.doi.org/10.1016/j.icarus.2009.07.025. URL //www.sciencedirect.com/science/article/pii/S0019103509003248.

J. Castillo-Rogez, P. Vernazza, and K. Walsh. Geophysical evidence that Saturn's Moon Phoebe originated from a C-type asteroid reservoir. *Monthly Notices of the Royal Astronomical Society*, 486(1):538–543, 03 2019. ISSN 0035-8711. doi: 10.1093/mnras/stz786. URL https://doi.org/10.1093/mnras/stz786.

W. Cheng, M. H. Lee, and S. Peale. Complete tidal evolution of pluto-charon. *Icarus*, 233:242 – 258, 2014. ISSN 0019-1035. doi: http://dx.doi.org/10.1016/j.icarus.2014.01.046. URL http://www.sciencedirect.com/science/article/pii/S0019103514000773.

J. W. Conrad, F. Nimmo, P. M. Schenk, W. B. McKinnon, J. M. Moore, C. B. Beddingfield, R. A. Beyer, K. D. Runyon, L. A. Young, S. A. Stern, H. A. Weaver, C. B. Olkin, K. Ennico, and New Horizons GGI Team. An upper bound on Pluto's heat flux from a lack of flexural response of its normal faults. *Icarus*, 328:210–217, Aug. 2019. doi: 10.1016/j.icarus.2019.03.028.

G. Consolmagno, D. Britt, and R. Macke. The significance of meteorite density and porosity. *Chemie der Erde - Geochemistry*, 68(1):1 – 29, 2008. ISSN 0009-2819. doi: http://dx.doi.org/10.1016/j.chemer.2008.01.003. URL `http://www.sciencedirect.com/science/article/pii/S0009281908000044`.

D. V. Cotton, J. Bailey, D. Crisp, and V. Meadows. The distribution of carbon monoxide in the lower atmosphere of venus. *Icarus*, 217(2):570 – 584, 2012. ISSN 0019-1035. doi: http://dx.doi.org/10.1016/j.icarus.2011.05.020. URL `http://www.sciencedirect.com/science/article/pii/S001910351100193X`. Advances in Venus Science.

J. Crovisier. Molecular abundances in comets. *Symposium - International Astronomical Union*, 160:313?326, 1994. doi: 10.1017/S0074180900046611.

D. Cruikshank, W. Grundy, F. DeMeo, M. Buie, R. Binzel, D. Jennings, C. Olkin, J. Parker, D. Reuter, J. Spencer, S. Stern, L. Young, and H. Weaver. The surface compositions of pluto and charon. *Icarus*, 246:82 – 92, 2015. ISSN 0019-1035. doi: http://dx.doi.org/10.1016/j.icarus.2014.05.023. URL `http://www.sciencedirect.com/science/article/pii/S0019103514002760`. Special Issue: The Pluto System.

D. P. Cruikshank, O. M. Umurhan, R. A. Beyer, and et al. Recent cryovolcanism in Virgil Fossae on Pluto. *Icarus*, 330:155–168, Sep 2019. doi: 10.1016/j.icarus.2019.04.023.

C. M. Dalle Ore, L. V. Dalle Ore, T. L. Roush, D. P. Cruikshank, J. P. Emery, N. Pinilla-Alonso, and G. A. Marzo. A compositional interpretation of trans-neptunian objects taxonomies. *Icarus*, 222(1):307 – 322, 2013. ISSN 0019-1035. doi: https://doi.org/10.1016/j.icarus.2012.11.015. URL `http://www.sciencedirect.com/science/article/pii/S0019103512004617`.

C. M. Dalle Ore, D. P. Cruikshank, S. Protopapa, F. Scipioni, W. B. McKinnon, J. C. Cook, W. M. Grundy, B. Schmitt, S. A. Stern, J. M. Moore, A. Verbiscer, A. H. Parker, K. N. Singer, O. M. Umurhan, H. A. Weaver, C. B. Olkin, L. A. Young, and K. Ennico. Detection of ammonia on pluto's surface in a region of geologically recent tectonism. *Science Advances*, 5(5), 2019. doi: 10.1126/sciadv.aav5731. URL `https://advances.sciencemag.org/content/5/5/eaav5731`.

S. Desch and M. Neveu. Differentiation and cryovolcanism on charon: A view before and after new horizons. *Icarus*, pages –, 2016. ISSN 0019-1035. doi: http://dx.doi.org/10.1016/j.icarus.2016.11.037. URL `http://www.sciencedirect.com/science/article/pii/S0019103516307904`.

S. J. Desch. Density of charon formed from a disk generated by the impact of partially differentiated bodies. *Icarus*, 246:37 – 47, 2015. ISSN 0019-1035. doi: http://dx.doi.

org/10.1016/j.icarus.2014.07.034. URL http://www.sciencedirect.com/science/article/pii/S0019103514004989. Special Issue: The Pluto System.

S. J. Desch, J. C. Cook, T. Doggett, and S. B. Porter. Thermal evolution of kuiper belt objects, with implications for cryovolcanism. *Icarus*, 202(2):694 – 714, 2009. ISSN 0019-1035. doi: http://dx.doi.org/10.1016/j.icarus.2009.03.009. URL http://www.sciencedirect.com/science/article/pii/S0019103509001146.

B. Z. Dlugogorski and R. D. Balucan. Dehydroxylation of serpentine minerals: Implications for mineral carbonation. *Renewable and Sustainable Energy Reviews*, 31: 353 – 367, 2014. ISSN 1364-0321. doi: 10.1016/j.rser.2013.11.002. URL http://www.sciencedirect.com/science/article/pii/S136403211300751X.

A. J. Dombard and W. B. McKinnon. Elastoviscoplastic relaxation of impact crater topography with application to Ganymede and Callisto. *Journal of Geophysical Research (Planets)*, 111:E01001, Jan. 2006. doi: 10.1029/2005JE002445.

W. Durham, O. Prieto-Ballesteros, D. Goldsby, and J. Kargel. Rheological and thermal properties of icy materials. *Space science reviews*, 153(1-4):273–298, 2010.

W. B. Durham, W. B. McKinnon, and L. A. Stern. Cold compaction of water ice. *Geophysical Research Letters*, 32(18), 2005. ISSN 1944-8007. doi: 10.1029/2005GL023484. URL http://dx.doi.org/10.1029/2005GL023484. L18202.

P. Eberhardt, D. Krankowsky, W. Schulte, U. Dolder, P. Lämmerzahl, J. J. Berthelier, J. Woweries, U. Stubbemann, R. R. Hodges, J. H. Hoffman, and J. M. Illiano. *The*

CO and N2 abundance in comet P/Halley, pages 481–484. Springer Berlin Heidelberg, Berlin, Heidelberg, 1988. ISBN 978-3-642-82971-0. doi: 10.1007/978-3-642-82971-0_87. URL http://dx.doi.org/10.1007/978-3-642-82971-0_87.

J. Eluszkiewicz. Compaction and internal structure of mimas. *Icarus*, 84(1):215 – 225, 1990. ISSN 0019-1035. doi: http://dx.doi.org/10.1016/0019-1035(90)90167-8. URL http://www.sciencedirect.com/science/article/pii/0019103590901678.

J. Eluszkiewicz. Dim prospects for radar detection of europa's ocean. *Icarus*, 170(1):234 – 236, 2004. ISSN 0019-1035. doi: http://dx.doi.org/10.1016/j.icarus.2004.02.011. URL http://www.sciencedirect.com/science/article/pii/S0019103504000788.

Encrenaz, T., Greathouse, T. K., Roe, H., Richter, M., Lacy, J., Bézard, B., Fouchet, T., and Widemann, T. Hdo and so2 thermal mapping on venus: evidence for strong so2 variability. *Astronomy & Astrophysics*, 543:A153, 2012. doi: 10.1051/0004-6361/201219419. URL http://dx.doi.org/10.1051/0004-6361/201219419.

L. W. Esposito. Ultraviolet contrasts and the absorbers near the venus cloud tops. *Journal of Geophysical Research: Space Physics*, 85(A13):8151–8157, 12 1980. ISSN 2156-2202. doi: 10.1029/JA085iA13p08151. URL https://doi.org/10.1029/JA085iA13p08151.

J. Fegley, B., G. Klingelhöfer, K. Lodders, and T. Widemann. Geochemistry of Surface-Atmosphere Interactions on Venus. In S. W. Bougher, D. M. Hunten, and R. J.

Phillips, editors, *Venus II: Geology, Geophysics, Atmosphere, and Solar Wind Environment*, page 591, Jan 1997.

Fornasier, S., Lellouch, E., Müller, T., Santos-Sanz, P., Panuzzo, P., Kiss, C., Lim, T., Mommert, M., Bockelée-Morvan, D., Vilenius, E., Stansberry, J., Tozzi, G. P., Mottola, S., Delsanti, A., Crovisier, J., Duffard, R., Henry, F., Lacerda, P., Barucci, A., and Gicquel, A. Tnos are cool: A survey of the trans-neptunian region - viii. combined herschel pacs and spire observations of nine bright targets at 70-500 μm. *A&A*, 555:A15, 2013. doi: 10.1051/0004-6361/201321329. URL `https://doi.org/10.1051/0004-6361/201321329`.

A. C. Fowler. A mathematical model of magma transport in the asthenosphere. *Geophysical & Astrophysical Fluid Dynamics*, 33(1-4):63–96, 1985. doi: 10.1080/03091928508245423. URL `http://dx.doi.org/10.1080/03091928508245423`.

B. N. Frandsen, P. O. Wennberg, and H. G. Kjaergaard. Identification of osso as a near-uv absorber in the venusian atmosphere. *Geophysical Research Letters*, 43(21): 11,146–11,155, Nov. 2016. doi: 10.1002/2016GL070916. URL `https://agupubs.onlinelibrary.wiley.com/doi/abs/10.1002/2016GL070916`.

W. C. Fraser, M. T. Bannister, R. E. Pike, M. Marsset, M. E. Schwamb, J. J. Kavelaars, P. Lacerda, D. Nesvorný, K. Volk, A. Delsanti, S. Benecchi, M. J. Lehner, K. Noll, B. Gladman, J.-M. Petit, S. Gwyn, Y.-T. Chen, S.-Y. Wang, M. Alexandersen, T. Burdullis, S. Sheppard, and C. Trujillo. All planetesimals born near

the kuiper belt formed as binaries. *Nature Astronomy*, 1:0088–, Apr. 2017. URL http://dx.doi.org/10.1038/s41550-017-0088.

P. Gao, X. Zhang, D. Crisp, C. G. Bardeen, and Y. L. Yung. Bimodal distribution of sulfuric acid aerosols in the upper haze of venus. *Icarus*, 231:83 – 98, 2014. ISSN 0019-1035. doi: http://dx.doi.org/10.1016/j.icarus.2013.10.013. URL http://www.sciencedirect.com/science/article/pii/S0019103513004326.

C. Goldblatt, T. D. Robinson, K. J. Zahnle, and D. Crisp. Low simulated radiation limit for runaway greenhouse climates. *Nature Geosci*, 6(8):661–667, Aug. 2013. ISSN 1752-0894. URL http://dx.doi.org/10.1038/ngeo1892.

P. Goldreich, N. Murray, P. Y. Longaretti, and D. Banfield. Neptune's story. *Science*, 245(4917):500–504, 1989. ISSN 0036-8075. doi: 10.1126/science.245.4917.500. URL http://science.sciencemag.org/content/245/4917/500.

P. Goldreich, Y. Lithwick, and R. Sari. Formation of kuiper-belt binaries by dynamical friction and three-body encounters. *Nature*, 420:643–, Dec. 2002. URL http://dx.doi.org/10.1038/nature01227.

E. K. Graham and G. R. Barsch. Elastic constants of single-crystal forsterite as a function of temperature and pressure. *Journal of Geophysical Research*, 74(25):5949–5960, 1969. ISSN 2156-2202. doi: 10.1029/JB074i025p05949. URL http://dx.doi.org/10.1029/JB074i025p05949.

R. E. Grimm and H. Y. McSween Jr. Heliocentric zoning of the asteroid belt by

aluminum-26 heating. *Science*, pages 653–655, 1993. URL http://www.jstor.org/stable/2882870?seq=1.

W. Grundy, J. Stansberry, K. Noll, D. Stephens, D. Trilling, S. Kern, J. Spencer, D. Cruikshank, and H. Levison. The orbit, mass, size, albedo, and density of (65489) ceto/phorcys: A tidally-evolved binary centaur. *Icarus*, 191(1):286 – 297, 2007. ISSN 0019-1035. doi: https://doi.org/10.1016/j.icarus.2007.04.004. URL http://www.sciencedirect.com/science/article/pii/S0019103507001546.

W. Grundy, K. Noll, M. Buie, S. Benecchi, D. Ragozzine, and H. Roe. The mutual orbit, mass, and density of transneptunian binary g!kún'hòmdímà (229762 2007 uk126). *Icarus*, 2019. ISSN 0019-1035. doi: https://doi.org/10.1016/j.icarus.2018.12.037. URL http://www.sciencedirect.com/science/article/pii/S0019103518306286.

W. M. Grundy, R. P. Binzel, B. J. Buratti, J. C. Cook, D. P. Cruikshank, C. M. Dalle Ore, A. M. Earle, K. Ennico, C. J. A. Howett, A. W. Lunsford, C. B. Olkin, A. H. Parker, S. Philippe, S. Protopapa, E. Quirico, D. C. Reuter, B. Schmitt, K. N. Singer, A. J. Verbiscer, R. A. Beyer, M. W. Buie, A. F. Cheng, D. E. Jennings, I. R. Linscott, J. W. Parker, P. M. Schenk, J. R. Spencer, J. A. Stansberry, S. A. Stern, H. B. Throop, C. C. C. Tsang, H. A. Weaver, G. E. Weigle, L. A. Young, and T. N. H. science team. Surface compositions across pluto and charon. *Science*, 351(6279), 2016. ISSN 0036-8075. doi: 10.1126/science.aad9189. URL http://science.sciencemag.org/content/351/6279/aad9189.

K. E. Haisch, Jr., E. A. Lada, and C. J. Lada. Disk frequencies and lifetimes in young clusters. *The Astrophysical Journal Letters*, 553(2):L153, 2001. URL http://stacks.iop.org/1538-4357/553/i=2/a=L153.

N. P. Hammond, A. C. Barr, and E. M. Parmentier. Recent tectonic activity on pluto driven by phase changes in the ice shell. *Geophysical Research Letters*, pages n/a–n/a, 2016. ISSN 1944-8007. doi: 10.1002/2016GL069220. URL http://dx.doi.org/10.1002/2016GL069220. 2016GL069220.

N. P. Hammond, E. M. Parmenteir, and A. C. Barr. Compaction and melt transport in ammonia-rich ice shells: Implications for the evolution of triton. *Journal of Geophysical Research: Planets*, 123(12):3105–3118, 2018. doi: 10.1029/2018JE005781. URL https://agupubs.onlinelibrary.wiley.com/doi/abs/10.1029/2018JE005781.

H. Hiesinger, S. Marchi, N. Schmedemann, P. Schenk, J. H. Pasckert, A. Neesemann, D. P. O'Brien, T. Kneissl, A. I. Ermakov, R. R. Fu, M. T. Bland, A. Nathues, T. Platz, D. A. Williams, R. Jaumann, J. C. Castillo-Rogez, O. Ruesch, B. Schmidt, R. S. Park, F. Preusker, D. L. Buczkowski, C. T. Russell, and C. A. Raymond. Cratering on ceres: Implications for its crust and evolution. *Science*, 353(6303), Sept. 2016. ISSN 0036-8075. doi: 10.1126/science.aaf4759. URL https://science.sciencemag.org/content/353/6303/aaf4759.

P. V. Hobbs. *Ice physics*. Oxford university press, 1974.

D. M. Hunten and A. J. Watson. Stability of pluto's atmosphere. *Icarus*, 51(3):665 –

667, 1982. ISSN 0019-1035. doi: http://dx.doi.org/10.1016/0019-1035(82)90155-5. URL http://www.sciencedirect.com/science/article/pii/0019103582901555.

T. Imamura and G. L. Hashimoto. Microphysics of venusian clouds in rising tropical air. *Journal of the Atmospheric Sciences*, 58(23):3597–3612, 2001. doi: 10.1175/1520-0469(2001)058⟨3597:MOVCIR⟩2.0.CO;2. URL https://doi.org/10.1175/1520-0469(2001)058<3597:MOVCIR>2.0.CO;2.

T. Imamura, H. Ando, S. Tellmann, M. Pätzold, B. Häusler, A. Yamazaki, T. M. Sato, K. Noguchi, Y. Futaana, J. Oschlisniok, S. Limaye, R. K. Choudhary, Y. Murata, H. Takeuchi, C. Hirose, T. Ichikawa, T. Toda, A. Tomiki, T. Abe, Z.-i. Yamamoto, H. Noda, T. Iwata, S.-y. Murakami, T. Satoh, T. Fukuhara, K. Ogohara, K.-i. Sugiyama, H. Kashimura, S. Ohtsuki, S. Takagi, Y. Yamamoto, N. Hirata, G. L. Hashimoto, M. Yamada, M. Suzuki, N. Ishii, T. Hayashiyama, Y. J. Lee, and M. Nakamura. Initial performance of the radio occultation experiment in the venus orbiter mission akatsuki. *Earth, Planets and Space*, 69(1):137, Oct 2017. ISSN 1880-5981. doi: 10.1186/s40623-017-0722-3. URL https://doi.org/10.1186/s40623-017-0722-3.

T. Inoue, I. Yoshimi, A. Yamada, and T. Kikegawa. Time-resolved x-ray diffraction analysis of the experimental dehydration of serpentine at high pressure. *Journal of Mineralogical and Petrological Sciences*, 104(2):105–109, 2009. doi: 10.2465/jmps.081022d.

E. A. Irene, E. Tierney, and J. Angilello. A viscous flow model to explain the appearance of high density thermal sio2 at low oxidation temperatures. *Journal of*

The Electrochemical Society, 129(11):2594–2597, 1982. doi: 10.1149/1.2123617. URL http://jes.ecsdl.org/content/129/11/2594.abstract.

J. A. Jackson and N. J. White. Normal faulting in the upper continental crust: observations from regions of active extension. *J. Struct. Geol.*, 11:15–36, 1989.

K. L. Jessup, E. Marcq, F. Mills, A. Mahieux, S. Limaye, C. Wilson, M. Allen, J.-L. Bertaux, W. Markiewicz, T. Roman, A.-C. Vandaele, V. Wilquet, and Y. Yung. Coordinated hubble space telescope and venus express observations of venus' upper cloud deck. *Icarus*, 258:309 – 336, 2015. ISSN 0019-1035. doi: http://dx.doi.org/10.1016/j.icarus.2015.05.027. URL http://www.sciencedirect.com/science/article/pii/S0019103515002377.

F. Jiang, S. Speziale, and T. S. Duffy. Single-crystal elasticity of brucite, mg (oh) 2, to 15 gpa by brillouin scattering. *American Mineralogist*, 91(11-12):1893–1900, 2006.

G. J. Jiang, W. B. Person, and K. G. Brown. Absolute infrared intensities and band shapes in pure solid co and co in some solid matrices. *The Journal of Chemical Physics*, 62(4):1201–1211, 1975. doi: http://dx.doi.org/10.1063/1.430634. URL http://scitation.aip.org/content/aip/journal/jcp/62/4/10.1063/1.430634.

A. Johansen and M. Lambrechts. Forming planets via pebble accretion. *Annual Review of Earth and Planetary Sciences*, 45(1):359–387, 2017. doi:

10.1146/annurev-earth-063016-020226. URL https://doi.org/10.1146/annurev-earth-063016-020226.

A. Johansen, M.-M. M. Low, P. Lacerda, and M. Bizzarro. Growth of asteroids, planetary embryos, and kuiper belt objects by chondrule accretion. *Science Advances*, 1 (3), 2015. doi: 10.1126/sciadv.1500109. URL http://advances.sciencemag.org/content/1/3/e1500109.

B. C. Johnson, K. J. Walsh, D. A. Minton, A. N. Krot, and H. F. Levison. Timing of the formation and migration of giant planets as constrained by cb chondrites. *Science Advances*, 2(12), 2016. doi: 10.1126/sciadv.1601658. URL http://advances.sciencemag.org/content/2/12/e1601658.

L. Jorda, R. Gaskell, C. Capanna, S. Hviid, P. Lamy, J. Ďeurech, G. Faury, O. Groussin, P. Gutiérrez, C. Jackman, S. Keihm, H. Keller, J. Knollenberg, E. Kührt, S. Marchi, S. Mottola, E. Palmer, F. Schloerb, H. Sierks, J.-B. Vincent, M. A'Hearn, C. Barbieri, R. Rodrigo, D. Koschny, H. Rickman, M. Barucci, J. Bertaux, I. Bertini, G. Cremonese, V. D. Deppo, B. Davidsson, S. Debei, M. D. Cecco, S. Fornasier, M. Fulle, C. Güttler, W.-H. Ip, J. Kramm, M. Küppers, L. Lara, M. Lazzarin, J. L. Moreno, F. Marzari, G. Naletto, N. Oklay, N. Thomas, C. Tubiana, and K.-P. Wenzel. The global shape, density and rotation of comet 67p/churyumov-gerasimenko from preperihelion rosetta/osiris observations. *Icarus*, 277(Supplement C):257 – 278, 2016. ISSN 0019-1035. doi: https://doi.org/10.1016/j.icarus.2016.05.002. URL http://www.sciencedirect.com/science/article/pii/S0019103516301385.

S. Kamata, F. Nimmo, Y. Sekine, K. Kuramoto, N. Noguchi, J. Kimura, and A. Tani. Pluto's ocean is capped and insulated by gas hydrates. *Nature Geoscience*, 12:407–410, May 2019. doi: 10.1038/s41561-019-0369-8.

J. Keane and I. Matsuyama. Pluto followed its heart: True polar wander of pluto due to the formation and evolution of sputnik planum. In *Lunar and Planetary Science Conference*, volume 47, page 2348, 2016.

S. J. Kenyon. Planet formation in the outer solar system. *Publications of the Astronomical Society of the Pacific*, 114(793):265, 2002. URL `http://stacks.iop.org/1538-3873/114/i=793/a=265`.

S. J. Kenyon and B. C. Bromley. Coagulation Calculations of Icy Planet Formation at 15-150 AU: A Correlation between the Maximum Radius and the Slope of the Size Distribution for Trans-Neptunian Objects. *Astron. J.*, 143(3):63, Mar 2012. doi: 10.1088/0004-6256/143/3/63.

S. J. Kenyon and J. X. Luu. Accretion in the early kuiper belt. ii. fragmentation. *The Astronomical Journal*, 118(2):1101, 1999. URL `http://stacks.iop.org/1538-3881/118/i=2/a=1101`.

S. J. Kenyon, B. C. Bromley, D. P. O'Brien, and D. R. Davis. Formation and collisional evolution of kuiper belt objects. *The Solar System Beyond Neptune*, 293, 2008.

H. Kieffer. Thermal model for analysis of mars infrared mapping. *Journal of Geo-*

physical Research: Planets, 118(3):451–470, 2013. ISSN 2169-9100. doi: 10.1029/2012JE004164. URL http://dx.doi.org/10.1029/2012JE004164.

J. Kimura and S. Kamata. Stability of the subsurface ocean of pluto. *Planetary and Space Science*, 181:104828, 2020. ISSN 0032-0633. doi: https://doi.org/10.1016/j.pss.2019.104828. URL http://www.sciencedirect.com/science/article/pii/S0032063318303854.

C. Kiss, G. Marton, A. Farkas-Takács, J. Stansberry, T. Müller, J. Vinkó, Z. Balog, J.-L. Ortiz, and A. Pál. Discovery of a satellite of the large trans-neptunian object (225088) 2007 or 10. *The Astrophysical Journal Letters*, 838(1):L1, 2017. URL http://stacks.iop.org/2041-8205/838/i=1/a=L1.

R. G. Knollenberg and D. M. Hunten. The microphysics of the clouds of venus: Results of the pioneer venus particle size spectrometer experiment. *Journal of Geophysical Research: Space Physics*, 85(A13):8039–8058, 1980. ISSN 2156-2202. doi: 10.1029/JA085iA13p08039. URL http://dx.doi.org/10.1029/JA085iA13p08039.

V. Krasnopolsky and J. Pollack. H2o-h2so4 system in venus' clouds and ocs, co, and h2so4 profiles in venus' troposphere. *Icarus*, 109(1):58 – 78, 1994. ISSN 0019-1035. doi: http://dx.doi.org/10.1006/icar.1994.1077. URL http://www.sciencedirect.com/science/article/pii/S0019103584710773.

V. A. Krasnopolsky. A sensitive search for nitric oxide in the lower atmospheres of venus and mars: Detection on venus and upper limit for mars. *Icarus*, 182(1):80 –

91, 2006. ISSN 0019-1035. doi: http://dx.doi.org/10.1016/j.icarus.2005.12.003. URL //www.sciencedirect.com/science/article/pii/S0019103505004975.

V. A. Krasnopolsky. Chemical kinetic model for the lower atmosphere of venus. *Icarus*, 191(1):25 – 37, 2007. ISSN 0019-1035. doi: http://dx.doi.org/10.1016/j.icarus.2007.04.028. URL http://www.sciencedirect.com/science/article/pii/S0019103507002059.

V. A. Krasnopolsky. Spatially-resolved high-resolution spectroscopy of venus 1. variations of co2, co, hf, and {HCl} at the cloud tops. *Icarus*, 208(2):539 – 547, 2010a. ISSN 0019-1035. doi: http://dx.doi.org/10.1016/j.icarus.2010.02.012. URL //www.sciencedirect.com/science/article/pii/S0019103510000862.

V. A. Krasnopolsky. Spatially-resolved high-resolution spectroscopy of venus 2. variations of hdo, ocs, and {SO2} at the cloud tops. *Icarus*, 209(2):314 – 322, 2010b. ISSN 0019-1035. doi: http://dx.doi.org/10.1016/j.icarus.2010.05.008. URL //www.sciencedirect.com/science/article/pii/S0019103510001892.

V. A. Krasnopolsky. A photochemical model for the venus atmosphere at 47-112 km. *Icarus*, 218(1):230 – 246, 2012. ISSN 0019-1035. doi: http://dx.doi.org/10.1016/j.icarus.2011.11.012. URL http://www.sciencedirect.com/science/article/pii/S0019103511004398.

V. A. Krasnopolsky. S3 and s4 abundances and improved chemical kinetic model for the lower atmosphere of venus. *Icarus*, 225(1):570 – 580, 2013. ISSN 0019-1035. doi:

https://doi.org/10.1016/j.icarus.2013.04.026. URL http://www.sciencedirect.com/science/article/pii/S0019103513001917.

V. A. Krasnopolsky. Vertical profiles of h2o, h2so4, and sulfuric acid concentration at 45-75 km on venus. *Icarus*, 252(0):327 – 333, 2015. ISSN 0019-1035. doi: http://dx.doi.org/10.1016/j.icarus.2015.01.024. URL http://www.sciencedirect.com/science/article/pii/S0019103515000408.

V. A. Krasnopolsky. Disulfur dioxide and its near-uv absorption in the photochemical model of venus atmosphere. *Icarus*, 299:294 – 299, 2018. ISSN 0019-1035. doi: https://doi.org/10.1016/j.icarus.2017.08.013. URL http://www.sciencedirect.com/science/article/pii/S0019103517300490.

T. S. Kruijer, C. Burkhardt, G. Budde, and T. Kleine. Age of jupiter inferred from the distinct genetics and formation times of meteorites. *Proceedings of the National Academy of Sciences*, 114(26):6712–6716, 2017. ISSN 0027-8424. doi: 10.1073/pnas.1704461114. URL http://www.pnas.org/content/114/26/6712.

W. Lane and R. Opstbaum. High altitude venus haze from pioneer venus limb scans. *Icarus*, 54(1):48 – 58, 1983. ISSN 0019-1035. doi: https://doi.org/10.1016/0019-1035(83)90071-4. URL http://www.sciencedirect.com/science/article/pii/0019103583900714.

Z. M. Leinhardt, R. A. Marcus, and S. T. Stewart. The formation of the collisional

family around the dwarf planet haumea. *The Astrophysical Journal*, 714(2):1789, 2010. URL http://stacks.iop.org/0004-637X/714/i=2/a=1789.

J. Leliwa-Kopystyński and K. Kossacki. Evolution of porosity in small icy bodies. *Planetary and Space Science*, 48(7):727 – 745, 2000. ISSN 0032-0633. doi: https://doi.org/10.1016/S0032-0633(00)00038-6. URL http://www.sciencedirect.com/science/article/pii/S0032063300000386.

J. Leliwa-Kopystyński, M. Maruyama, and T. Nakajima. The water-ammonia phase diagram up to 300 mpa: Application to icy satellites. *Icarus*, 159(2):518 – 528, 2002. ISSN 0019-1035. doi: http://dx.doi.org/10.1006/icar.2002.6932. URL http://www.sciencedirect.com/science/article/pii/S0019103502969320.

E. Lellouch, B. Sicardy, C. de Bergh, H.-U. Käufl, S. Kassi, and A. Campargue. Pluto's lower atmosphere structure and methane abundance from high-resolution spectroscopy and stellar occultations. *A&A*, 495(3):L17–L21, 2009. doi: 10.1051/0004-6361/200911633. URL http://dx.doi.org/10.1051/0004-6361/200911633.

S. S. Limaye, D. Grassi, A. Mahieux, A. Migliorini, S. Tellmann, and D. Titov. Venus atmospheric thermal structure and radiative balance. *Space Science Reviews*, 214(5):102, Aug. 2018. ISSN 1572-9672. URL https://doi.org/10.1007/s11214-018-0525-2.

J. J. Lissauer and G. R. Stewart. Growth of planets from planetesimals. In E. H. Levy and J. I. Lunine, editors, *Protostars and Planets III*, pages 1061–1088, 1993.

C.-W. Lu, Y.-J. Wu, Y.-P. Lee, R. S. Zhu, and M. C. Lin. Experimental and theoretical investigation of rate coefficients of the reaction s(p3)+ocs in the temperature range of 298-985k. *The Journal of Chemical Physics*, 125(16):164329, 2006. doi: 10.1063/1.2357739. URL `https://doi.org/10.1063/1.2357739`.

A. Mahieux, V. Wilquet, A. Vandaele, S. Robert, R. Drummond, S. Chamberlain, A. G. Ribes, and J. Bertaux. Hydrogen halides measurements in the venus mesosphere retrieved from soir on board venus express. *Planetary and Space Science*, 113-114:264 – 274, 2015. ISSN 0032-0633. doi: https://doi.org/10.1016/j.pss.2014.12.014. URL `http://www.sciencedirect.com/science/article/pii/S0032063314004061`. SI:Exploration of Venus.

U. Malamud and D. Prialnik. Modeling kuiper belt objects charon, orcus and salacia by means of a new equation of state for porous icy bodies. *Icarus*, 246:21–36, 2015.

U. Malamud and D. Prialnik. A 1-d evolutionary model for icy satellites, applied to enceladus. *Icarus*, 268:1 – 11, 2016. ISSN 0019-1035. doi: http://dx.doi.org/10.1016/j.icarus.2015.12.046. URL `http://www.sciencedirect.com/science/article/pii/S0019103515006120`.

U. Malamud, H. B. Perets, and G. Schubert. The contraction/expansion history of charon with implication for its planetary scale tectonic belt. *ArXiv e-prints*, Mar. 2016.

R. L. Marcialis, G. H. Rieke, and L. A. Lebofsky. The surface composition of charon? tentative identification of water ice. *Science*, 237:1349–51, 1987.

E. Marcq, T. Encrenaz, B. Bézard, and M. Birlan. Remote sensing of venus' lower atmosphere from ground-based {IR} spectroscopy: Latitudinal and vertical distribution of minor species. *Planetary and Space Science*, 54(13?14):1360 – 1370, 2006. ISSN 0032-0633. doi: http://dx.doi.org/10.1016/j.pss.2006.04.024. URL `//www.sciencedirect.com/science/article/pii/S0032063306001632`. The Planet Venus and the Venus Express MissionThe Planet Venus and the Venus Express Mission.

E. Marcq, B. Bézard, P. Drossart, G. Piccioni, J. M. Reess, and F. Henry. A latitudinal survey of co, ocs, h2o, and so2 in the lower atmosphere of venus: Spectroscopic studies using virtis-h. *Journal of Geophysical Research: Planets*, 113(E5), 2008. ISSN 2156-2202. doi: 10.1029/2008JE003074. URL `http://dx.doi.org/10.1029/2008JE003074`. E00B07.

E. Marcq, F. P. Mills, C. D. Parkinson, and A. C. Vandaele. Composition and chemistry of the neutral atmosphere of venus. *Space Science Reviews*, 214(1):10, Nov 2017. ISSN 1572-9672. doi: 10.1007/s11214-017-0438-5. URL `https://doi.org/10.1007/s11214-017-0438-5`.

E. Marcq, L. Baggio, F. Lefèvre, A. Stolzenbach, F. Montmessin, D. Belyaev, O. Korablev, and J.-L. Bertaux. Discovery of cloud top ozone on venus. *Icarus*, 319:491 –

498, 2019. ISSN 0019-1035. doi: https://doi.org/10.1016/j.icarus.2018.10.006. URL http://www.sciencedirect.com/science/article/pii/S001910351830352X.

E. Marcq, K. L. Jessup, L. Baggio, T. Encrenaz, Y. J. Lee, F. Montmessin, D. Belyaev, O. Korablev, and J.-L. Bertaux. Climatology of so2 and uv absorber at venus' cloud top from spicav-uv nadir dataset. *Icarus*, 335:113368, 2020. ISSN 0019-1035. doi: https://doi.org/10.1016/j.icarus.2019.07.002. URL http://www.sciencedirect.com/science/article/pii/S0019103519302283.

I. Matsuyama, D. Johnstone, and L. Hartmann. Viscous diffusion and photoevaporation of stellar disks. *The Astrophysical Journal*, 582(2):893, 2003. URL http://stacks.iop.org/0004-637X/582/i=2/a=893.

K. McGouldrick and O. B. Toon. An investigation of possible causes of the holes in the condensational venus cloud using a microphysical cloud model with a radiative-dynamical feedback. *Icarus*, 191(1):1 – 24, 2007. ISSN 0019-1035. doi: https://doi.org/10.1016/j.icarus.2007.04.007. URL http://www.sciencedirect.com/science/article/pii/S0019103507001649.

P. McGovern, O. White, and P. Schenk. Tectonism across pluto: Mapping and interpretations. In *Pluto System After New Horizons*, volume 2133, 2019.

W. B. McKinnon and S. Mueller. Pluto's structure and composition suggest origin in the solar, not a planetary, nebula. *Nature*, 335:240–, Sept. 1988. URL http://dx.doi.org/10.1038/335240a0.

W. B. McKinnon, S. Stern, H. Weaver, F. Nimmo, C. Bierson, J. Cook, W. Grundy, D. Cruikshank, A. Parker, J. Moore, J. Spencer, L. Young, C. Olkin, and K. E. Smith. Origin of the pluto-charon system: Constraints from the new horizons flyby. *Icarus*, pages –, 2017. ISSN 0019-1035. doi: http://dx.doi.org/10.1016/j.icarus.2016.11.019. URL http://www.sciencedirect.com/science/article/pii/S0019103516307473.

W. B. McKinnon, P. M. Schenk, M. T. Bland, K. N. Singer, O. L. White, J. M. Moore, J. R. Spencer, L. A. Young, C. B. Olkin, H. A. Weaver, S. A. Stern, and New Horizons GGI Theme Team. Pluto's Heat Flow: A Mystery Wrapped in an Ocean Inside an Ice Shell. In *Lunar and Planetary Science Conference*, volume 49 of *Lunar and Planetary Inst. Technical Report*, page 2715, Mar. 2018.

R. Merk and D. Prialnik. Combined modeling of thermal evolution and accretion of trans-neptunian objects-occurrence of high temperatures and liquid water. *Icarus*, 183(2):283 – 295, 2006. ISSN 0019-1035. doi: https://doi.org/10.1016/j.icarus.2006.02.011. URL http://www.sciencedirect.com/science/article/pii/S0019103506000741.

C. Milbury, B. C. Johnson, H. J. Melosh, G. S. Collins, D. M. Blair, J. M. Soderblom, F. Nimmo, C. J. Bierson, R. J. Phillips, and M. T. Zuber. Pre-impact porosity controls the gravity signature of lunar craters. *Geophysical Research Letters*, 42(17), 2015. ISSN 1944-8007. doi: 10.1002/2015GL066198. URL http://dx.doi.org/10.1002/2015GL066198.

F. P. Mills. *I. Observations and photochemical modeling of the Venus middle atmosphere. II. Thermal infrared spectroscopy of Europa and Callisto.* PhD thesis, California Institute of Technology, 1998.

F. P. Mills and M. Allen. A review of selected issues concerning the chemistry in venus' middle atmosphere. *Planetary and Space Science*, 55(12):1729–1740, 2007.

J. Monteux, G. Tobie, G. Choblet, and M. Le Feuvre. Can large icy moons accrete undifferentiated? *Icarus*, 237:377–387, Jul 2014. doi: 10.1016/j.icarus.2014.04.041.

F. Montmessin, J.-L. Bertaux, F. Lefèvre, E. Marcq, D. Belyaev, J.-C. Gérard, O. Korablev, A. Fedorova, V. Sarago, and A. Vandaele. A layer of ozone detected in the nightside upper atmosphere of venus. *Icarus*, 216(1):82 – 85, 2011. ISSN 0019-1035. doi: http://dx.doi.org/10.1016/j.icarus.2011.08.010. URL `//www.sciencedirect.com/science/article/pii/S0019103511003277`.

J. M. Moore, W. B. McKinnon, J. R. Spencer, A. D. Howard, P. M. Schenk, R. A. Beyer, F. Nimmo, K. N. Singer, O. M. Umurhan, O. L. White, S. A. Stern, K. Ennico, C. B. Olkin, H. A. Weaver, L. A. Young, R. P. Binzel, M. W. Buie, B. J. Buratti, A. F. Cheng, D. P. Cruikshank, W. M. Grundy, I. R. Linscott, H. J. Reitsema, D. C. Reuter, M. R. Showalter, V. J. Bray, C. L. Chavez, C. J. A. Howett, T. R. Lauer, C. M. Lisse, A. H. Parker, S. B. Porter, S. J. Robbins, K. Runyon, T. Stryk, H. B. Throop, C. C. C. Tsang, A. J. Verbiscer, A. M. Zangari, A. L. Chaikin, D. E. Wilhelms, and N. H. S. Team. The geology of pluto and charon through the eyes of new horizons. *Science*,

351(6279):1284–1293, 2016. ISSN 0036-8075. doi: 10.1126/science.aad7055. URL http://science.sciencemag.org/content/351/6279/1284.

A. Morbidelli and D. Nesvorny. *Kuiper belt: formation and evolution*, page 25?53. 2020.

J. I. Moses, M. Y. Zolotov, and B. Fegley. Photochemistry of a volcanically driven atmosphere on io: Sulfur and oxygen species from a pele-type eruption. *Icarus*, 156(1): 76 – 106, 2002. ISSN 0019-1035. doi: https://doi.org/10.1006/icar.2001.6758. URL http://www.sciencedirect.com/science/article/pii/S0019103501967582.

M. J. Mumma and S. B. Charnley. The chemical composition of comets-emerging taxonomies and natal heritage. *Annual Review of Astronomy and Astrophysics*, 49 (1):471–524, 2011. doi: 10.1146/annurev-astro-081309-130811. URL http://dx.doi.org/10.1146/annurev-astro-081309-130811.

D. Nesvorný, A. N. Youdin, and D. C. Richardson. Formation of kuiper belt binaries by gravitational collapse. *The Astronomical Journal*, 140(3):785, 2010. URL http://stacks.iop.org/1538-3881/140/i=3/a=785.

D. Nesvorný, R. Li, A. N. Youdin, J. B. Simon, and W. M. Grundy. Trans-neptunian binaries as evidence for planetesimal formation by the streaming instability. *Nature Astronomy*, 3(9):808–812, Sept. 2019. ISSN 2397-3366. URL https://doi.org/10.1038/s41550-019-0806-z.

M. Neveu, S. J. Desch, and J. C. Castillo-Rogez. Aqueous geochemistry in icy world interiors: Equilibrium fluid, rock, and gas compositions, and fate of antifreezes and

radionuclides. *Geochim. Cosmochim. Acta*, 212:324–371, Sept. 2017. doi: 10.1016/j.gca.2017.06.023.

F. Nimmo and J. Spencer. Powering triton recent geological activity by obliquity tides: Implications for pluto geology. *Icarus*, pages 1–9, Feb. 2014. ISSN 00191035. doi: 10.1016/j.icarus.2014.01.044. URL http://linkinghub.elsevier.com/retrieve/pii/S001910351400075X.

F. Nimmo, R. Pappalardo, and B. Giese. On the origins of band topography, europa. *Icarus*, 166(1):21 – 32, 2003. ISSN 0019-1035. doi: http://dx.doi.org/10.1016/j.icarus.2003.08.002. URL http://www.sciencedirect.com/science/article/pii/S0019103503002367.

F. Nimmo, D. P. Hamilton, W. B. McKinnon, P. M. Schenk, R. P. Binzel, C. J. Bierson, R. A. Beyer, J. M. Moore, S. A. Stern, H. A. Weaver, C. B. Olkin, L. A. Young, K. E. Smith, and New Horizons Geology, Geophysics & Imaging Theme Team. Reorientation of sputnik planitia implies a subsurface ocean on pluto. *Nature*, advance online publication:–, Nov. 2016a. ISSN 1476-4687. URL http://dx.doi.org/10.1038/nature20148.

F. Nimmo, O. Umurhan, C. M. Lisse, C. J. Bierson, T. R. Lauer, M. W. Buie, H. B. Throop, J. A. Kammer, J. H. Roberts, W. B. McKinnon, A. M. Zangari, J. M. Moore, S. A. Stern, L. A. Young, H. A. Weaver, C. B. Olkin, and K. Ennico. Mean radius and shape of pluto and charon from new horizons images. *Icarus*, pages –,

2016b. ISSN 0019-1035. doi: http://dx.doi.org/10.1016/j.icarus.2016.06.027. URL http://www.sciencedirect.com/science/article/pii/S0019103516303529.

F. Nimmo, O. M. Umurhan, C. M. Lisse, C. J. Bierson, T. R. Lauer, M. W. Buie, H. B. Throop, J. A. Kammer, J. H. Roberts, W. B. McKinnon, J. M. Moore, S. Stern, L. A. Young, H. A. Weaver, C. B. Olkin, K. Ennico, and the New Horizons GGI team. Mean radius and shape of pluto and charon from new horizons images. *ArXiv e-prints*, Mar. 2016.

C. W. Ormel. *The Emerging Paradigm of Pebble Accretion*, volume 445 of *Astrophysics and Space Science Library*, page 197. 2017. doi: 10.1007/978-3-319-60609-5_7.

J. L. Ortiz, P. Santos-Sanz, B. Sicardy, G. Benedetti-Rossi, D. Bérard, N. Morales, R. Duffard, F. Braga-Ribas, U. Hopp, C. Ries, V. Nascimbeni, F. Marzari, V. Granata, A. Pál, C. Kiss, T. Pribulla, R. Komžík, K. Hornoch, P. Pravec, P. Bacci, M. Maestripieri, L. Nerli, L. Mazzei, M. Bachini, F. Martinelli, G. Succi, F. Ciabattari, H. Mikuz, A. Carbognani, B. Gaehrken, S. Mottola, S. Hellmich, F. L. Rommel, E. Fernádez-Valenzuela, A. C. Bagatin, S. Cikota, A. Cikota, J. Lecacheux, R. Vieira-Martins, J. I. B. Camargo, M. Assafin, F. Colas, R. Behrend, J. Desmars, E. Meza, A. Alvarez-Candal, W. Beisker, A. R. Gomes-Junior, B. E. Morgado, F. Roques, F. Vachier, J. Berthier, T. G. Mueller, J. M. Madiedo, O. Unsalan, E. Sonbas, N. Karaman, O. Erece, D. T. Koseoglu, T. Ozisik, S. Kalkan, Y. Guney, M. S. Niaei, O. Satir, C. Yesilyaprak, C. Puskullu, A. Kabas, O. Demircan, J. Alikakos, V. Charmandaris, G. Leto, J. Ohlert, J. M. Christille, R. Szakáts,

A. T. Farkas, E. Varga-Verebélyi, G. Marton, A. Marciniak, P. Bartczak, T. Santana-Ros, M. Butkiewicz-Bkak, G. Dudziński, V. Alí-Lagoa, K. Gazeas, L. Tzouganatos, N. Paschalis, V. Tsamis, A. Sánchez-Lavega, S. Pérez-Hoyos, R. Hueso, J. C. Guirado, V. Peris, and R. Iglesias-Marzoa. The size, shape, density and ring of the dwarf planet haumea from a stellar occultation. *Nature*, 550:219–, Oct. 2017. URL http://dx.doi.org/10.1038/nature24051.

J. Oschlisniok, B. Häusler, M. Pätzold, G. Tyler, M. Bird, S. Tellmann, S. Remus, and T. Andert. Microwave absorptivity by sulfuric acid in the venus atmosphere: First results from the venus express radio science experiment vera. *Icarus*, 221(2):940 – 948, 2012. ISSN 0019-1035. doi: https://doi.org/10.1016/j.icarus.2012.09.029. URL http://www.sciencedirect.com/science/article/pii/S0019103512004022.

A. H. Parker, M. W. Buie, W. M. Grundy, and K. S. Noll. Discovery of a makemakean moon. *The Astrophysical Journal Letters*, 825(1):L9, 2016. URL http://stacks.iop.org/2041-8205/825/i=1/a=L9.

C. D. Parkinson, P. Gao, L. Esposito, Y. Yung, S. Bougher, and M. Hirtzig. Photochemical control of the distribution of venusian water. *Planetary and Space Science*, 113? 114:226 – 236, 2015. ISSN 0032-0633. doi: http://dx.doi.org/10.1016/j.pss.2015.02.015. URL http://www.sciencedirect.com/science/article/pii/S0032063315000501. SI:Exploration of Venus.

J.-M. Petit and O. Mousis. Kbo binaries: how numerous were they? *Icarus*, 168(2):409

– 419, 2004. ISSN 0019-1035. doi: https://doi.org/10.1016/j.icarus.2003.12.013. URL http://www.sciencedirect.com/science/article/pii/S0019103503004330.

V. F. Petrenko and R. W. Whitworth. Elastic, thermal, and lattice dynamical properties. In *Physics of Ice*, pages –. Oxford University Press, Oxford, 2002. URL http://www.oxfordscholarship.com/view/10.1093/acprof:oso/9780198518945.001.0001/acprof-9780198518945-chapter-3.

S. Protopapa, H. Boehnhardt, T. M. Herbst, D. P. Cruikshank, W. M. Grundy, F. Merlin, and C. B. Olkin. Surface characterization of pluto and charon by l and m band spectra. *A&A*, 490(1):365–375, 2008. doi: 10.1051/0004-6361:200809994. URL http://dx.doi.org/10.1051/0004-6361:200809994.

F. L. Pundsack. The properties of asbestos. ii. the density and structure of chrysotile. *The Journal of Physical Chemistry*, 60(3):361–364, 1956. doi: 10.1021/j150537a027. URL http://dx.doi.org/10.1021/j150537a027.

A. Rivoldini, T. V. Hoolst, and O. Verhoeven. The interior structure of mercury and its core sulfur content. *Icarus*, 201(1):12 – 30, 2009. ISSN 0019-1035. doi: https://doi.org/10.1016/j.icarus.2008.12.020. URL http://www.sciencedirect.com/science/article/pii/S001910350800448X.

G. Robuchon and F. Nimmo. Thermal evolution of pluto and implications for surface tectonics and a subsurface ocean. *Icarus*, 216(2):426 – 439, 2011. ISSN 0019-1035. doi:

http://dx.doi.org/10.1016/j.icarus.2011.08.015. URL http://www.sciencedirect.com/science/article/pii/S0019103511003320.

M. E. Rubin, S. J. Desch, and M. Neveu. The effect of rayleigh-taylor instabilities on the thickness of undifferentiated crust on kuiper belt objects. *Icarus*, 236 (Supplement C):122 – 135, 2014. ISSN 0019-1035. doi: https://doi.org/10.1016/j.icarus.2014.03.047. URL http://www.sciencedirect.com/science/article/pii/S0019103514001821.

B. J. Sandor and R. T. Clancy. Observations of hcl altitude dependence and temporal variation in the 70-100km mesosphere of venus. *Icarus*, 220(2):618 – 626, 2012. ISSN 0019-1035. doi: https://doi.org/10.1016/j.icarus.2012.05.016. URL http://www.sciencedirect.com/science/article/pii/S0019103512001984.

B. J. Sandor and R. T. Clancy. Diurnal observations of hcl altitude variation in the 70-100 km mesosphere of venus. *Icarus*, 290:156 – 161, 2017. ISSN 0019-1035. doi: http://dx.doi.org/10.1016/j.icarus.2017.02.017. URL http://www.sciencedirect.com/science/article/pii/S0019103516307242.

B. J. Sandor and R. T. Clancy. First measurements of clo in the venus atmosphere - altitude dependence and temporal variation. *Icarus*, 313:15 – 24, 2018. ISSN 0019-1035. doi: https://doi.org/10.1016/j.icarus.2018.04.022. URL http://www.sciencedirect.com/science/article/pii/S001910351830040X.

B. J. Sandor, R. T. Clancy, and G. Moriarty-Schieven. Upper limits for h2so4 in the

mesosphere of venus. *Icarus*, 217(2):839 – 844, 2012. ISSN 0019-1035. doi: http://dx.doi.org/10.1016/j.icarus.2011.03.032. URL http://www.sciencedirect.com/science/article/pii/S0019103511001291. Advances in Venus Science.

M. Satorre, M. Domingo, C. Millán, R. Luna, R. Vilaplana, and C. Santonja. Density of ch4, n2 and co2 ices at different temperatures of deposition. *Planetary and Space Science*, 56(13):1748 – 1752, 2008. ISSN 0032-0633. doi: http://dx.doi.org/10.1016/j.pss.2008.07.015. URL http://www.sciencedirect.com/science/article/pii/S0032063308002304. Advances in Planetary Sciences: AOGS 20074th Annual Meeting of the.

M. Satorre, J. Leliwa-Kopystynski, C. Santonja, and R. Luna. Refractive index and density of ammonia ice at different temperatures of deposition. *Icarus*, 225(1):703 – 708, 2013. ISSN 0019-1035. doi: https://doi.org/10.1016/j.icarus.2013.04.023. URL http://www.sciencedirect.com/science/article/pii/S0019103513001887.

M. Sawai, I. Katayama, A. Hamada, M. Maeda, and S. Nakashima. Dehydration kinetics of antigorite using in situ high-temperature infrared microspectroscopy. *Physics and Chemistry of Minerals*, 40(4):319–330, 2013. ISSN 1432-2021. doi: 10.1007/s00269-013-0573-9. URL http://dx.doi.org/10.1007/s00269-013-0573-9.

P. Saxena, J. P. Renaud, W. G. Henning, M. Jutzi, and T. Hurford. Relevance of tidal heating on large tnos. *Icarus*, 302:245 – 260, 2018. ISSN 0019-1035. doi: https://doi.org/10.1016/j.icarus.2017.11.023. URL http://www.sciencedirect.com/science/article/pii/S0019103517303858.

E. L. Schaller and M. E. Brown. Volatile loss and retention on kuiper belt objects. *The Astrophysical Journal Letters*, 659(1):L61, 2007. URL http://stacks.iop.org/1538-4357/659/i=1/a=L61.

P. M. Schenk, R. A. Beyer, W. B. McKinnon, J. M. Moore, J. R. Spencer, O. L. White, K. Singer, F. Nimmo, C. Thomason, T. R. Lauer, S. Robbins, O. M. Umurhan, W. M. Grundy, S. A. Stern, H. A. Weaver, L. A. Young, K. E. Smith, and C. Olkin. Basins, fractures and volcanoes: Global cartography and topography of pluto from new horizons. *Icarus*, 314:400 – 433, 2018. ISSN 0019-1035. doi: https://doi.org/10.1016/j.icarus.2018.06.008. URL http://www.sciencedirect.com/science/article/pii/S0019103517306024.

H. E. Schlichting and R. Sari. Runaway growth during planet formation: Explaining the size distribution of large kuiper belt objects. *The Astrophysical Journal*, 728(1):68, 2011. URL http://stacks.iop.org/0004-637X/728/i=1/a=68.

A. Seiff, J. Schofield, A. Kliore, F. Taylor, S. Limaye, H. Revercomb, L. Sromovsky, V. Kerzhanovich, V. Moroz, and M. Marov. Models of the structure of the atmosphere of venus from the surface to 100 kilometers altitude. *Advances in Space Research*, 5(11):3 – 58, 1985. ISSN 0273-1177. doi: https://doi.org/10.1016/0273-1177(85)90197-8. URL http://www.sciencedirect.com/science/article/pii/0273117785901978.

W. D. Shao, X. Zhang, C. J. Bierson, and T. Encrenaz. Revisiting the sulfur-water chemical system in the middle atmosphere of venus. *JGR:Planets*, In Review.

Y. Shoshany, D. Prialnik, and M. Podolak. Monte carlo modeling of the thermal conductivity of porous cometary ice. *Icarus*, 157(1):219 – 227, 2002. ISSN 0019-1035. doi: http://dx.doi.org/10.1006/icar.2002.6815. URL `http://www.sciencedirect.com/science/article/pii/S0019103502968156`.

B. Sicardy, J. L. Ortiz, M. Assafin, E. Jehin, A. Maury, E. Lellouch, R. G. Hutton, F. Braga-Ribas, F. Colas, D. Hestroffer, J. Lecacheux, F. Roques, P. Santos-Sanz, T. Widemann, N. Morales, R. Duffard, A. Thirouin, A. J. Castro-Tirado, M. Jelnek, P. Kubánek, A. Sota, R. Sánchez-Ramrez, A. H. Andrei, J. I. B. Camargo, D. N. da Silva Neto, A. R. Gomes, R. V. Martins, M. Gillon, J. Manfroid, G. P. Tozzi, C. Harlingten, S. Saravia, R. Behrend, S. Mottola, E. G. Melendo, V. Peris, J. Fabregat, J. M. Madiedo, L. Cuesta, M. T. Eibe, A. Ullán, F. Organero, S. Pastor, J. A. de los Reyes, S. Pedraz, A. Castro, I. de la Cueva, G. Muler, I. A. Steele, M. Cebrián, P. Montas-Rodríguez, A. Oscoz, D. Weaver, C. Jacques, W. J. B. Corradi, F. P. Santos, W. Reis, A. Milone, M. Emilio, L. Gutiérrez, R. Vázquez, and H. Hernández-Toledo. A pluto-like radius and a high albedo for the dwarf planet eris from an occultation. *Nature*, 478(7370):493–496, Oct. 2011. ISSN 1476-4687. URL `https://doi.org/10.1038/nature10550`.

K. N. Singer, W. B. McKinnon, B. Gladman, S. Greenstreet, E. B. Bierhaus, S. A. Stern, A. H. Parker, S. J. Robbins, P. M. Schenk, W. M. Grundy, V. J. Bray, R. A. Beyer, R. P. Binzel, H. A. Weaver, L. A. Young, J. R. Spencer, J. J. Kavelaars, J. M. Moore, A. M. Zangari, C. B. Olkin, T. R. Lauer, C. M. Lisse, K. Ennico,

New Horizons Geology, Geophysics and Imaging Science Theme Team, New Horizons Surface Composition Science Theme Team, and New Horizons Ralph and LORRI Teams. Impact craters on pluto and charon indicate a deficit of small kuiper belt objects. *Science*, 363(6430):955–959, 2019. ISSN 0036-8075. doi: 10.1126/science.aap8628. URL https://science.sciencemag.org/content/363/6430/955.

S. W. Squyres, R. T. Reynolds, A. L. Summers, and F. Shung. Accretional heating of the satellites of saturn and uranus. *Journal of Geophysical Research: Solid Earth*, 93(B8):8779–8794, 1988. URL http://onlinelibrary.wiley.com/doi/10.1029/JB093iB08p08779/full.

J. Stansberry, W. Grundy, M. Mueller, S. Benecchi, G. Rieke, K. Noll, M. Buie, H. Levison, S. Porter, and H. Roe. Physical properties of trans-neptunian binaries (120347) salacia-actaea and (42355) typhon-echidna. *Icarus*, 219(2):676 – 688, 2012. ISSN 0019-1035. doi: https://doi.org/10.1016/j.icarus.2012.03.029. URL http://www.sciencedirect.com/science/article/pii/S0019103512001224.

J. A. Stansberry, W. M. Grundy, J. L. Margot, D. P. Cruikshank, J. P. Emery, G. H. Rieke, and D. E. Trilling. The albedo, size, and density of binary kuiper belt object (47171) 1999 tc36. *The Astrophysical Journal*, 643(1):556, 2006. URL http://stacks.iop.org/0004-637X/643/i=1/a=556.

S. A. Stern, F. Bagenal, K. Ennico, G. R. Gladstone, W. M. Grundy, W. B. McKinnon, J. M. Moore, C. B. Olkin, J. R. Spencer, H. A. Weaver, L. A. Young, T. Andert, J. Andrews, M. Banks, B. Bauer, J. Bauman, O. S. Barnouin, P. Bedini, K. Beisser,

R. A. Beyer, S. Bhaskaran, R. P. Binzel, E. Birath, M. Bird, D. J. Bogan, A. Bowman, V. J. Bray, M. Brozovic, C. Bryan, M. R. Buckley, M. W. Buie, B. J. Buratti, S. S. Bushman, A. Calloway, B. Carcich, A. F. Cheng, S. Conard, C. A. Conrad, J. C. Cook, D. P. Cruikshank, O. S. Custodio, C. M. Dalle Ore, C. Deboy, Z. J. B. Dischner, P. Dumont, A. M. Earle, H. A. Elliott, J. Ercol, C. M. Ernst, T. Finley, S. H. Flanigan, G. Fountain, M. J. Freeze, T. Greathouse, J. L. Green, Y. Guo, M. Hahn, D. P. Hamilton, S. A. Hamilton, J. Hanley, A. Harch, H. M. Hart, C. B. Hersman, A. Hill, M. E. Hill, D. P. Hinson, M. E. Holdridge, M. Horanyi, A. D. Howard, C. J. A. Howett, C. Jackman, R. A. Jacobson, D. E. Jennings, J. A. Kammer, H. K. Kang, D. E. Kaufmann, P. Kollmann, S. M. Krimigis, D. Kusnierkiewicz, T. R. Lauer, J. E. Lee, K. L. Lindstrom, I. R. Linscott, C. M. Lisse, A. W. Lunsford, V. A. Mallder, N. Martin, D. J. McComas, R. L. McNutt, D. Mehoke, T. Mehoke, E. D. Melin, M. Mutchler, D. Nelson, F. Nimmo, J. I. Nunez, A. Ocampo, W. M. Owen, M. Paetzold, B. Page, A. H. Parker, J. W. Parker, F. Pelletier, J. Peterson, N. Pinkine, M. Piquette, S. B. Porter, S. Protopapa, J. Redfern, H. J. Reitsema, D. C. Reuter, J. H. Roberts, S. J. Robbins, G. Rogers, D. Rose, K. Runyon, K. D. Retherford, M. G. Ryschkewitsch, P. Schenk, E. Schindhelm, B. Sepan, M. R. Showalter, K. N. Singer, M. Soluri, D. Stanbridge, A. J. Steffl, D. F. Strobel, T. Stryk, M. E. Summers, J. R. Szalay, M. Tapley, A. Taylor, H. Taylor, H. B. Throop, C. C. C. Tsang, G. L. Tyler, O. M. Umurhan, A. J. Verbiscer, M. H. Versteeg, M. Vincent, R. Webbert, S. Weidner, G. E. Weigle, O. L. White, K. Whittenburg, B. G. Williams, K. Williams, S. Williams, W. W. Woods, A. M. Zangari, and E. Zirnstein. The pluto system:

Initial results from its exploration by new horizons. *Science*, 350(6258), 2015. doi: 10.1126/science.aad1815. URL http://www.sciencemag.org/content/350/6258/aad1815.abstract.

S. A. Stern, W. M. Grundy, W. B. McKinnon, H. A. Weaver, and L. Young. The Pluto system after New Horizons. *Ann. Rev. Astron. Astrophys.*, 56:357–392, 2018.

D. J. Stevenson. *Mantle convection: plate tectonics and global dynamics*, chapter Formation and early evolution of the Earth, pages 817–873. Gordon and Breach Science, 1989.

H. Tang and N. Dauphas. Abundance, distribution, and origin of 60fe in the solar protoplanetary disk. *Earth and Planetary Science Letters*, 359-360:248 – 263, 2012. ISSN 0012-821X. doi: https://doi.org/10.1016/j.epsl.2012.10.011. URL http://www.sciencedirect.com/science/article/pii/S0012821X12005705.

S. C. Tegler, W. Romanishin, and S. J. G. J. Consolmagno. Two color populations of kuiper belt and centaur objects and the smaller orbital inclinations of red centaur objects. *The Astronomical Journal*, 152(6):210, 2016. URL http://stacks.iop.org/1538-3881/152/i=6/a=210.

D. J. Tholen and M. W. Buie. Bulk properties of pluto and charon. *Pluto and Charon*, 1:193, 1997.

P. Thomas. The shape of triton from limb profiles. *Icarus*, 148(2):587 – 588, 2000.

ISSN 0019-1035. doi: https://doi.org/10.1006/icar.2000.6511. URL http://www.sciencedirect.com/science/article/pii/S0019103500965114.

P. C. Thomas, J. W. Armstrong, S. W. Asmar, J. A. Burns, T. Denk, B. Giese, P. Helfenstein, L. Iess, T. V. Johnson, A. McEwen, L. Nicolaisen, C. Porco, N. Rappaport, J. Richardson, L. Somenzi, P. Tortora, E. P. Turtle, and J. Veverka. Hyperion/'s sponge-like appearance. *Nature*, 448(7149):50–56, July 2007. ISSN 0028-0836. URL http://dx.doi.org/10.1038/nature05779.

F. Tian and O. B. Toon. Hydrodynamic escape of nitrogen from pluto. *Geophysical Research Letters*, 32(18):n/a–n/a, 2005. ISSN 1944-8007. doi: 10.1029/2005GL023510. URL http://dx.doi.org/10.1029/2005GL023510. L18201.

F. Tian, O. B. Toon, A. A. Pavlov, and H. D. Sterck. Transonic hydrodynamic escape of hydrogen from extrasolar planetary atmospheres. *The Astrophysical Journal*, 621 (2):1049, 2005. URL http://stacks.iop.org/0004-637X/621/i=2/a=1049.

L. Trafton. Does pluto have a substantial atmosphere? *Icarus*, 44(1):53 – 61, 1980. ISSN 0019-1035. doi: http://dx.doi.org/10.1016/0019-1035(80)90054-8. URL http://www.sciencedirect.com/science/article/pii/0019103580900548.

D. L. Turcotte and G. Schubert. *Geodynamics*. Cambridge University Press, 2014.

O. Umurhan, A. Howard, J. Moore, A. Earle, O. White, P. Schenk, R. Binzel, S. Stern, R. Beyer, F. Nimmo, W. McKinnon, K. Ennico, C. Olkin, H. Weaver, and L. Young. Modeling glacial flow on and onto pluto's sputnik planitia. *Icarus*, 287:301 – 319, 2017.

ISSN 0019-1035. doi: https://doi.org/10.1016/j.icarus.2017.01.017. URL http://www.sciencedirect.com/science/article/pii/S0019103517300489. Special Issue: The Pluto System.

S. D. Vance, K. P. Hand, and R. T. Pappalardo. Geophysical controls of chemical disequilibria in europa. *Geophysical Research Letters*, 43(10):4871–4879, 2016. ISSN 1944-8007. doi: 10.1002/2016GL068547. URL http://dx.doi.org/10.1002/2016GL068547. 2016GL068547.

A. Vandaele, O. Korablev, D. Belyaev, S. Chamberlain, D. Evdokimova, T. Encrenaz, L. Esposito, K. Jessup, F. Lefévre, S. Limaye, A. Mahieux, E. Marcq, F. Mills, F. Montmessin, C. Parkinson, S. Robert, T. Roman, B. Sandor, A. Stolzenbach, C. Wilson, and V. Wilquet. Sulfur dioxide in the venus atmosphere: I. vertical distribution and variability. *Icarus*, 295:16 – 33, 2017. ISSN 0019-1035. doi: https://doi.org/10.1016/j.icarus.2017.05.003. URL http://www.sciencedirect.com/science/article/pii/S0019103516303281.

Vilenius, E., Kiss, C., Müller, T., Mommert, M., Santos-Sanz, P., Pál, A., Stansberry, J., Mueller, M., Peixinho, N., Lellouch, E., Fornasier, S., Delsanti, A., Thirouin, A., Ortiz, J. L., Duffard, R., Perna, D., and Henry, F. "tnos are cool": A survey of the trans-neptunian region - x. analysis of classical kuiper belt objects from herschel and spitzer observations. *A&A*, 564:A35, 2014. doi: 10.1051/0004-6361/201322416. URL https://doi.org/10.1051/0004-6361/201322416.

U. von Zahn, D. Krankowsky, K. Mauersberger, A. O. Nier, and D. M. Hunten. Venus

thermosphere: In situ composition measurements, the temperature profile, and the homopause altitude. *Science*, 203(4382):768–770, 1979. ISSN 00368075, 10959203. URL http://www.jstor.org/stable/1747089.

H. Wang, B. P. Weiss, X.-N. Bai, B. G. Downey, J. Wang, J. Wang, C. Suavet, R. R. Fu, and M. E. Zucolotto. Lifetime of the solar nebula constrained by meteorite paleomagnetism. *Science*, 355(6325):623–627, 2017. ISSN 0036-8075. doi: 10.1126/science.aaf5043. URL http://science.sciencemag.org/content/355/6325/623.

R. C. Weber, P.-Y. Lin, E. J. Garnero, Q. Williams, and P. Lognonné. Seismic detection of the lunar core. *Science*, 331(6015):309–312, 2011. ISSN 0036-8075. doi: 10.1126/science.1199375. URL http://science.sciencemag.org/content/331/6015/309.

W. W. Wegner and W. Ernst. Experimentally determined hydration and dehydration reaction rates in the system mgo-sio2-h2o. *American Journal of Science*, 283:151–180, 1983. URL http://earth.geology.yale.edu/~ajs/1983/11.1983.06Wegner.pdf.

O. L. White, J. M. Moore, W. B. McKinnon, J. R. Spencer, A. D. Howard, P. M. Schenk, R. A. Beyer, F. Nimmo, K. N. Singer, O. M. Umurhan, S. A. Stern, K. Ennico, C. B. Olkin, H. A. Weaver, L. A. Young, A. F. Cheng, T. Bertrand, R. P. Binzel, A. M. Earle, W. M. Grundy, T. R. Lauer, S. Protopapa, S. J. Robbins, and B. Schmitt. Geological mapping of sputnik planitia on pluto. *Icarus*, 287:261 – 286, 2017. ISSN 0019-1035. doi: https://doi.org/10.1016/j.icarus.2017.01.011. URL http://www.sciencedirect.com/science/article/pii/S001910351630598X. Special Issue: The Pluto System.

M. a. Wieczorek, G. a. Neumann, F. Nimmo, W. S. Kiefer, G. J. Taylor, H. J. Melosh, R. J. Phillips, S. C. Solomon, J. C. Andrews-Hanna, S. W. Asmar, A. S. Konopliv, F. G. Lemoine, D. E. Smith, M. M. Watkins, J. G. Williams, and M. T. Zuber. The crust of the moon as seen by GRAIL. *Science (New York, N.Y.)*, 339(6120):671–5, Feb. 2013. ISSN 1095-9203. doi: 10.1126/science.1231530. URL `http://www.ncbi.nlm.nih.gov/pubmed/23223394`.

J. P. Williams and L. A. Cieza. Protoplanetary disks and their evolution. *Annual Review of Astronomy and Astrophysics*, 49(1):67–117, 2011. doi: 10.1146/annurev-astro-081710-102548. URL `https://doi.org/10.1146/annurev-astro-081710-102548`.

R. Woo and A. Ishimaru. Eddy diffusion coefficient for the atmosphere of venus from radio scintillation measurements. *Nature*, 289(5796):383–384, Jan. 1981. ISSN 1476-4687. URL `https://doi.org/10.1038/289383a0`.

R. Woo, J. Armstrong, and A. Kliore. Small-scale turbulence in the atmosphere of venus. *Icarus*, 52(2):335 – 345, 1982. ISSN 0019-1035. doi: https://doi.org/10.1016/0019-1035(82)90116-6. URL `http://www.sciencedirect.com/science/article/pii/0019103582901166`.

M. Yasui and M. Arakawa. Compaction experiments on ice-silica particle mixtures: Implication for residual porosity of small icy bodies. *Journal of Geophysical Research: Planets*, 114(E9), 2009. ISSN 2156-2202. doi: 10.1029/2009JE003374. URL `http://dx.doi.org/10.1029/2009JE003374`. E09004.

A. N. Youdin and J. Goodman. Streaming instabilities in protoplanetary disks. *The Astrophysical Journal*, 620(1):459, 2005. URL http://stacks.iop.org/0004-637X/620/i=1/a=459.

Y. L. Yung and W. Demore. Photochemistry of the stratosphere of venus: Implications for atmospheric evolution. *Icarus*, 51(2):199 – 247, 1982. ISSN 0019-1035. doi: http://dx.doi.org/10.1016/0019-1035(82)90080-X. URL http://www.sciencedirect.com/science/article/pii/001910358290080X.

Y. L. Yung, M. C. Liang, X. Jiang, R. L. Shia, C. Lee, B. Bézard, and E. Marcq. Evidence for carbonyl sulfide (ocs) conversion to co in the lower atmosphere of venus. *Journal of Geophysical Research: Planets*, 114(E5), 2009. ISSN 2156-2202. doi: 10.1029/2008JE003094. URL http://dx.doi.org/10.1029/2008JE003094. E00B34.

X. Zhang and A. P. Showman. Global-mean vertical tracer mixing in planetary atmospheres. II. tidally locked planets. *The Astrophysical Journal*, 866(1):2, oct 2018a. doi: 10.3847/1538-4357/aada7c. URL https://doi.org/10.3847%2F1538-4357%2Faada7c.

X. Zhang and A. P. Showman. Global-mean vertical tracer mixing in planetary atmospheres. i. theory and fast-rotating planets. *The Astrophysical Journal*, 866(1):1, oct 2018b. doi: 10.3847/1538-4357/aada85. URL https://doi.org/10.3847%2F1538-4357%2Faada85.

X. Zhang, M.-C. Liang, F. Montmessin, J.-L. Bertaux, C. Parkinson, and Y. L. Yung.

Photolysis of sulphuric acid as the source of sulphur oxides in the mesosphere of venus. *Nature geoscience*, 3(12):834–837, 2010.

X. Zhang, M. C. Liang, F. P. Mills, D. A. Belyaev, and Y. L. Yung. Sulfur chemistry in the middle atmosphere of venus. *Icarus*, 217(2):714–739, 2012. ISSN 0019-1035. doi: 10.1016/j.icarus.2011.06.016. URL http://www.sciencedirect.com/science/article/pii/S0019103511002338. Advances in Venus Science.

M. Y. Zolotov. Gas-Solid Interactions on Venus and Other Solar System Bodies. *Reviews in Mineralogy and Geochemistry*, 84(1):351–392, 11 2018. ISSN 1529-6466. doi: 10.2138/rmg.2018.84.10. URL https://doi.org/10.2138/rmg.2018.84.10.

Appendix A

Mass conservation derivations

As a layer changes in density it will change in volume to conserve mass. Using conservation of mass we can solve for the change in radius of the layer that is changing mass. In the following R_t and R_b denote the upper and lower bound of a layer.

$$M_0 = M_f \tag{A.1}$$

$$\rho_0(R_{t,0}^3 - R_{b,0}^3) = \rho_f(R_{t,f}^3 - R_{b,f}^3) \tag{A.2}$$

$$\Psi = \frac{\rho_0}{\rho_f} = \frac{R_{t,f}^3 - R_{b,f}^3}{R_{t,0}^3 - R_{b,0}^3} \tag{A.3}$$

$$\Psi R_{t,0}^3 - \Psi R_{b,0}^3 = R_{t,f}^3 - R_{b,f}^3 \tag{A.4}$$

Let $R_{b,0} = R_{b,f}$ (fixed bottom boundary)

$$R_{t,f}^3 - \Psi R_{t,0}^3 = R_{b,0}^3(1 - \Psi) \tag{A.5}$$

$$\Delta R_t = R_{t,f} - R_{t,0} \tag{A.6}$$

$$(\Delta R_t + R_{t,0})^3 - \Psi R_{t,0}^3 = R_{b,0}^3(1 - \Psi) \tag{A.7}$$

$$\left(1 + \frac{\Delta R_t}{R_{t,0}}\right)^3 - \Psi = \left(\frac{R_{b,0}}{R_{t,0}}\right)^3 (1 - \Psi) \tag{A.8}$$

Let $\Delta z = R_{t,0} - R_{b,0}$

$$\left(1 + \frac{\Delta R_t}{R_{t,0}}\right)^3 = \left(1 - \frac{\Delta z}{R_{t,0}}\right)^3 (1 - \Psi) + \Psi \tag{A.9}$$

$$\Delta R_t = \left\{ \left[\left(1 - \frac{\Delta z}{R_{t,0}}\right)^3 (1 - \Psi) + \Psi \right]^{1/3} - 1 \right\} R_{t,0} \tag{A.10}$$

Because of the spherical geometry each layer will change thickness by a different amount. In the following let Δa and Δb be the change in radial position at the locations R_b and R_t respectively. Δa is known from the previous layer so for each layer we must solve for Δb.

$$\Delta a \equiv R_{b,f} - R_{b,0} \tag{A.11}$$

$$\Delta b \equiv R_{t,f} - R_{t,0} \tag{A.12}$$

$$\Delta z_0 \equiv R_{t,0} - R_{b,0} \tag{A.13}$$

$$\Delta(\Delta z) \equiv \Delta z_f - \Delta z_0 = \Delta b - \Delta a \tag{A.14}$$

$$V_0 = V_f \tag{A.15}$$

$$R_{t,0}^3 - R_{b,0}^3 = R_{t,f}^3 - R_{b,f}^3 \tag{A.16}$$

$$R_{t,f}^3 - R_{t,0}^3 = R_{b,f}^3 - R_{b,0}^3 \tag{A.17}$$

$$(\Delta b + R_{t,0})^3 - R_{t,0}^3 = R_{b,f}^3 - R_{b,0}^3 \tag{A.18}$$

$$\left(\frac{\Delta b}{R_{t,0}} + 1\right)^3 - 1 = \frac{R_{b,f}^3 - R_{b,0}^3}{R_{t,0}^3} \tag{A.19}$$

$$\left(\frac{\Delta b}{R_{t,0}} + 1\right)^3 - 1 = \left(\frac{R_{b,f}}{R_{t,0}}\right)^3 - \left(\frac{R_{b,0}}{R_{t,0}}\right)^3 \tag{A.20}$$

$$\left(\frac{\Delta b}{R_{t,0}} + 1\right)^3 - 1 = \left(\frac{\Delta a - \Delta z_0 + R_{t,0}}{R_{t,0}}\right)^3 - \left(\frac{R_{t,0} - \Delta z_0}{R_{t,0}}\right)^3 \tag{A.21}$$

$$\left(\frac{\Delta b}{R_{t,0}} + 1\right)^3 - 1 = \left(1 + \frac{\Delta a - \Delta z_0}{R_{t,0}}\right)^3 - \left(1 - \frac{\Delta z_0}{R_{t,0}}\right)^3 \tag{A.22}$$

$$\Delta b = \left\{ \left[\left(1 + \frac{\Delta a - \Delta z_0}{R_{t,0}}\right)^3 - \left(1 - \frac{\Delta z_0}{R_{t,0}}\right)^3 \right]^{1/3} - 1 \right\} R_{t,0} \tag{A.23}$$

Appendix B

Mineral densities

Table B.1: All values are for surface pressure and temperature. Water was assumed to have a density of 1000 kg/m^3.

Mineral name	Formula	Density (kg/m^3)	Source
Chrysotile	$Mg_3Si_2O_5(OH)_4$	2500	Pundsack (1956)
Forsterite	Mg_2SiO_4	3200	Graham and Barsch (1969)
Enstatite	$MgSiO_3$	3300	Ahrens and Gaffney (1971)
Silica	SiO_2	2300	Irene et al. (1982)
Brucite	$Mg(OH)_2$	2400	Jiang et al. (2006)

Appendix C

Pluto and Charon ocean thicknesses

Given our discrepancy on the dependence of the ocean thickness to core conductivity compared with Hammond et al. (2016) we want to clearly present on results here. Figure C.1 is an attempt to replicate Hammond et al. (2016) Figure S3 (0% ammonia). It is not clear why our final ocean thickness are about half that calculated by Hammond et al. (2016).

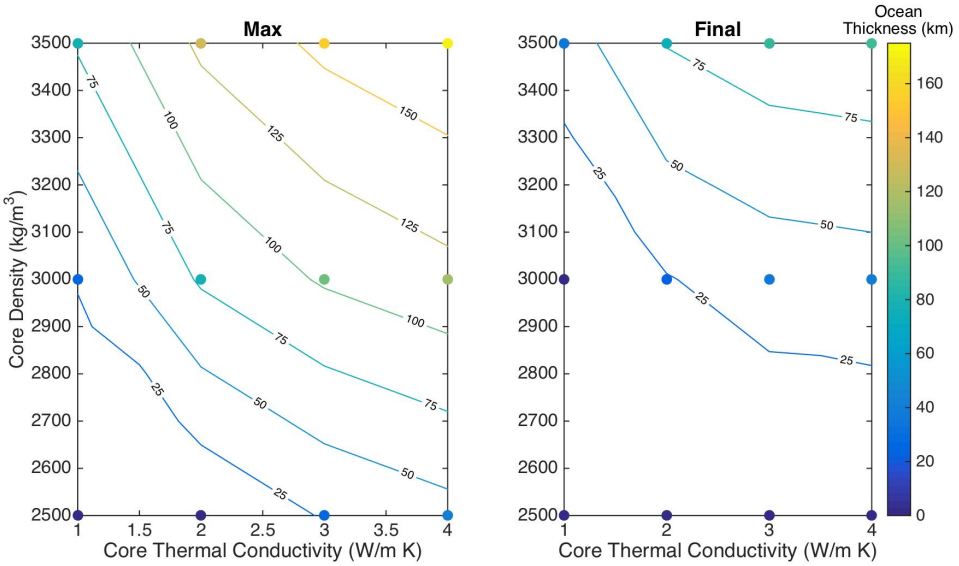

Figure C.1: Final and maximum ocean thickness for all model runs with $\phi_0 = 0.0$, $\rho_{ice} = 920$ kg/m^3, and no mass conservation. This figure is meant to be equivalent to Hammond et al. (2016) Figure S3 (0% ammonia).

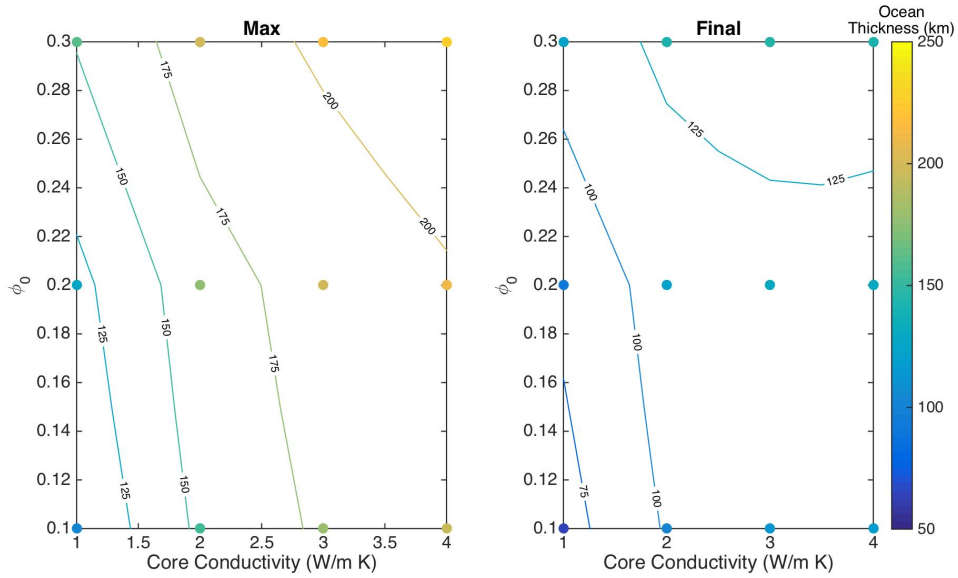

Figure C.2: Final and maximum ocean thickness for all model runs with $\rho_c = 3500$ kg/m^3, $\rho_{ice} = 950$ kg/m^3, $\eta_0 = 10^{14}$ Pa s (same as those plotted in Figure 3.2.

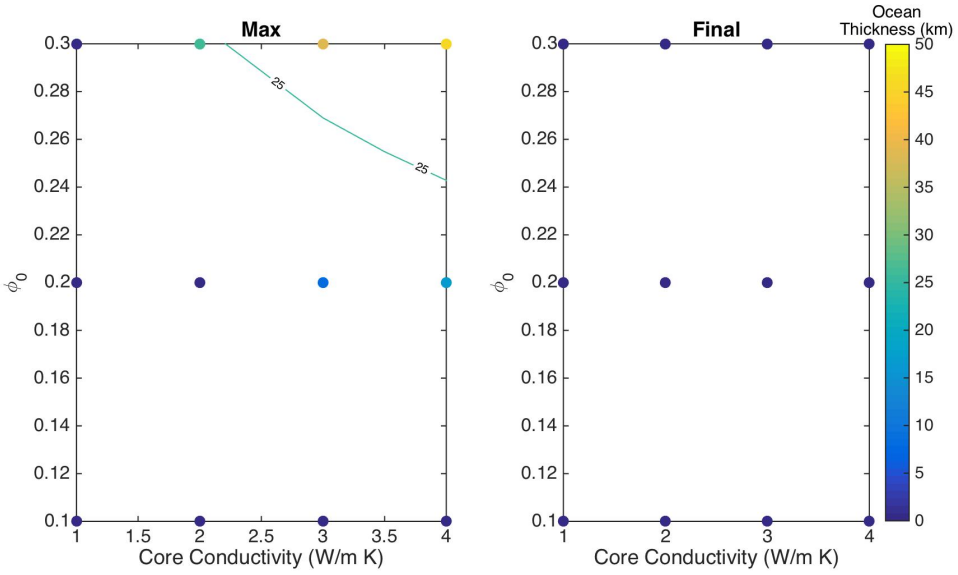

Figure C.3: Same as Figure C.2 only for Charon.

Appendix D

KBO Observations and parameters

Table D.1: Density values used.

Name			Density (kg/m^3)	Diameter (km)	Source
Typhon	42355	2002 CR_{46}	600	157 ± 34	Stansberry et al. (2012)
Ceto	65489	2003 FX_{128}	1370	174 ± 17	Grundy et al. (2007)
Teharonhiawako	88611	2001 QT_{297}	600	178^{+33}_{-36}	Vilenius, E. et al. (2014)
		2001 QC_{298}	1140	235^{+21}_{-23}	Vilenius, E. et al. (2014)
Altjira	148780	2001 UQ_{18}	300	123^{+19}_{-69}	Vilenius, E. et al. (2014)
Sila	79360	1997 CS_{29}	730	249^{+30}_{-31}	Vilenius, E. et al. (2014)
Lempo	47171	1999 TC_{36}	500	304 ± 101	Stansberry et al. (2006)
G!kún||'hòmdímà	229762	2007 UK_{126}	1040	632 ± 34	Grundy et al. (2019)
	55637	2002 UX_{25}	820	652 ± 12	Brown (2013)
Varda	174567	2003 MW_{12}	1270	705^{+81}_{-75}	Vilenius, E. et al. (2014)
Salacia	120347	2004 SB_{60}	1260	866 ± 37	Brown and Butler (2017)
Orcus	90482	2004 DW	1520	958 ± 23	Fornasier, S. et al. (2013)
Quaoar	50000	2002 LM_{60}	2180	1070 ± 38	Vilenius, E. et al. (2014)
Charon			1700	1212 ± 2	Nimmo et al. (2016b)
Haumea	136108	2003 EL_{61}	1885	1595 ± 11	Ortiz et al. (2017)
Eris	136199	2003 UB_{313}	2520	2326 ± 12	Sicardy et al. (2011)
Pluto	134340		1850	2376 ± 3	Nimmo et al. (2016b)
Triton			2060	2706 ± 1.8	Thomas (2000)

Table D.2: Radioactive isotope values used. Long lived isotope values from Robuchon and Nimmo (2011). Short lived isotope values from Castillo-Rogez et al. (2007) and Castillo-Rogez et al. (2009). Concentration is the abundance of that element relative within the silicate. For ^{60}Fe we use the value from Tang and Dauphas (2012).

Isotope	Concentration (ppb)	Specific heat production (W/kg)	Half-life (yrs)
^{235}U	5.4	568.7×10^{-6}	7.04×10^{8}
^{238}U	19.9	94.65×10^{-6}	4.47×10^{9}
^{40}K	737.9	29.17×10^{-6}	1.28×10^{9}
^{232}Th	38.7	26.38×10^{-6}	1.4×10^{10}
^{26}Al	600	0.355	7.16×10^{5}
^{60}Fe	100	7.0×10^{-2}	1.5×10^{6}
^{53} Mn	25.7	2.7×10^{-2}	3.7×10^{6}